Corrosion of Nuclear Fuel (UO_2) Inside a Failed Nuclear Waste Container

A Review of Research Conducted Under the Industrial Research Chair Agreement Between NSERC, NWMO and Western University (January 2006 to December 2010)

NWMO TR-2012-09 **May 2012**

Heming He, Michael Broczkowski, Kevin O'Neil, Derrick Ofori, Oleg Semenikhin and David Shoesmith

Western University

nwmo

NUCLEAR WASTE MANAGEMENT ORGANIZATION

SOCIÉTÉ DE GESTION DES DÉCHETS NUCLÉAIRES

Nuclear Waste Management Organization
22 St. Clair Avenue East, 6th Floor
Toronto, Ontario
M4T 2S3
Canada

Tel: 416-934-9814
Web: www.nwmo.ca

Corrosion of Nuclear Fuel (UO_2) Inside a Failed Nuclear Waste Container

A Review of Research Conducted Under the Industrial Research Chair Agreement Between NSERC, NWMO and Western University (January 2006 to December 2010)

NWMO TR-2012-09

May 2012

Heming He, Michael Broczkowski, Kevin O'Neil, Derrick Ofori, Oleg Semenikhin and David Shoesmith
Western University

Disclaimer:

This report does not necessarily reflect the views or position of the Nuclear Waste Management Organization, its directors, officers, employees and agents (the “NWMO”) and unless otherwise specifically stated, is made available to the public by the NWMO for information only. The contents of this report reflect the views of the author(s) who are solely responsible for the text and its conclusions as well as the accuracy of any data used in its creation. The NWMO does not make any warranty, express or implied, or assume any legal liability or responsibility for the accuracy, completeness, or usefulness of any information disclosed, or represent that the use of any information would not infringe privately owned rights. Any reference to a specific commercial product, process or service by trade name, trademark, manufacturer, or otherwise, does not constitute or imply its endorsement, recommendation, or preference by NWMO.

ABSTRACT

Title: **Corrosion of Nuclear Fuel (UO_2) Inside a Failed Nuclear Waste Container**
A Review of Research Conducted Under the Industrial Research Chair Agreement Between NSERC, NWMO and Western University (January 2006 to December 2010)

Report No.: **NWMO TR-2012-09**

Author(s): Heming He, Michael Broczkowski, Kevin O'Neil, Derrick Ofori, Oleg Semenikhin and David Shoesmith
Company: Western University

Date: May 2012

Abstract

This report reviews the research conducted over the second term (2006 to 2010) of an industrial research chair established to determine the behaviour of CANDU fuel wastes inside a failed waste container. Research was concentrated in three areas: (i) the influence of fuel properties on its corrosion; (ii) the possibility of local chemistries, particularly low pH, within corrosion product deposits and flaws in the fuel, and (iii) the influence of dissolved H_2, from steel corrosion, on the fuel corrosion process. A range of experimental techniques was employed including electrochemical methods, Raman spectroscopy, X-ray photoelectron spectroscopy, atomic force and current-sensing atomic force microscopy, and secondary ion mass spectrometry.

A review of spent fuel properties indicated that the key in-reactor modifications of the properties of uranium dioxide most likely to influence its corrosion are: (i) rare-earth doping of the UO_2 matrix, (ii) the production of noble metal particles, and (iii) the introduction of non-stoichiometry.

Rare-earth doping was found to have a small influence in suppressing fuel corrosion; although the mechanism by which this occurs remains to be investigated. The introduction of non-stoichiometry was found to have a major influence on fuel reactivity which increased by over a factor of 1000 over the range $x = 0.002$ to $x = 0.23$ (in UO_{2+x}). This increase was attributable to the formation of defect clusters as the degree of non-stoichiometry increased. Since the increase in non-stoichiometry due to the in-reactor production of excess oxygen is likely to be confined to $x \leq 0.007$, only a small increase in chemical reactivity (a factor of ≤ 5) of the fuel is anticipated.

Previous model calculations predicted that the development of acidic conditions in occluded regions of the fuel surface would be negligible. These predictions were verified in a series of experiments which simulated, as closely as feasibly possible, the anticipated surface conditions, and indicated acidification at the alpha radiation dose rates anticipated was extremely unlikely. These studies included experiments to assess the consequences of exposure to low pH on fuel dissolution and peroxide reduction.

Noble metal particles were shown to act as catalytic anodes for H_2 oxidation thereby suppressing fuel corrosion by the galvanic coupling of these particles to the rare earth doped conductive UO_2 matrix. Since these particles can also act as catalytic cathodes for H_2O_2 reduction and, hence, accelerate fuel corrosion via a similar galvanic-coupling process, their influence when both H_2O_2 and H_2 were present was also investigated. For 1.5 at% SIMFUEL (which approximately simulates anticipated CANDU fuel burn-ups) complete protection of the fuel surface from corrosion could be achieved providing the aqueous H_2/H_2O_2 concentration ratio was $> 10^6$.

TABLE OF CONTENTS

Page

ABSTRACT v

1. INTRODUCTION 1

2. CHARACTERISTICS OF SPENT FUEL 5

3. CHARACTERIZATION OF SIMULATED FUEL PROPERTIES 9

3.1 RAMAN SPECTROSCOPY OF URANIUM DIOXIDE 9
3.2 SIMFUEL PROPERTIES 10

4. THE INFLUENCE OF RARE EARTH – DOPING ON FUEL REACTIVITY 13

5. THE INFLUENCE OF NON-STOICHIOMETRY ON FUEL REACTIVITY 15

5.1 CRYSTALLINE STRUCTURE OF UO_2 15
5.2 MATRIX PROPERTIES OF NON-STOICHIOMETRIC UO_{2+x} 16
5.3 SURFACE PROPERTIES OF NON-STOICHIOMETRIC UO_{2+X} 21
5.4 RELATIONSHIP BETWEEN SURFACE STRUCTURE/COMPOSITION AND CORROSIVITY 25
5.5 LOCAL CORROSIVITY ON NON-STOICHIOMETRIC UO_{2+x} SURFACES 32

6. DEVELOPMENT OF LOCAL ACIDITY AT THE CORRODING FUEL SURFACE 37

6.1 THE INFLUENCE OF CORROSION PRODUCT DEPOSITS ON FUEL CORROSION 37
6.2 THE ANODIC DISSOLUTION OF UO_2 IN ACIDIC SOLUTIONS 40
6.3 THE INFLUENCE OF pH ON THE MECHANISM OF H_2O_2 REDUCTION 43

7. THE INFLUENCE OF H_2 ON FUEL CORROSION 46

7.1 THE INFLUENCE OF NOBLE METAL PARTICLES ON FUEL CORROSION 46
7.2 THE ROLE OF THE UO_2 SURFACE IN CONTROLLING SURFACE REDOX CONDITIONS 54

8. DISCUSSION AND CONCLUSIONS 56

ACKNOWLEDGEMENTS 59

REFERENCES 60

LIST OF TABLES

Page

Table 1: Resistivity of various SIMFUEL specimens 11
Table 2: Exchange current densities for proton reduction for the four predominant epsilon particle constituents 46

LIST OF FIGURES

Page

Figure 1: Cut away view of a used fuel container showing the inner steel vessel, the outer copper shell, and the fuel bundles. 1
Figure 2: Typical CANDU fuel bundle. 2
Figure 3: Alpha, beta and gamma radiation dose rates as a function of time for a layer of water in contact with a CANDU fuel bundle with a burn-up of 220 MWh/kgU (Garisto et al. 2009). 3
Figure 4: Illustration showing the key chemical and electrochemical reactions anticipated inside a failed, groundwater-flooded waste container. A radiolytic corrosion front exists on the fuel surface and an anoxic corrosion front on the surface of the steel vessel. 4
Figure 5: Scanning electron micrographs of UO_2 fuel: (a) unirradiated UO_2 and (b) irradiated fuel at high burn-up (770 MWh/kgU at 52 kW/m). In (a) two key features of the unirradiated fuel are noted. In (b) the features which cannot readily be simulated in SIMFUELs are noted in green; those which can be simulated are noted in red; the feature noted in blue is simulated in this study in separate fuel specimens. 7
Figure 6: Schematic energy-level diagram for UO_2 derived from spectroscopic and electrochemical data (expressed on the standard hydrogen scale (SHE)). The filled valence band has predominantly O2p character, and the empty conduction band consists mainly of U5f, 6d and 7f states. The U5f band contains two electrons per U atom. A more detailed description of this diagram is given by Shoesmith et al. (1994). 7
Figure 7: Schematic, A, illustrating how non-stoichiometric locations UO_{2+x} (U^{IV}/U^{V}) provide donor-acceptor sites which catalyze the cathodic reduction of oxidants, such as O_2 and H_2O_2, and promote UO_2 corrosion. As illustrated in B, non-stoichiometric locations might be expected at grain boundary locations. 8
Figure 8: A Raman spectrum recorded on sintered UO_2 with a composition close to stoichiometric. The numbers show the key features observed in the spectrum (1, 3, 4) or expected to develop as the fuel becomes more oxidized (5, 6). 9
Figure 9: Averaged Raman spectra for three SIMFUELs with different degrees of simulated burn-up (see Table 1). Averaged spectra were obtained by point-by-point (2 μm per step) mapping over a 40 μm linear region. The numbers refer to the spectral features illustrated in Figure 8 and described in the text. 11
Figure 10: ToF-SIMS images showing the distribution of noble metal (ε) particles in three SIMFUELs with different degrees of simulated burn-up. The distributions were obtained from analyses of individual elements ($^{96, 98}$Mo, $^{102, 104}$Ru and $^{106, 108}$Pd). No map for Ru is shown due to its low concentration. Each individual area is 50 μm x 50 μm. 12
Figure 11: Schematic illustrations of how noble metal (ε) particles can act either as preferential cathodes supporting oxidant reductions (A) or preferential anodes suppporting reductant oxidation reactions (B). 12

Figure 12: Voltammograms recorded on three SIMFUELs with different degrees of simulated burn-up in (A) 0.1 mol.L^{-1} NaCl at pH 9.5, and in (B), borate buffered 0.1 mol.L^{-1} NaCl at pH 9.5. The stages of oxidation described in the text are indicated by the vertical dashed lines in (A). 13
Figure 13: Current densities $i_p^{(1)}$ and $i_p^{(2)}$ recorded at the potentials indicated in Figure 12, for oxidation ($UO_2 \rightarrow UO_{2+x}$; $i_p^{(1)}$) and dissolution ($UO_{2+x} \rightarrow UO_2^{2+}$; $i_p^{(2)}$) in buffered and unbuffered solutions as a function of the degree of simulated burn-up of the three different SIMUFUELs. 14
Figure 14: The Influence of temperature on the currents recorded in voltammograms for three different SIMFUEL electrodes with different degrees of simulated burn-up in buffered 0.1 mol.L^{-1} NaCl (pH 9.5); (A) 1.5 at% (B) 3.0 at%; (C) 6.0 at%. The two stages of oxidation described in Figure 13 are labelled 1 and 2. 15
Figure 15: Schematic showing the cubic fluorite structure adopted by uranium dioxide and other actinide dioxides; ●-U atoms; o-O atoms; □-cubically coordinated empty lattice sites. The introduction of non-stoichiometry in the form of O^{II} ions accompanied by the formation of U^{V} atoms to maintain charge balance is illustrated. 16
Figure 16: SEM image of a typical surface morphology observed on a uranium dioxide specimen with a nominal stoichiometry of $UO_{2.1}$. (A) a smooth flat grain with an approximate O/U ratio of ~2.01; (B) a grain with a very shallow stepped pattern with a slightly hyperstoichiometric composition of ~2.15; (C) a grain with a pronounced stepped pattern of ridges oriented horizontally along the x – y plan with a composition of ~2.22; (D) a highly non-stoichiometric spiral-like grain with a composition of ~2.31. 17
Figure 17: Raman spectra recorded on the four types of grains (A) to (D) described in Figure 16. The O/U ratio is ~2.01, 2.15, 2.22 and 2.31 for (A), (B), (C) and (D), respectively....18
Figure 18: Sections of the Raman spectra shown in Figure 17 showing the deconvolution of the two pairs of contiguous bands at 445cm^{-1} (1) / 470cm^{-1} (2) and 575cm^{-1} (4A) / 630cm^{-1} (4B). The O/U ratio is ~2.01, 2.15, 2.22 and 2.31 for specimens (A), (B), (C) and (D), respectively. 19
Figure 19: The relationships between Raman bands 1 (445 cm^{-1}), 3 (1150 cm^{-1}) and 5 (155 cm^{-1}) based on an extensive series of Raman spot analyses. The points A to D show the peak intensities taken from the spectra shown in Figure 17, and the vertical lines indicate transitions between various defect regions. The compositional scale (based on many EDX and XRD analyses) locates the approximate degree of non-stoichiometry at which these transitions occur. 20
Figure 20: Schematic showing the principle behind the technique of current-sensing atomic force microscopy (CS-AFM). A DC bias potential is applied to the microscopy probe tip while the specimen (in the present case UO_{2+x}) is held at ground potential and the current passing through the tip and the specimen is measured. Both topographic and conductivity images are then generated simultaneously by scanning the tip across the surface allowing correlation of the surface features and the local conductivity (O'Neil at al. 2007, 2008). Also shown are two examples of the tip current-potential (I-V) bias plots recorded on a conductive and a non-conductive location. 21
Figure 21: SEM micrographs of four UO_{2+x} specimens with different nominal degrees of non-stoichiometry. Note: the scales of these four micrographs are not the same. 22
Figure 22: AFM, CS-AFM and spot analyses recorded on the $UO_{2.002}$ specimen (Figure 21). The Raman spectra were recorded at a series of locations and arranged according to the intensity of band 1 (445 cm^{-1}). The CS-AFM image is color-coded according to standard AFM practice with conducting regions shown as bright, and regions of lower activity as dark areas. 23

Figure 23: AFM, CS-AFM and Raman spot analyses recorded on the $UO_{2.011}$ specimen (Figure 21). Additional details are given in the legend to Figure 22. 23
Figure 24: AFM, CS-AFM and Raman spot analyses recorded on the $UO_{2.05}$ specimen (Figure 21). Additional details are given in the legend to Figure 22. 24
Figure 25: AFM, CS-AFM and and Raman spot analyses recorded on the $UO_{2.1}$ specimen (Figure 21). Additional details are given in the legend to Figure 22. 25
Figure 26: AFM, CS-AFM images recorded on a single grain on the $UO_{2.1}$ specimen (Figure 21): A - a non-conductive stoichiometric region; B - a uniform, moderately conductive region with randomly distributed O interstitials; C - a highly non-stoichiometric region comprising clustered defects exhibiting anisotropic conductivity. 26
Figure 27: AFM images of the surface of a $UO_{2.1}$ specimen before exposure to solution and after corrosion in a naturally aerated 0.1 mol/L NaCl solution containing a small concentration of the oxidant ferrocene methanol. 26
Figure 28: Schematic illustrating the preferential corrosion sites on a hyper stoichiometric surface exhibiting the various features observed in the SEM micrograph in Figure 16. 27
Figure 29: Voltamogram recorded on a 1.5 at% SIMFUEL in 0.1 mol/L NaCl (pH 9.5) at a scan rate of 5 mV/s. 27
Figure 30: The relative amounts of U^{IV}, U^{IV} and U^{VI} in the surface of a 1.5 at% SIMFUEL electrode determined by XPS after one hour of potentiostatic oxidation in 0.1 mol/L NaCl (pH 9.5) at each individual potential. 28
Figure 31: Voltammograms recorded on the four hyper-stoichiometric electrodes (shown in Figure 21) in 0.1 mol/L NaCl (pH 9.5) at a scan rate of 5 mV/s. The threshold is that established for the electrochemical oxidation of 1.5 at% SIMFUEL (Figure 30). 29
Figure 32: Cathodic reduction scans performed on the $UO_{2.002}$ electrode at a scan rate of 5 mV/s after individual 30 minute anodic oxidations at applied potentials in the range -0.5 V to +0.3 V in 0.1 mol/L NaCl (pH 9.5). The electrode was prepared by polishing and cathodic cleaning between each experiment. 30
Figure 33: Cathodic reduction scans performed on the $UO_{2.011}$ electrode at a scan rate of 5 mV/s after individual anodic oxidations at potentials from -0.5V to -0.1V (A) and 0.0V to+0.35V (B) in 0.1 mol/L NaCl (pH 9.5) for times ranging from 1 minute to 30 minutes at each potential: (*i*) to (*v*) indicate the locations of individual reduction peaks observed after anodic oxidation at the most positive applied potential. 31
Figure 34: Schematic illustrating the principle behind the technique of scanning electrochemical microscopy (SECM) used to supply in-situ electrochemical information at high spatial resolution (micron scale). A potential is applied to an ultra microelectrode (UME) to create an oxidant which can subsequently corrode the UO_{2+x} substrate. 33
Figure 35: An SECM image (50 µm by 50 µm) and probe approach curves recorded on a $UO_{2.011}$ electrode under corrosion conditions in 0.1 mol/L NaCl (pH 9.5). The current range is indicated in the bar on the right-side of the image. The probe approach curves are superimposed on a series of theoretical curves calculated for various values of the rate constant for the cathodic reaction on the corroding UO_{2+x} substrate surface. 34
Figure 36: An SECM map (80 µm by 80 µm) and probe approach curves recorded on a $UO_{2.05}$ electrode under corrosion conditions in 0.1 mol/L NaCl (pH 9.5). The current range is indicated on the bar attached to the image. The probe approach curves are superimposed on a series of theoretical curves calculated for various values of the rate constant for the cathodic reaction on the corroding UO_{2+x} substrate surface. 35
Figure 37: An SECM map (30 µm by 30 µm) and probe approach curves recorded on a $UO_{2.1}$ electrode under corrosion conditions in 0.1 mol/L NaCl (pH 9.5). The current range is indicated in the bar on the image. The probe approach curves are superimposed on a

series of theoretical curves calculated for various values of the rate constant for the cathodic reaction on the corroding UO_{2+x} substrate surface.....35
Figure 38: The diversity in corrosion kinetics, expressed in terms of the rate constants (determined from PACs) for the cathodic reduction reaction, and the UO_{2+x} defect structures determined by Raman mapping (expressed in terms of the intensity of band 1 (445 cm^{-1})) for the four electrodes varying in nominal composition from $UO_{2.002}$ to $UO_{2.1}$ (Figure 21). 36
Figure 39: Illustrations showing how acidity can develop within pores in a corrosion product deposit. The first panel shows that acidity can develop at the anodic dissolution site providing it is separated spatially from the cathodic site. The second panel shows that, if the two sites are not separated, then the alkalinity produced by H_2O_2 reduction will, at least partially, neutralize the acidity. 37
Figure 40: Potential-time profile recorded on a 1.5 at% SIMFUEL electrode in 0.1 mol/L NaCl (pH 9.5) in which the applied current (simulating the corrosion rate) was increased in stages from 1nA to 10nA. The area of the exposed electrode surface was ~1cm^2. 38
Figure 41: The final potentials achieved on a 1.5 at% SIMFUEL electrode at each current applied in the experiment shown in Figure 40. The dashed line at 275 mV (vs. SCE) is the approximate potential at which the development of local acidity can be clearly observed (Ofori et al. 2010).....39
Figure 42: SEM images of a 1.5 at% SIMFUEL surface after application of a sequence of applied currents (Figure 40) in 0.1 mol/L NaCl (pH 9.5) for magnifications of (A) 1500; (B) 3000; (C) 5000 X. 39
Figure 43: Raman spectrum recorded on a 1.5 at% SIMFUEL electrode after application of a sequence of applied currents from 1nA to 10nA (Figure 40). The bands are numbered as defined in Figure 8.....40
Figure 44: Anodic dissolution currents recorded on a 1.5 at% SIMUFUEL rotating disk electrode (16.7 Hz) in 0.1 mol/L^{-1} NaCl (A) and 0.1 mol.L^{-}1 Na_2SO_4 (B) solutions with various pH values: pH = 1 (black); pH = 2 (red); pH = 3 (green). The numbered lines are theoretical slopes of 40 mV/decade (1), 60 mV/decade (2), and 120 mV/decade (3)..41
Figure 45: Steady-state anodic dissolution currents recorded on a 1.5 at% SIMFUEL electrode at a potential of 325 mV, as a function of pH in 0.1 mol/L^{-1} NaCl (red) and 0.1 mol/L^{-1} Na_2SO_4 (black) 42
Figure 46: H_2O_2 reduction currents recorded on a 1.5 at% SIMFUEL electrode from negative to positive potentials at a potential scan rate of 10 mV.s^{-1} and an electrode rotation rate of 16.7 Hz in 0.1 mol/L^{-1} NaCl/0.05 mol/L^{-1} borate containing 8 x 10^{-3} mol/L^{-1} H_2O_2 with pH values of 4, 7 and 9. 44
Figure 47: H_2O_2 reduction currents recorded on a 1.5 at% SIMFUEL electrode from negative to positive potential at a scan rate of 10 mV.s^{-1} and an electrode rotation rate of 16.7 Hz in 0.1 mol.L^{-1} NaCl + 0.05 borate containing 9 x 10^{-3} mol.L^{-1} H_2O_2.....45
Figure 48: H_2O_2 reduction currents recorded on a 1.5 at% SIMFUEL electrode from negative to positive potentials at a potential scan rate of 10 mV.s^{-1} and an electrode rotation rate of 16.7 Hz. From the top to the bottom scan, (H_2O_2) = 0, 5.2, 21, 36 and 52 x 10^{-3} mol.L^{-1}. 45
Figure 49: Corrosion potential (E_{CORR}) measured on a 1.5 at% SIMFUEL electrode in 0.1 mol/L KCl (pH 9.5) purged with either O_2, Ar, or 5% H_2/95% Ar at 60ºC. The electrode was freshly polished and cathodically cleaned before each experiment. The potential threshold for surface oxidation and dissolution was established by XPS (Figure 30).....47
Figure 50: Schematic illustrations showing how noble metal (ε) particles dispersed throughout a conducting, rare each-doped UO_2 matrix could catalyst, (A) oxidant reduction reactions leading to the acceleration of corrosion, and (B) reductant oxidation

reactions leading to the suppression of corrosion. The question mark in (B) indicates that there is no substantial evidence that H_2 oxidation can reverse the corrosion reaction by driving the redeposition of dissolved UO_2^{2+}.....47
Figure 51:The influence of the increasing number and size of noble metal (ε) particles in SIMFUELs with different degrees of simulated burn-up on the corrosion potential (E_{CORR}) measured in H_2/Ar-purged 0.1 mol/L KCl (pH 9.5) at 60ºC. The dashed line indicates the potential threshold for surface oxidation and dissolution established by XPS (Broczkowski et al. 2007). The arrows indicated the approximate maximum burn-ups expected for different types of fuel.....48
Figure 52: Relative surface fractions of U^{IV}, U^{V} and U^{VI} obtained by XPS as a function of the E_{CORR} achieved in 0.1 mol/L KCl (pH 9.5) purged with either O_2, Ar, or H_2/Ar gas for SIMFUEL specimens with different degrees of simulated burn-up. For comparison, a set of data recorded on a SIMFUEL specimen not containing noble metal (ε) particles is shown. The values are superimposed on a plot showing the surface composition of a 1.5 at% SIMFUEL electrochemically oxidized at individual applied potentials (Broczkowski et al. 2007). 49
Figure 53: E_{CORR} recorded on a 1.5 at% SIMFUEL electrode in 0.1 mol/L KCl (pH 9.5) at 60ºC purged with Ar. The arrows indicate the times when H_2O_2 was added to achieve the specific concentration indicated.....50
Figure 54: E_{CORR} recorded on a 1.5 at% SIMFUEL electrode in 0.1 mol/L KCl (pH 9.5) at 60ºC purged with 5% H_2/ 95% Ar. The arrows indicate the times when H_2O_2 was added to achieve the specific concentration indicated.....51
Figure 55: The relative fractions of U^{IV}, UI^{V} and U^{VI} (as determined by XPS) in the surface of a 1.5 at% SIMFUEL electrode after additions of various [H_2O_2] to a 0.1 mol/L KCl solution (pH 9.5) purged with Ar. The lines refer to the fractions of U^{IV} (dotted line), U^{V} (dotted-dashed line) and U^{VI} (dashed line) in the surface after E_{CORR} experiments in solutions to which H_2O_2 was not added (Broczkowski 2008). 52
Figure 56: The relative fractions of U^{IV}, U^{V} and U^{VI} (as determined by XPS) in the surface of a 1.5 at% SIMFUEL electrode after additions of various [H_2O_2] to a 0.1 mol/L KCl solution (pH 9.5) purged with H_2/Ar. The lines refer to the fractions of U^{IV} (dotted line), U^{V} (dotted-dashed line) and U^{VI} (dashed line) in the surface after E_{CORR} experiments in solutions to which H_2O_2 was not added (Broczkowski 2008). 52
Figure 57: Proposed mechanism for the influence of H_2 on the corrosion 1.5 at% SIMFUEL containing noble metal (ε) particles in the presence of H_2O_2 (see text).....53
Figure 58: E_{CORR} recorded on a rare-earth doped SIMFUEL not containing noble metal particles in 0.1 mol/L KCl (pH 9.5) purged with (A) Ar at 60ºC; (B) H_2/Ar at 60ºC. The arrows indicate the times when H_2O_2 was added to achieve the specific concentration indicated.....55
Figure 59: The relative fractions of U^{IV}, U^{V} and U^{VI} (as determined by XPS) in the surface of a SIMFUEL electrode not containing noble metal (ε) particles after additions of various [H_2O_2] to a 0.1 mol/L KCl solution (pH 9.5) purged with (A) Ar; and (B) H_2/Ar. The lines refer to the fractions of U^{IV} (dotted line), U^{V} (dotted-dashed line), and U^{VI} (dashed line) in the surface after E_{CORR} experiments in solutions to which H_2O_2 was not added (Broczkowski 2008).....56

1. INTRODUCTION

The recommended approach for the long term management of used nuclear fuel in Canada is adaptive phased management. This approach includes centralized containment and the isolation of the used fuel in a deep geological repository in a suitable rock formation. The Canadian repository concept is based on multiple barriers: the used fuel bundles, durable metal containers, a clay buffer and seals around the container, and a deep geologic environment (McMurry et al. 2003). This deep geologic repository can provide reasonable assurance in the long-term containment and isolation of used fuel bundles.

A key barrier in this sequence is the container. Various container designs have been considered (King 2007; King and Shoesmith 2010; Maak and Simmons 2001; Maak 2007) and the present reference Canadian design would be fabricated with a carbon-steel vessel and an outer barrier of copper, as illustrated in Figure 1. At repository depths, groundwaters will be oxygen-free once the repository is sealed and oxygen, introduced during excavation and waste emplacement, has been consumed by mineral and biochemical reactions in the surrounding clays and by minor corrosion of the copper container. Container failure is not expected since model calculations predict corrosion should cease once the oxygen is consumed, limiting the loss of wall thickness by general corrosion to ~11μm of the available 25mm wall thickness (King and Kolar 2000).

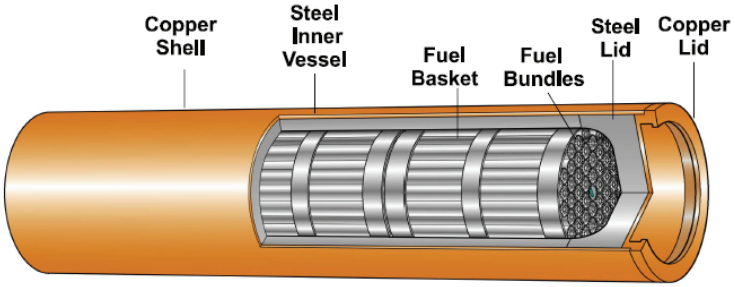


Figure 1: Cut away view of a used fuel container showing the inner steel vessel, the outer copper shell, and the fuel bundles.

It is judicious, however, to assume containers will eventually fail, thereby, exposing the used fuel bundles to groundwater. A typical fuel bundle is illustrated in Figure 2. Although the thin Zircaloy cladding on the fuel is likely to provide an additional barrier (Shoesmith and Zagidulin 2010), it is usually conservatively assumed in safety assessments that groundwater can contact the used fuel directly as soon as the container fails.

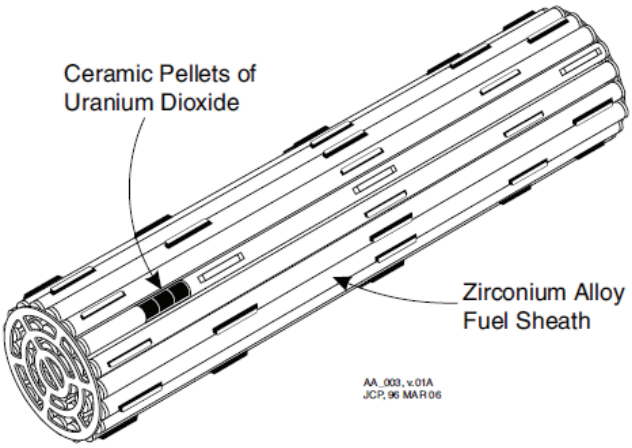


Figure 2: Typical CANDU fuel bundle.

Since the fuel contains the residual radioactivity, its behaviour on contact with the groundwater is important for the long-term safety assurance. Thus, a primary requirement for repository performance assessment models is the development of a source term model to predict the release rate of radionuclides from the fuel. Since > 95% of the radionuclides are contained within the solid state matrix of the used fuel, their release will be governed by the dissolution kinetics of the fuel. More extensive descriptions of the fuel, and the radionuclide inventory within it, have been published elsewhere (Johnson and Shoesmith 1988; Tait et al. 1989; Shoesmith 2007).

The rate of fuel dissolution will be related to, but not necessarily directly proportional to, the solubility of uranium in the groundwater contacting the fuel. The groundwater entering the container will be anoxic and the solubility of the waste form would be expected to be low ($\leq 10^{-9.5}$ mol/L) (Parks and Pohl 1988; Grenthe et al. 1992; Guillamont et al. 2003) and dissolution correspondingly slow. However, radiolysis of water due to the radiation fields associated with the fuel will establish oxidizing conditions. Under such conditions the solubility of uranium increases by many orders of magnitude (Grenthe et al. 1992), and the dissolution rate could be increased in proportion to the concentration of available radiolytic oxidants (primarily H_2O_2 from the long-lasting alpha radiolysis process). Under these conditions, fuel dissolution is a corrosion reaction whose rate will evolve as radiolytically established redox conditions change with time, Figure 3.

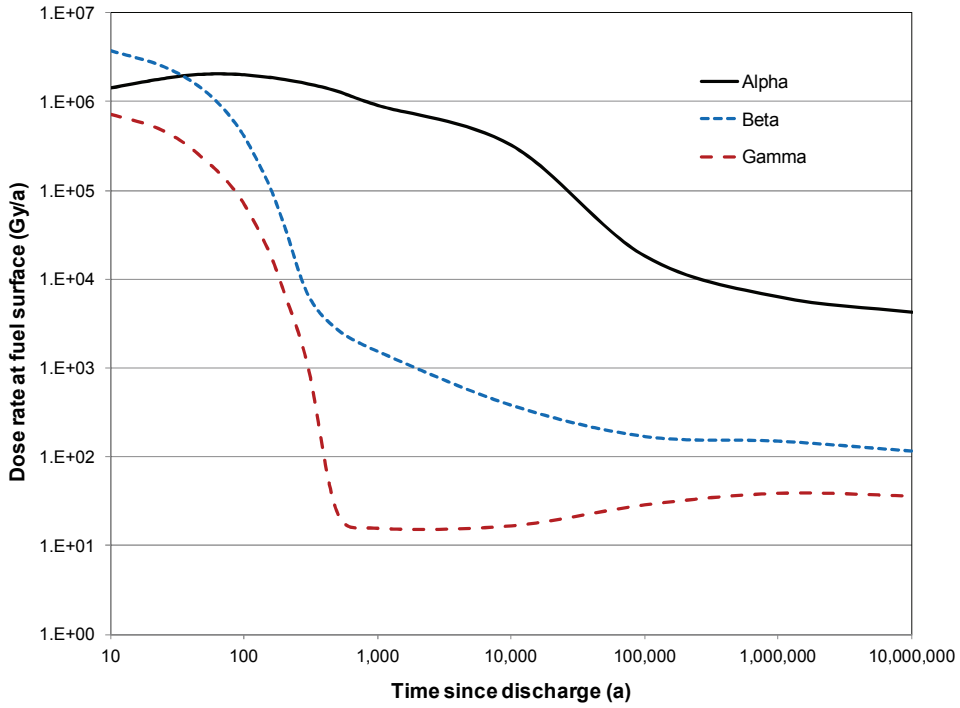


Figure 3: Alpha, beta and gamma radiation dose rates as a function of time for a layer of water in contact with a CANDU fuel bundle with a burn-up of 220 MWh/kgU (Garisto et al. 2009).

To address this issue, an Industrial Research Chair in Nuclear Fuel Disposal Chemistry (IRC) was established with the primary goal of determining both the behaviour of the fuel wasteform inside the failed container and the behaviour of the container itself. The experimental program adopted was based on numerous calculations and sensitivity analyses performed using a mixed potential electrochemical model (MPM) (Shoesmith et al. 2003) developed to describe the key processes occurring within a failed container. These processes are illustrated in Figure 4.

As indicated in the figure, and discussed in detail elsewhere, two corrosion fronts exist, one on the fuel surface driven by radiolytic oxidants and a second one on the surface of the carbon steel sustained by reaction with water to produce Fe^{2+} and H_2. In this illustration, H_2O_2 is taken to be the primary radiolytic oxidant driving fuel corrosion (Ekeroth et al. 2004, Nielsen and Jonsson 2006), although the production of O_2 via H_2O_2 decomposition could introduce a second oxidant. The following key issues were identified:

(a) The kinetics of reduction of radiolytically-produced H_2O_2, the cathodic reaction supporting fuel corrosion;
(b) The influence of corrosion product deposits on the fuel surface;
(c) The reactivity of the fuel surface;
(d) The scavenging of H_2O_2 by the products of corrosion of the carbon steel vessel;
(e) The ability of the carbon steel to maintain active corrosion conditions to produce the H_2O_2 scavengers Fe^{2+} and H_2.

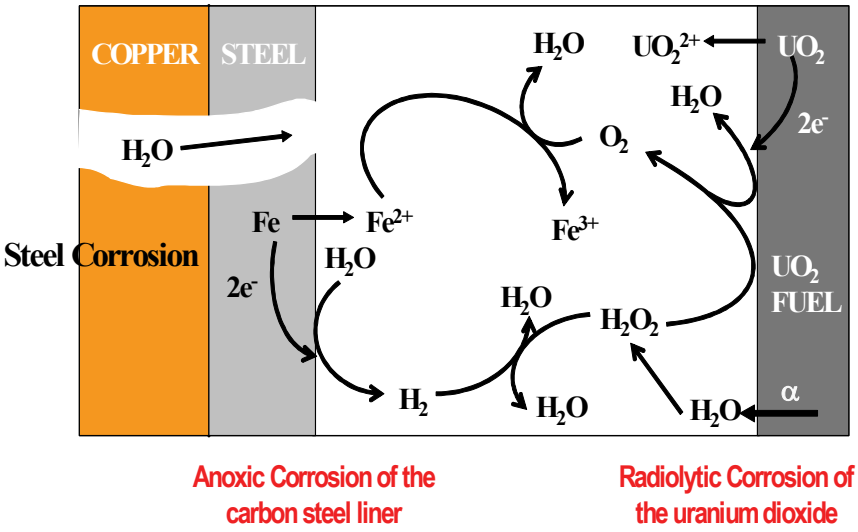


Figure 4: Illustration showing the key chemical and electrochemical reactions anticipated inside a failed, groundwater-flooded waste container. A radiolytic corrosion front exists on the fuel surface and an anoxic corrosion front on the surface of the steel vessel.

Over the first IRC term (2001 to 2005), the key achievements were the following:

(i) The composition of the fuel surface as a function of environmental redox conditions (expressed as a corrosion potential of the fuel) was determined (Santos et al. 2004). These results provided a template making it possible to specify the redox conditions under which the fuel surface is immune to, or can support, corrosion. This template has proven invaluable over the second IRC term (2006 to 2010) since it has provided a basis upon which to evaluate the influence of various redox reagents (but especially H_2O_2 and H_2) on the fuel corrosion process.

(ii) A basic knowledge of the influence of various groundwater species (carbonate/bicarbonate, silicate, and calcium) was determined (Santos et al. 2006a, b). This allowed a preliminary, but far from complete, characterization of the groundwater conditions likely to enhance (carbonate/bicarbonate by complexation of UO_2^{2+}) or retard (silicate and Ca^{2+} by formation of insoluble uranyl surface deposits) the fuel corrosion process.

(iii) A mechanism for the cathodic reduction of H_2O_2 was developed (Goldik et al. 2005, 2006). Knowledge of the mechanism of this reaction is essential since sensitivity calculations using the MPM showed the fuel corrosion rate was highly sensitive to the kinetics of this reaction (King and Kolar 2002).

(iv) Preliminary studies showed that dissolved H_2 had a very large effect on surface redox conditions (Broczkowski et al. 2005), and the potential to completely inhibit fuel corrosion.

A detailed review of the progress made over the first IRC term has been published (Shoesmith et al. 2005).

The primary goal of this report is to review the progress made over the second IRC term (2006 to 2010). The key goals defined for the second IRC term were the following:

(i) to examine the influence of fuel properties on corrosion;
(ii) to analyze the development of local chemistries within corrosion product deposits on the fuel surfaces;
(iii) to determine the kinetics of H_2 reactions with UO_2 and the possibility that synergistic reactions between H_2 and H_2O_2 could suppress fuel corrosion;
(iv) to analyze the influences of container corrosion on fuel corrosion.

The progress made in areas (i) to (iii) is reviewed in this report. Research in area (iv) was deferred to allow a greater emphasis on the key area (iii), and because the issues involved were under study in other national waste management programs.

2. CHARACTERISTICS OF SPENT FUEL

In-reactor irradiation leads to key changes in the composition and properties of the UO_2 fuel, and, from the perspective of fuel disposal, it is necessary to know the influence of in-reactor burn-up (the amount of thermal energy generated per unit mass of uranium dioxide) on fuel corrosion and dissolution rates[1]

Fuel burn-up leads to complex and significant changes in the properties of the fuel (Kleykamp 1985; Hastings 1982; Johnson and Shoesmith 1988) and the extent of burn-up changes with reactor type. While for light water reactors (LWR) burn-up is typically in the range 35 to 45 GWd/MgU, CANDU fuel burn-ups are considerably lower and generally within the range 6 to 12 (average ~8) GWd/MgU. Subtle changes in fuel density occur as fabrication sintering porosity is eliminated and the generation of fission gas bubbles expands the lattice and generates grain boundary tunnels (Johnson and Shoesmith 1988, Tait et al. 1989).

At higher linear power ratings, UO_2 grain growth becomes an important process, and thermal stresses cause cracking of the fuel matrix (Johnson and Shoesmith 1988). Collision cascades initiated by fission and alpha recoil events create a large number of atomic defects, but the final number is limited through thermal reannealing (Matzke 1982). Inhomogeneity arises at both microscopic and macroscopic levels due to temperature and neutron flux gradients and the segregation of fission products.

The chemical composition and microstructure of nuclear fuel has been studied extensively (Kleykamp 1985, 1988; Johnson and Shoesmith 1988; Grimes and Catlow 1991; Hanson 1998) and is only briefly summarized here:

(i) Elements stable in metallic form (Mo, Ru, Pd, Tc, Rh) tend to congregate in alloy precipitates, generally referred to as epsilon (ε) particles.

[1] In this report, we define fuel corrosion as the consumption of an oxidant (e.g., H_2O_2) leading to dissolution as U^{VI} (UO_2^{2+}), and fuel dissolution as the chemical release of U^{IV} not involving the consumption of an oxidant.

(ii) Fission products which are stable as oxides, but incompatible with the UO_2 matrix (Rb, Cs, Ba, Zr, Nb, Mo, Te, Sr), separate into precipitates sometimes referred to as grey phases. These phases tend to have the general composition ABO_3 and to adopt a cubic perovskite-type structure with Ba, Sr, and Cs in the A sites and Zr, Mo, U, Pu and rare earths in the B sites (Kleykamp 1985).

(iii) Elements that remain as substitutional ions within the fuel matrix include the actinides: Np, Pu, Am, and Cm; the rare earth elements (REE): La, Ce, Pr, Nd, Pm, Sm, Eu, Gd, and Y; and Sr, Zr, Ba, Te, and Nb within the limits of their solubility in the UO_2, and to the extent that they have not precipitated as perovskite-type oxides.

Two fission products are worth special mention: Mo, which can be present in both metallic and oxide forms and hence helps to maintain the fuel close to stoichiometry; and Zr which tends to distribute between perovskite-type phases and the fuel matrix, within which it exerts a major influence on lattice dimensions (Kleykamp 1993).

Despite the fact many elements created during fission are of lower oxidation state than U^{IV}, the excess oxygen created is almost completely neutralized by oxidation of Mo and reaction with the inner Zr- cladding surface (Kleykamp 1990; Floyd et al. 1992). The approximate change in CANDU fuel stoichiometry has been calculated to be from $UO_{2.000}$ to $UO_{2.007}$ (Smith et al. 1987). This slight increase in degree of non-stoichiometry, coupled to the substitution of U^{IV} by trivalent and divalent ions, leads to a substantial decrease in electrical resistivity (Hyland and Ralph 1983; Winter 1989; Dudney et al. 1981).

Based on these studies we can summarize the key changes induced in the fuel by in-reactor irradiation which we might expect to change the reactivity of the fuel under disposal conditions, Figure 5. (The SEM micrographs in this figure are taken from Hastings (1982)). Of the features shown, it is possible to simulate in unirradiated fuel analogs; (i) rare earth-doping of the UO_2 matrix; (ii) the presence of noble metal (ε) particles, and (iii) non-stoichiometry (though not necessarily located in grain boundaries). Physical changes, such as, the introduction of grain boundary tunnels and fission bubbles cannot be successfully simulated.

All of the features (i) to (iii) would be expected to influence the fuel corrosion process. Considerable evidence exists to show that the fission products and actinide – lanthanide doping of the fuel associated with burn-up exerts a significant effect on air oxidation of the fuel (Thomas et al. 1993; Choi et al. 1996; Cobos et al. 1998; McEachern and Taylor 1998) including CANDU fuel (Wasywich et al. 1993). Since fuel corrosion involves a similar conversion of U^{IV} to U^{VI} to that observed in air oxidation, one would anticipate an influence of lattice doping on fuel corrosion and radionuclide release. The dispersion of noble metal particles throughout the electrically conducting, fission product – doped UO_2 lattice introduces the strong possibility of separated, and galvanically-coupled, anodes and cathodes which would be expected to significantly influence fuel corrosion in the presence of potential oxidants (H_2O_2) and reductants (Fe^{2+}, H_2).

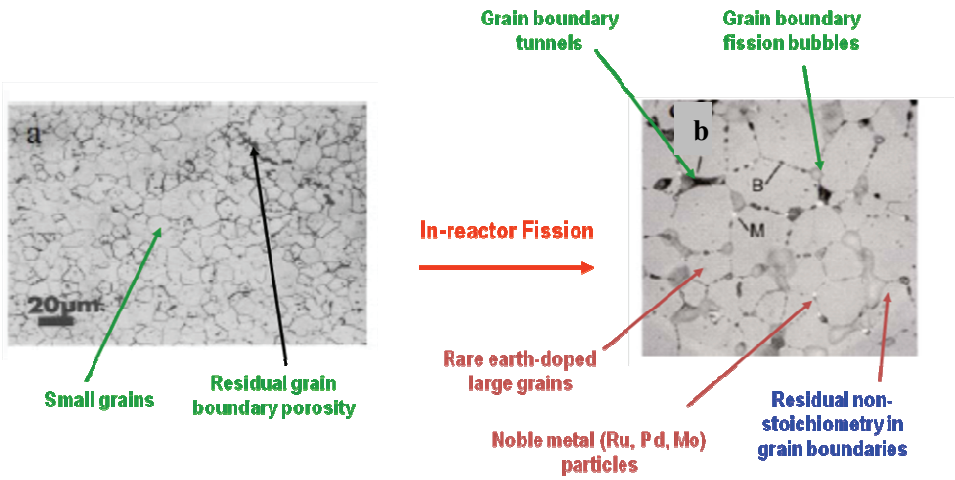


Figure 5: Scanning electron micrographs of UO_2 fuel: (a) unirradiated UO_2 and (b) irradiated fuel at high burn-up (770 MWh/kgU at 52 kW/m). In (a) two key features of the unirradiated fuel are noted. In (b) the features which cannot readily be simulated in SIMFUELs are noted in green; those which can be simulated are noted in red; the feature noted in blue is simulated in this study in separate fuel specimens.

Hyperstoichiometry (UO_{2+x}) would also exert a considerable influence on the electronic conductivity of UO_2. In the stoichiometric form, UO_2 is a Mott-Hubbard insulator with a filled narrow 5f band containing two electrons per U atom, located in the ~5eV gap between the filled valence band and the empty conduction band, Figure 6 (Shoesmith et al. 1994).

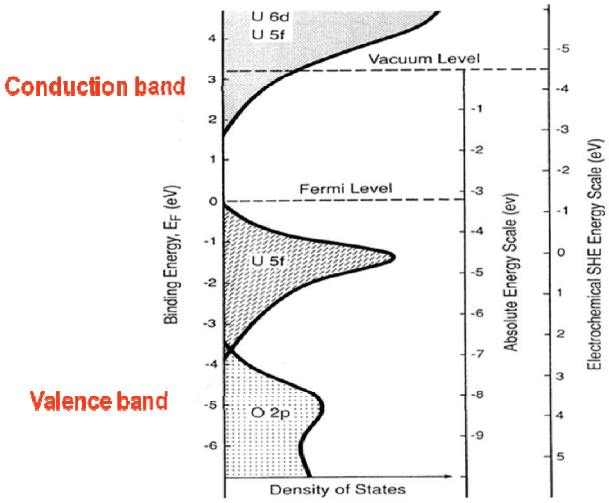


Figure 6: Schematic energy-level diagram for UO_2 derived from spectroscopic and electrochemical data (expressed on the standard hydrogen scale (SHE)). The filled valence band has predominantly O2p character, and the empty conduction band consists mainly of U5f, 6d and 7f states. The U5f band contains two electrons per U atom. A more detailed description of this diagram is given by Shoesmith et al. (1994).

The introduction of nonstoichiometry, in the form of incorporated additional O^{2-} ions accompanied by the creation of U^{V} atoms to maintain charge balance, creates holes in the 5f band making the electrical conductivity of UO_{2+x} very sensitive to the degree of non-stoichiometry. In addition, non-stoichiometric locations have been shown to provide donor-acceptor (U^{IV}/U^{V}) sites which catalyze the cathodic reduction of O_2/H_2O_2 (Hocking et al. 1994; Goldik et al. 2004) as illustrated schematically in Figure 7A. If these locations (shown as grain boundaries in Figure 7B) also exhibit enhanced anodic reactivity (i.e., more rapid oxidation and dissolution than stoichiometric locations) then they could be preferential corrosion sites.

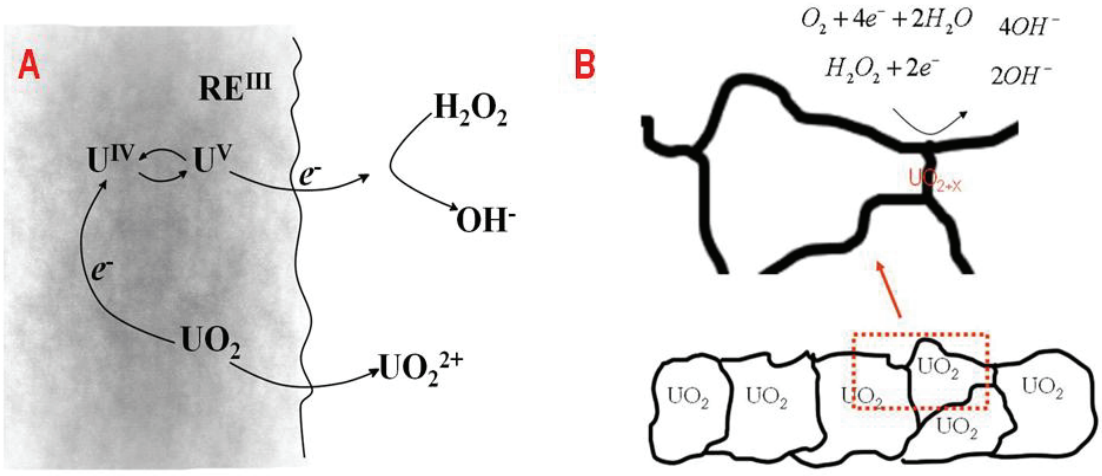


Figure 7: Schematic, A, illustrating how non-stoichiometric locations UO_{2+x} (U^{IV}/U^{V}) provide donor-acceptor sites which catalyze the cathodic reduction of oxidants, such as O_2 and H_2O_2, and promote UO_2 corrosion. As illustrated in B, non-stoichiometric locations might be expected at grain boundary locations.

To enable the study of these influences on fuel reactivity, various custom-fabricated fuel specimens have been used, ranging from SIMFUELs with various degrees of simulated in-reactor burn-up to specimens with controlled degrees of nominal non-stoichiometry (x in UO_{2+x}). SIMFUELs are natural UO_2 doped with non-radioactive fission products (Ba, Ce, La, Mo, Sr, Y, Zr, Rh, Pd, Ru, Nd) to replicate the chemical effects of in-reactor burn-up (Lucuta et al. 1991). The SIMFUELs used ranged from 1.5 at% burn-up (14 GWd/MgU, typical of a high burn-up CANDU fuel), to 3 at% (28 GWd/MgU) and 6 atom % (56 GWd/MgU, corresponding to a high burn-up LWR fuel). Non-stoichiometric specimens with nominal O/U ratios of 2.002, 2.011, 2.05 and 2.1 were prepared using a coulometric titration apparatus which has been described in detail elsewhere (Verrall et al. 2005; Corcoran et al. 2007).

3. CHARACTERIZATION OF SIMULATED FUEL PROPERTIES

3.1 RAMAN SPECTROSCOPY OF URANIUM DIOXIDE

Although a number of analytical techniques have been used to characterize fuel specimens, and will be described below when appropriate, Raman spectroscopy has proven a most useful technique since it can detect intermediate range order making it sensitive to small distortions of the O-sublattice. By contrast, the smaller X-ray scattering factor for O compared to that of U makes X-ray diffactometry (XRD) insensitive to changes in the O-sublattice. Here the basic features of Raman spectra observed for UO_2 are described, based on a more detailed discussion of the application of Raman spectroscopy to the analysis of UO_2 published elsewhere (He and Shoesmith 2010).

Figure 8 shows a Raman spectrum recorded on sintered UO_2 with a composition close to stoichiometric. The key features in this spectrum can be described as follows:

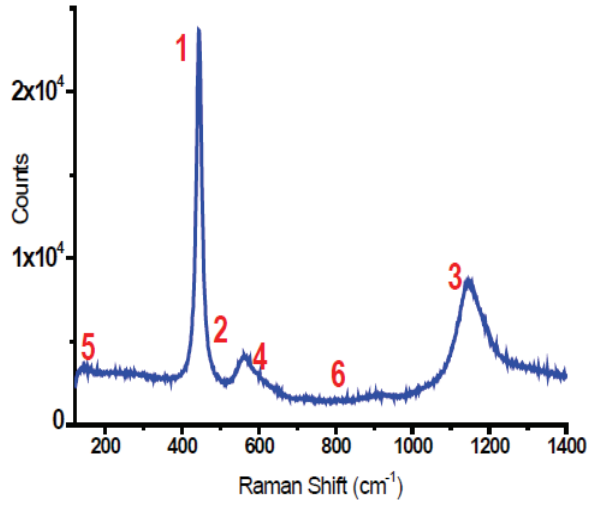


Figure 8: A Raman spectrum recorded on sintered UO_2 with a composition close to stoichiometric. The numbers show the key features observed in the spectrum (1, 3, 4) or expected to develop as the fuel becomes more oxidized (5, 6).

(i) The dominant peak at 445 cm^{-1} (1 in Figure 8) can be attributed to the fundamental O-U stretch in the cubic UO_2 lattice. A loss of intensity in this peak would indicate deviations from the perfect cubic fluorite structure.

(ii) Although not observed in this spectrum, a shoulder around 470 cm^{-1} (2 in Figure 8) would suggest the development of a tetragonal structure; i.e., a distortion of the cubic lattice along one axis.

(iii) The broader peak located at 1150 cm^{-1} (3 in Figure 8) is an L-O phonon band (actually an overtone of the L-O phonon band located at 575 cm^{-1}). Since this peak is attributed

to vibrations of the lattice it is sensitive to lattice distortions and can be considered a fingerprint for the fluorite structure (Livneh and Sterer 2006).

(iv) The broad multi-component band in the region 500 to 700 cm^{-1} (4 in Figure 8) is indicative of lattice damage due to the presence of defects and will be discussed in more detail below.

(v) Although not present in this spectrum the appearance of a peak at 155 cm^{-1} (5 in Figure 8, to be discussed below) would be indicative of a tetragonal structure induced by major distortions of both the O and U sublattices.

(vi) The very shallow peak in the region 800 to 900 cm^{-1} (6 in Figure 8), which suggests the presence of uranyl ion-containing phases, could be due to slight air oxidation of the sintered UO_2 surface.

3.2 SIMFUEL PROPERTIES

Prior to determining the electrochemical reactivity, the SIMFUEL specimens were characterized by X-ray diffractometry (XRD), Raman spectroscopy, X-ray photoelectron spectroscopy (XPS) (He et al. 2007) and time-of-flight Secondary Ion Mass Spectrometry (ToF-SIMS) (Broczkowski 2008; Broczkowski et al. 2010).

XRD analyses showed that the fluorite structure of the UO_2 lattice was retained but with a close to linear decrease in lattice constant with an increase in simulated burn-up. Comparison of XRD patterns to those recorded on fuels doped to various Zr levels (Shoesmith et al. 2005; Paschol et al. 1987) shows the SIMFUEL matrices were only lightly Zr-doped, indicating major segregation of Zr to the ABO_3 perovskite phase. SEM/EDX confirmed that a large amount of the Zr was incorporated in to a primarily Ba/Zr perovskite, i.e., $BaZrO_3$.

Figure 9 shows averaged Raman spectra for the three SIMFUELS obtained from a series of spot analyses. The characteristic fundamental U-O stretching mode (1) (445cm^{-1}) and the peak at 1150 cm^{-1} (3) both decrease with increased doping (degree of simulated burn-up). The loss in intensity in these two peaks accompanied by the consistent changes in the 575 cm^{-1} and 640 cm^{-1} peaks (4) associated with lattice distortions (He and Shoesmith 2010) indicate a regular change in the nature of the defect clusters thought to be formed by the rare earth dopants and the associated oxygen vacancies created. It is this increased defect clustering which leads to the lattice contraction observed by XRD (Park et al. 1997; Park and Olander 1992).

The influence of rare earth doping on conductivity of the UO_2 matrix is shown in the resistivity values for these SIMFUELs compared to similarly fabricated pellets containing either only rare earth dopants or only noble metal particles, Table 1. While the resistivity does not change consistently with the degree of doping, the decrease when rare-earths are present is clear. The resistivity of the SIMFUEL containing only noble metal (ε) particles can be taken to be that of undoped UO_2 when close to stoichiometric.

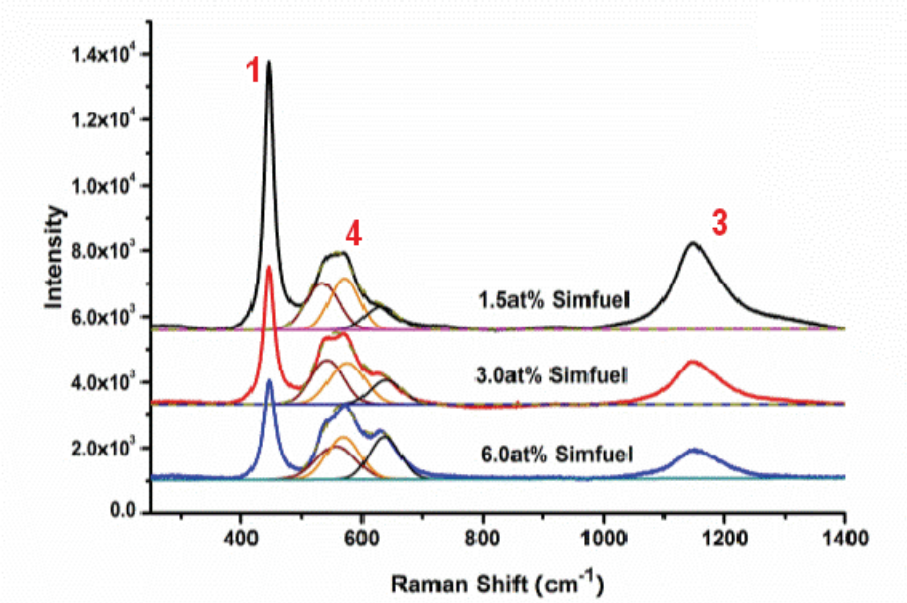


Figure 9: Averaged Raman spectra for three SIMFUELs with different degrees of simulated burn-up (see Table 1). Averaged spectra were obtained by point-by-point (2 μm per step) mapping over a 40 μm linear region. The numbers refer to the spectral features illustrated in Figure 8 and described in the text.

Table 1: Resistivity of various SIMFUEL specimens

Designation	Material	Resistivity (ohm.cm)
SF1	1.5 at%	182
SF2	3.0 at%	81
SF3	6.0 at%	1120
SS1	3 at% (rare earths only)	174
SS2*	3 at% (ε-particles only)	15400

*The resistivity of undoped UO_2 would be similar to that of SS2.

Figure 10 shows the distribution of noble metal (ε) particles for the three SIMFUELs with various degrees of simulated burn-up covering the range from the level expected for CANDU fuel (1.5 at%) to that expected for very high burn-up enriched fuel (6 at%). This distribution was obtained from ToF-SIMS analyses for the individual elements in the particles. The increase in size and number density of particles with the degree of simulated burn-up is clear.

These analyses show that the fabrication process for SIMFUELs simulates two important features of irradiated fuel: (i) it creates noble metal (ε) particles; and (ii) it increases the conductivity of the UO_2 matrix by rare earth doping. Since noble metals are well known as catalysts for oxidation/reduction reactions, and three of the four predominant constituents of these particles (Rh, Pd, Ru) are exceptionally good catalysts (Broczkowski 2008; Norskov et al. 2008), they would be expected to act as cathodes and/or anodes galvanically coupled to the conductive, and potentially reactive, rare earth-doped UO_2 matrix, as illustrated schematically in Figure 11. The question mark in Figure 11B indicates that while reduction of U^{V} to U^{IV} within

the lattice is expected it is unproven whether this galvanically-coupled process can reduce soluble U^{VI} (as UO_2^{2+}).

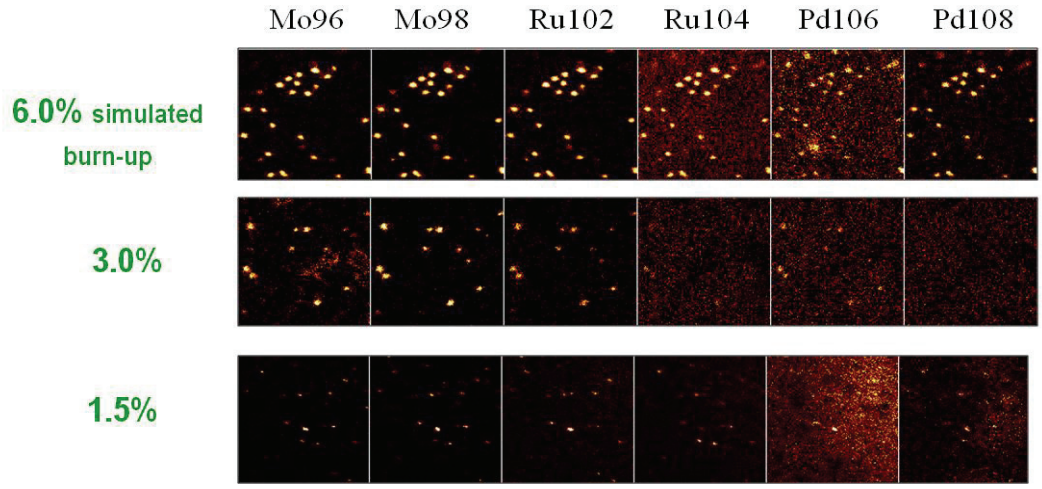


Figure 10: ToF-SIMS images showing the distribution of noble metal (ε) particles in three SIMFUELs with different degrees of simulated burn-up. The distributions were obtained from analyses of individual elements ($^{96, 98}$Mo, $^{102, 104}$Ru and $^{106, 108}$Pd). No map for Ru is shown due to its low concentration. Each individual area is 50 μm x 50 μm.

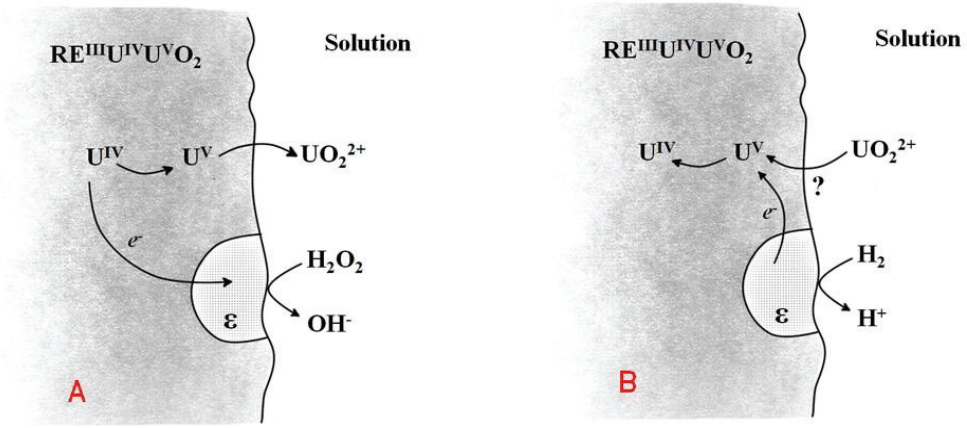


Figure 11: Schematic illustrations of how noble metal (ε) particles can act either as preferential cathodes supporting oxidant reductions (A) or preferential anodes suppporting reductant oxidation reactions (B).

4. THE INFLUENCE OF RARE EARTH – DOPING ON FUEL REACTIVITY

Using this range of SIMFUEL specimens, a preliminary investigation of the influence of fission product doping (with the primary emphasis on RE^{III}) on the electrochemical reactivity of UO_2 was performed (He et al. 2007). Figures 12A and 12B show the voltammetric behavior of all three SIMFUELs recorded in buffered and unbuffered solutions. As indicated on Figure 12B, for buffered conditions, anodic oxidation of UO_2 occurs in two stages: to UO_{2+x} in the potential region -0.1 to 0+1V and then to $UO_3 \bullet yH_2O$ at higher potentials. In unbuffered solutions, Figure 12A, a similar oxidation sequence is observed except the currents are increased by the development of local acidity (due to hydrolysis of UO_2^{2+})

$$n\,UO_2^{2+} + yH_2O \rightarrow ((UO_2)_n(OH)_y)^{(2n-y)+} + yH^+ \qquad (1)$$

at more positive potentials.

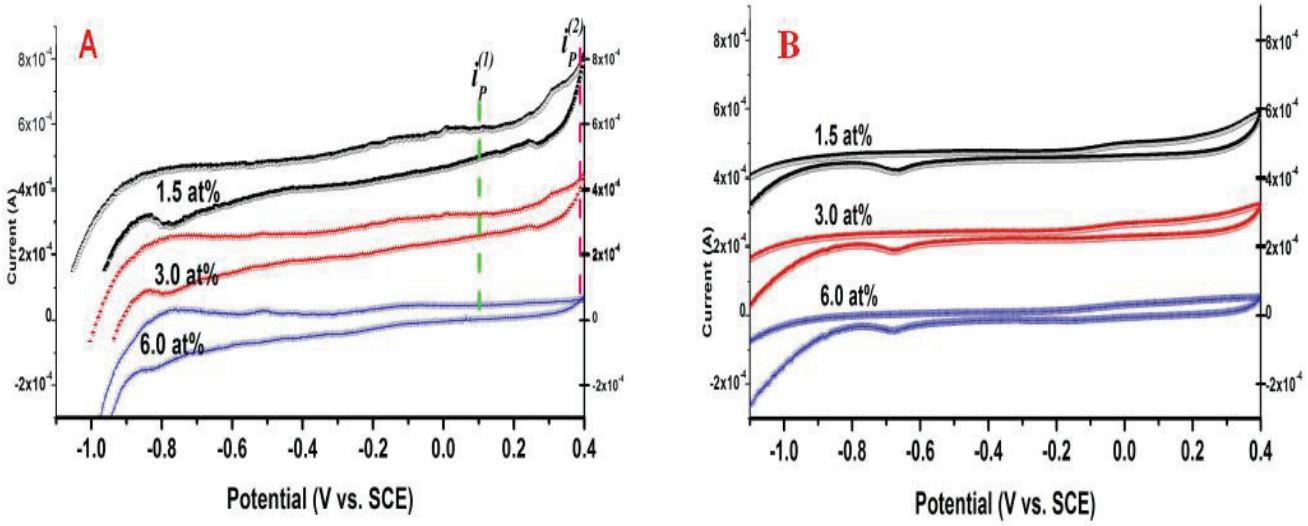


Figure 12: Voltammograms recorded on three SIMFUELs with different degrees of simulated burn-up in (A) 0.1 mol.L^{-1} NaCl at pH 9.5, and in (B), borate buffered 0.1 mol.L^{-1} NaCl at pH 9.5. The stages of oxidation described in the text are indicated by the vertical dashed lines in (A).

To emphasize the influence of simulated burn-up, the currents at +0.1V, representative of the first stage of oxidation ($UO_2 \rightarrow UO_{2+x}$), and +0.4V, representative of the second stage of oxidation ($UO_{2+x} \rightarrow UO_2^{2+}$ or $UO_3 \bullet yH_2O$) are plotted for all three SIMFUELs in Figure 13. At 0.1V the decrease in current with increase in simulated burn-up is small and effectively independent of solution buffering. This indicates a measurable but marginal influence of doping on the surface oxidation of the UO_2 lattice (i.e., O^{2-} injection at oxygen vacancy locations accompanied by oxidation of 2 U^{IV} atoms to U^{V}). The lack of any significant effect of buffering

at this potential is not surprising considering the negligible solution pH change caused by the formation of a thin surface layer to UO_{2+x}.

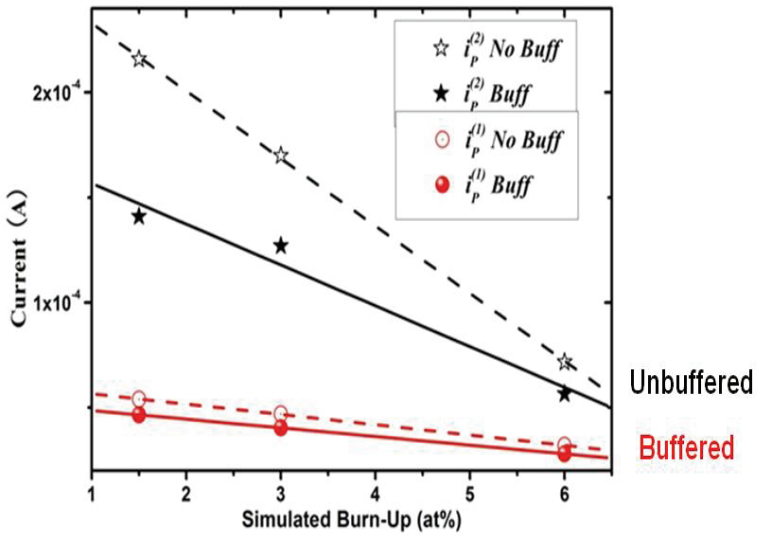


Figure 13: Current densities $i_p^{(1)}$ and $i_p^{(2)}$ recorded at the potentials indicated in Figure 12, for oxidation ($UO_2 \rightarrow UO_{2+x}$; $i_p^{(1)}$) and dissolution ($UO_{2+x} \rightarrow UO_2^{2+}$; $i_p^{(2)}$) in buffered and unbuffered solutions as a function of the degree of simulated burn-up of the three different SIMUFUELs.

By contrast, the influence of doping on the anodic dissolution/film deposition process at 0.4V is much more marked. As expected the presence of the buffer decreases the current for the dissolution of all SIMFUEL specimens. According to Figure 13, an increase in simulated burn-up from 1.5 at% to 6 at% leads to a decrease in oxidation current by a factor of 2.5 to 5.0 depending on whether a buffer is present or not. The very small influence of buffering on the anodic dissolution current for 6 at% SIMFUEL reinforces the argument that doping to this level stabilizes the fluorite lattice against anodic oxidation and dissolution, thereby preventing the formation of soluble and hydrolyzable UO_2^{2+}.

Figure 14, A to C, shows the influence of temperature on the voltammetric behavior of the three SIMFUELs recorded in buffered 0.1M KCl solution (pH ~9.5). For 1.5 at% and 3 at% SIMFUEL the currents observed in both oxidation regions (marked 1 ($UO_2 \rightarrow UO_{2+x}$) and 2 ($UO_{2+x} \rightarrow UO_3.yH_2O$) increase with temperature although there is some evidence that the current is suppressed by the deposition of $UO_3.yH_2O$ at positive potentials at higher temperatures. This is particularly clear for 1.5 at% SIMFUEL, Figure 14A. Despite the buffering, there is also evidence for localized acidification (particularly for the 3 at% SIMFUEL), leading to the reduction of UO_2^{2+} in the potential region -0.2V to -0.3V, presumably trapped in unbufferred occluded regions on the rough electrode surface (Santos et al. 2006). By contrast, the anodic current for these two processes is considerably lower and the temperature dependence muted for 6 at% SIMFUEL. Consistent with this lower anodic reactivity there is no evidence for the reduction of UO_2^{2+} in acidified locations, Figure 14C.

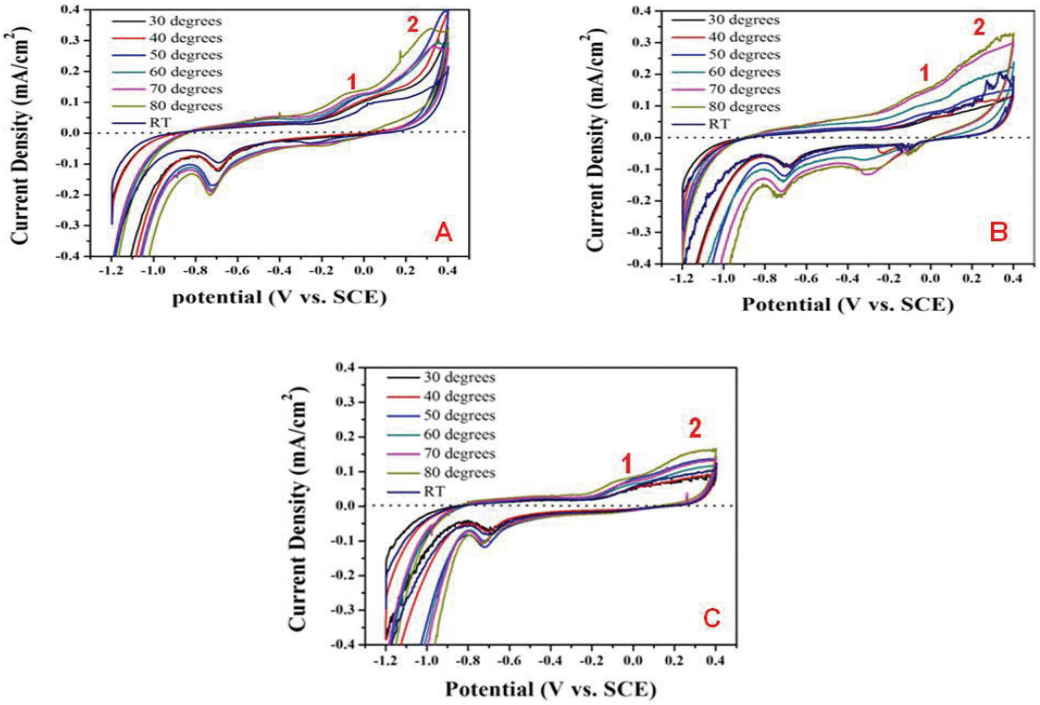


Figure 14: The Influence of temperature on the currents recorded in voltammograms for three different SIMFUEL electrodes with different degrees of simulated burn-up in buffered 0.1 mol.L^{-1} NaCl (pH 9.5); (A) 1.5 at% (B) 3.0 at%; (C) 6.0 at%. The two stages of oxidation described in Figure 13 are labelled 1 and 2.

While these electrochemical results must be considered preliminary they provide consistent evidence that rare-earth doping should suppress the corrosion of UO_2 under aqueous conditions in a similar manner to its suppression of fuel oxidation in air.

5. THE INFLUENCE OF NON-STOICHIOMETRY ON FUEL REACTIVITY

5.1 CRYSTALLINE STRUCTURE OF UO_2

Crystalline UO_2 can be described as a face centered cubic (fcc) sublattice of U^{4+} ions within a simple cubic O^{2-} sublattice to form a fluorite structure. Within this structure, U is coordinated by eight equivalent oxygen atoms at the corners of a cube, each of which is in turn surrounded by a tetrahedron of four equivalent U atoms. Of all the basic lattice structures, the fluorite one is the most flexible and capable of generating many derivative structures. This can be attributed to the existence of a large number of octahedral holes, which gives UO_2 the ability to accommodate large amounts of interstitial O to form hyperstoichiometric UO_{2+x} as illustrated in Figure 15. Incorporation of O occurs readily since the energy of formation of O interstitials is negative (Crocombette et al. 2001; Freyss et al. 2005; Gupta et al. 2007; Geng et al. 2008; Nerikar et al. 2009). This, and the ability of U to form multiple oxidation states (U^{IV} to U^{VI}),

allows the formation of a complex family of binary metal oxides within the range UO_2 to U_3O_7 (Conradson et al. 2004).

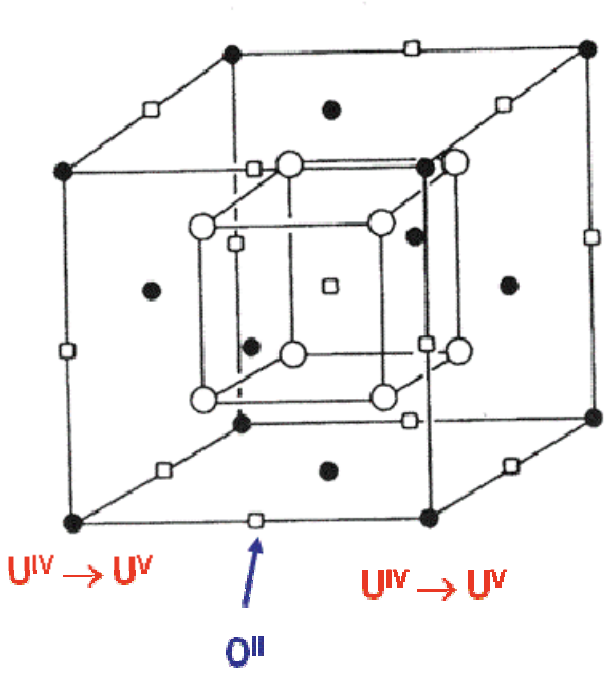


Figure 15: Schematic showing the cubic fluorite structure adopted by uranium dioxide and other actinide dioxides; ●-U atoms; o-O atoms; □-cubically coordinated empty lattice sites. The introduction of non-stoichiometry in the form of O^{II} ions accompanied by the formation of U^{V} atoms to maintain charge balance is illustrated.

The introduction of non-stoichiometry in the form of O^{2-}, accompanied by the formation of U^{V} atoms to maintain charge balance, increases the electrical conductivity of the oxide and provides donor acceptor (U^{IV} / U^{V}) sites in the surface of the oxide which have been shown to catalyze oxidant reduction reactions (Hocking et al. 1994; Goldik et al. 2004). This introduces the possibility that the overall corrosion process will be accelerated as illustrated in Figure 7A. In addition, there is the possibility that the structural changes in the UO_2 lattice due to addition of O will influence the anodic kinetics of the corrosion process, i.e., of the reaction $UO_2 \rightarrow (UO_2)^{2+}$, Figure 7A.

5.2 MATRIX PROPERTIES OF NON-STOICHIOMETRIC UO_{2+x}

To determine whether the above reaction occurs, a number of experimental approaches have been adopted: (a) Raman spectroscopy was used to characterize the changes in matrix structure; (b) surface physical changes (i.e., the accumulation of corrosion damage) were investigated using, atomic force microscopy (AFM); (c) current-sensing atomic force microscopy (CS-AFM) was used to relate surface structures to physical properties, such as electrical conductivity; (d) electrochemical techniques were used to relate these surface properties to changes in the corrosivity of UO_2 with variations in non-stoichiometry. Since these studies were conducted on UO_{2+x} specimens which varied laterally in surface properties,

scanning electrochemical microscopy (SECM) was employed to determine local electrochemical reactivities.

The influence of various degrees of non-stoichiometry on Raman spectra were characterized using a specimen of UO_2 with a nominal stoichiometry of $UO_{2.1.}$ Figure 16 shows that the surface of this specimen exhibits four distinct features which can be distinguished according to the relationship between their topography and composition (determined approximately by energy dispersive X-ray (EDX) analyses):

(i) the smooth flat grains (A in Figure 16) are close to stoichiometric;
(ii) the grains with very shallow stepped patterns (B in Figure 16) are slightly hyper-stoichiometric, with $x \leq 0.13$;
(iii) the grains with a pronounced step pattern of ridges oriented horizontally along the *x*-y plane (C in Figure 16) are more non-stoichiometric, with $0.13 \leq x \leq 0.24$;
(iv) grains with vertically developed terraces (D in Figure 16) are highly non-stoichiometric, with $0.25 \leq x \leq 0.033$.

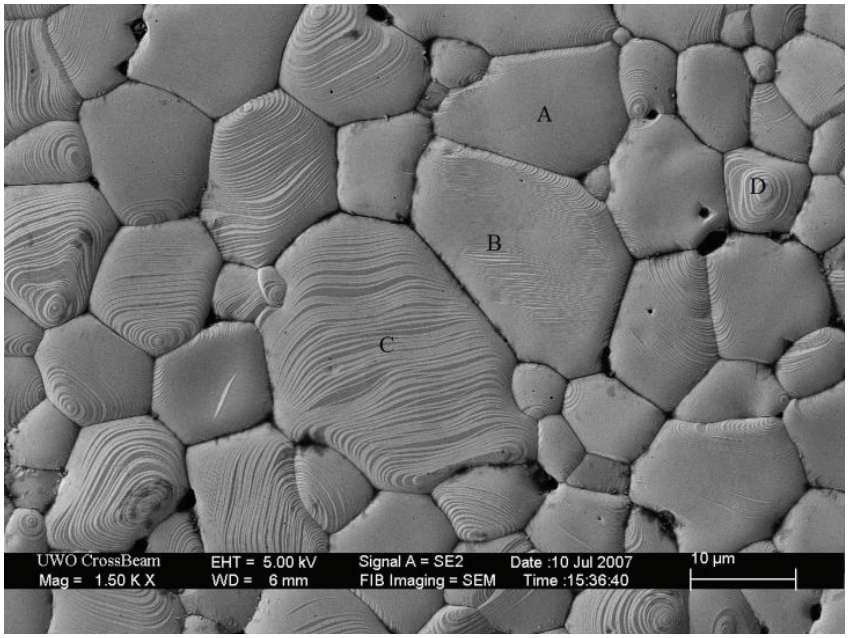


Figure 16: SEM image of a typical surface morphology observed on a uranium dioxide specimen with a nominal stoichiometry of $UO_{2.1}$. (A) a smooth flat grain with an approximate O/U ratio of ~2.01; (B) a grain with a very shallow stepped pattern with a slightly hyperstoichiometric composition of ~2.15; (C) a grain with a pronounced stepped pattern of ridges oriented horizontally along the x – y plan with a composition of ~2.22; (D) a highly non-stoichiometric spiral-like grain with a composition of ~2.31.

Figure 17 shows Raman spectra recorded on the four types of grains, and their inspection demonstrates the following:

(i) a loss of intensity in bands (1) and (3) associated with deviations from the fluorite structure (see Figure 8 for band numbers);
(ii) an increasing importance of the multicomponent band (4) attributed to “lattice damage”;
(iii) the appearance of band 5 due to tetragonal distortions at extreme non-stoichiometry which coincides with the disappearance of band 3.

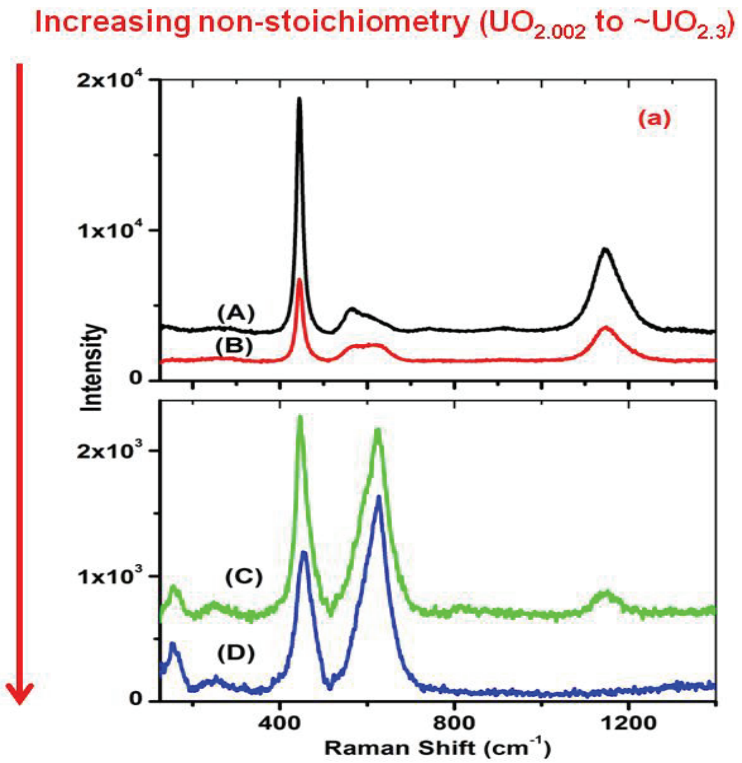


Figure 17: Raman spectra recorded on the four types of grains (A) to (D) described in Figure 16. The O/U ratio is ~2.01, 2.15, 2.22 and 2.31 for (A), (B), (C) and (D), respectively.

The loss of intensity in band 1 (445 cm^{-1}) is accompanied by the appearance of the shoulder on the high frequency side which, on deconvolution of the band, yields the peak at 470 cm^{-1} (2), Figure 18, attributed to tetragonal distortion of the O sublattice at high degrees of non-stoichiometry. The very broad band (4 in Figure 18) can be deconvoluted into two bands at 575 cm^{-1} and 630 cm^{-1}, 4A and 4B in Figure 18. The intensity of peak 4A decreases with that of band 3 (1150 cm^{-1}), Figure 17, and it is claimed (Livneh and Sterer 2006) that these bands are related, peak 4A being the L-O phonon band and peak 3 the overtone (2L-O). The development of peak 4B, Figure 18, has been attributed to O sublattice distortions due to the O ion displacements required to accommodate the increasing amounts of excess O and is accompanied by the development of the peak at 155 cm^{-1}(Figure 17) indicative of distortion of both the O and U sublattices.

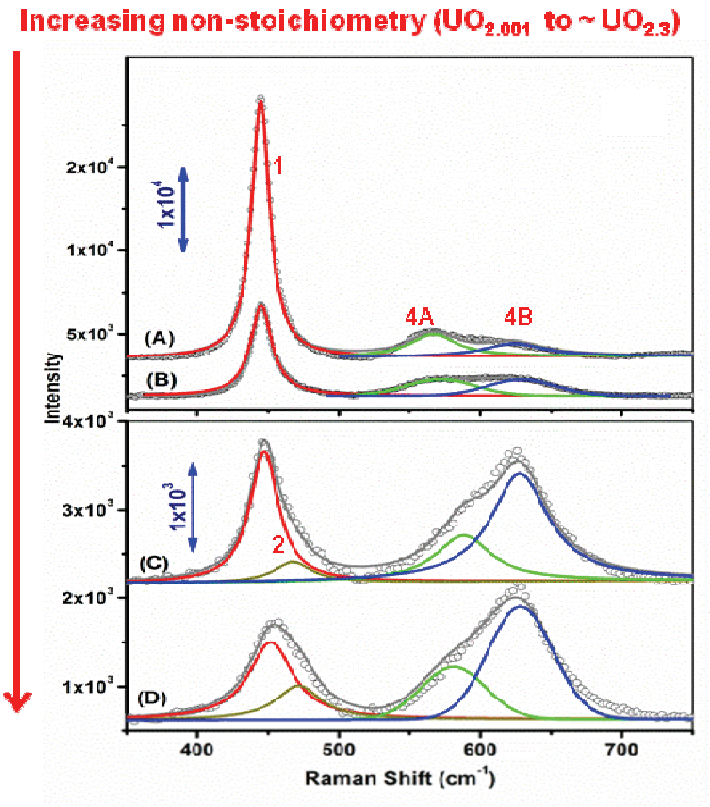


Figure 18: Sections of the Raman spectra shown in Figure 17 showing the deconvolution of the two pairs of contiguous bands at 445cm^{-1} (1) / 470cm^{-1} (2) and 575cm^{-1} (4A) / 630cm^{-1} (4B). The O/U ratio is ~2.01, 2.15, 2.22 and 2.31 for specimens (A), (B), (C) and (D), respectively.

Using an extensive series of Raman spot analyses, the relationships between the various bands and their connection to lattice structure were developed. The relationships between bands 1 (445 cm^{-1}), 3 (1150 cm^{-1}) and 5 (155 cm^{-1}) are shown in Figure 19. The points labeled A to D are the intensities of the spectra shown in Figure 17, and the vertical lines indicate transitions between various defect regions. The compositional scale (based on many EDX and XRD local analyses) locates the approximate degree of non-stoichiometry at which these transitions occur.

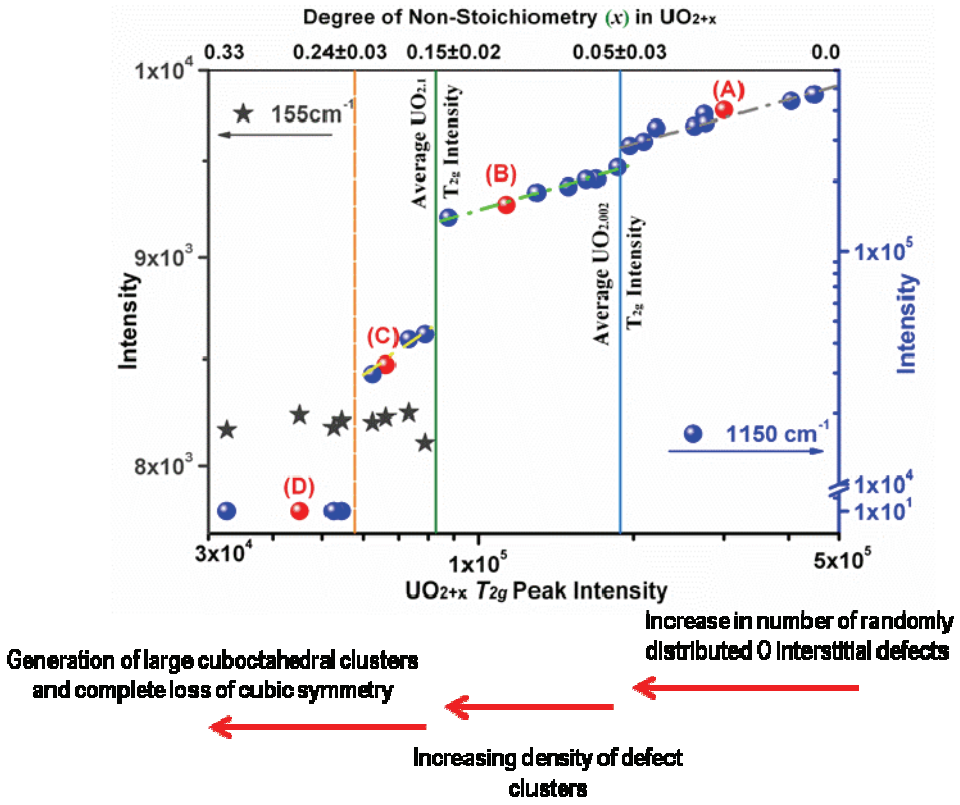


Figure 19: The relationships between Raman bands 1 (445 cm^{-1}), 3 (1150 cm^{-1}) and 5 (155 cm^{-1}) based on an extensive series of Raman spot analyses. The points A to D show the peak intensities taken from the spectra shown in Figure 17, and the vertical lines indicate transitions between various defect regions. The compositional scale (based on many EDX and XRD analyses) locates the approximate degree of non-stoichiometry at which these transitions occur.

While a more extensive discussion of this figure is given elsewhere (He and Shoesmith 2010), three very general categories can be established as indicated by the arrows in Figure 19. For relatively low degrees of non-stoichiometry there is an increase in the number of randomly distributed O interstitial defects. As the degree of non-stoichiometry increases these defects begin to associate into clusters whose number increases with x (UO_{2+x}). For a sufficiently high degree of non-stoichiometry large cuboctahedral clusters are generated leading to a major loss of cubic symmetry. The cuboctahedral cluster is the most densely packed defect cluster which minimizes the damage to the UO_2 lattice induced by incorporation of excess O by optimizing the spatial distribution of vacancies and interstitials (Bevan et al. 1986, Garrido et al. 2003, Willis 1987).

5.3 SURFACE PROPERTIES OF NON-STOICHIOMETRIC UO_{2+x}

The above studies clearly indicate that the bulk structure of UO_{2+x} changes as the value of x changes. However, corrosion/dissolution is a surface/interfacial process. The connection between the structural properties of the matrix and the properties of the surface was studied using current-sensing atomic force microscopy (CS-AFM). While this technique cannot be used in-situ to study corrosion/dissolution in progress, it can be used to simultaneously map surface topography and determine the local conductivity, both key properties of a surface undergoing corrosion. Since the electrical conductivity of UO_{2+x} is related to its degree of non-stoichiometry (Hyland and Ralph 1983) the variations in composition with location are expected to be reflected in the measured conductivity. The principle of this technique is illustrated in Figure 20.

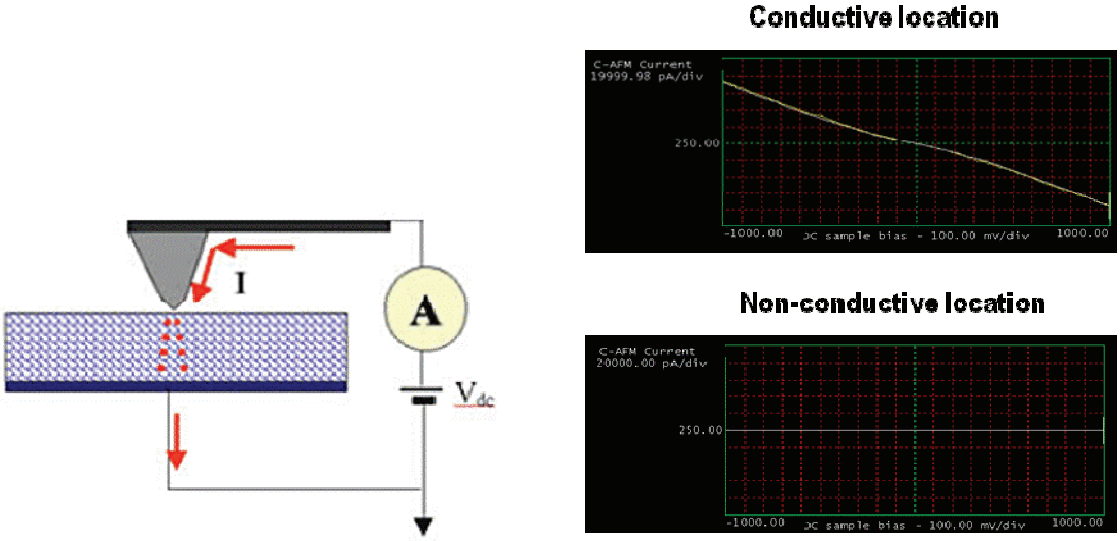


Figure 20: Schematic showing the principle behind the technique of current-sensing atomic force microscopy (CS-AFM). A DC bias potential is applied to the microscopy probe tip while the specimen (in the present case UO_{2+x}) is held at ground potential and the current passing through the tip and the specimen is measured. Both topographic and conductivity images are then generated simultaneously by scanning the tip across the surface allowing correlation of the surface features and the local conductivity (O'Neil at al. 2007, 2008). Also shown are two examples of the tip current-potential (I-V) bias plots recorded on a conductive and a non-conductive location.

In the images in subsequent figures, the current, which is proportional to conductivity, is plotted as a function of location for a set bias potential of 0.5V. The current scales given in the images in Figures 22 to 25 indicate the range from completely dark to totally bright. This yields an approximate measure of conductivity. More accurate values can be obtained from current-potential bias plots for specific locations.

Measurements of this kind were performed on a series of 4 specimens with different nominal degrees of non-stoichiometry, Figure 21. Figures 22 to 25 show AFM, CS-AFM and Raman spot analyses performed on these four specimens. Surface features similar to those in the SEM image are observed, and comparison of the topographic and current images reveals a distinct correlation between the topography and the local conductivity.

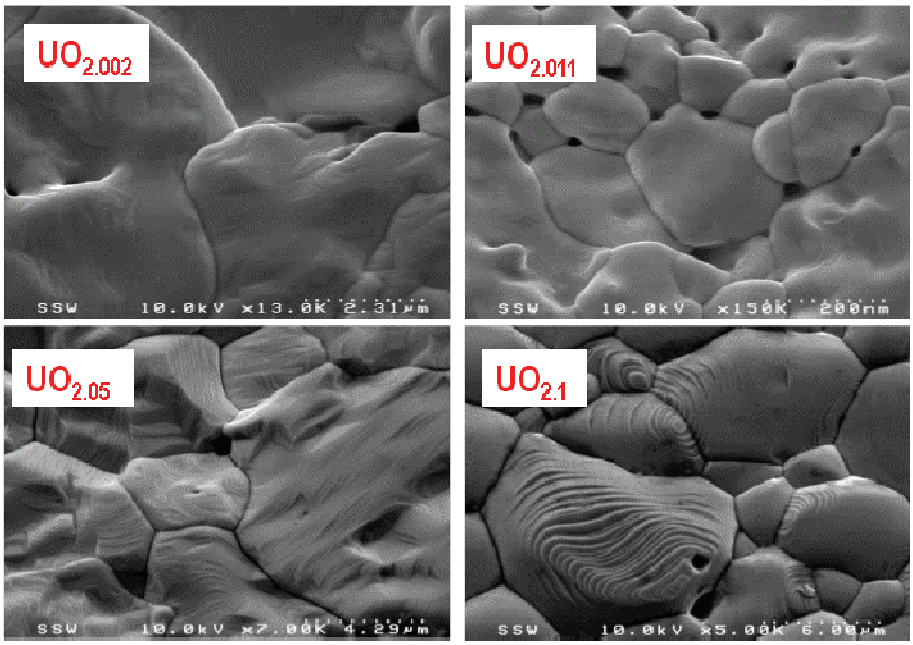


Figure 21: SEM micrographs of four UO_{2+x} specimens with different nominal degrees of non-stoichiometry. Note: the scales of these four micrographs are not the same.

The featureless grains which dominate the surface of the $UO_{2.002}$ specimen exhibit a generally uniform conductivity with some non-conducting locations, some of which are associated with surface voids, Figure 22. The minor variation in the intensity of the 455 cm^{-1} Raman band is consistent with these observations and confirms that the cubic symmetry of the lattice is generally maintained. At this degree of non-stoichiometry, the surface exhibits a generally random distribution of point defects (O interstitial ions) as expected for this composition based on the Raman results shown in Figure 19.

For the specimen with a nominal stoichiometry of $UO_{2.011}$ the conductivity varies from grain to grain and within individual grains, Figure 23. Comparison to the topographic image shows that the smoother flat locations with a composition close to stoichiometric consistently exhibit a low conductivity. By comparison the grains exhibiting stepped patterns, shown to be non-stoichiometric, possess higher conductivities and exhibit some anisotropy in conductivity. There is also an indication of enhanced conductivity in grain boundaries, although this is not common. The Raman spectra show that the cubic symmetry is generally maintained but a considerable variation in the intensities of the 455 cm^{-1} and 1150 cm^{-1} bands is observed consistent with significant variations in stoichiometry from one location to another. The development of anisotropic conductivity on the ridged areas of the surface supports the claim that, as the

degree of non-stoichiometry increases, defect clusters begin to form; i.e., at this nominal composition there is a separation into stoichiometric and ordered defect domains.

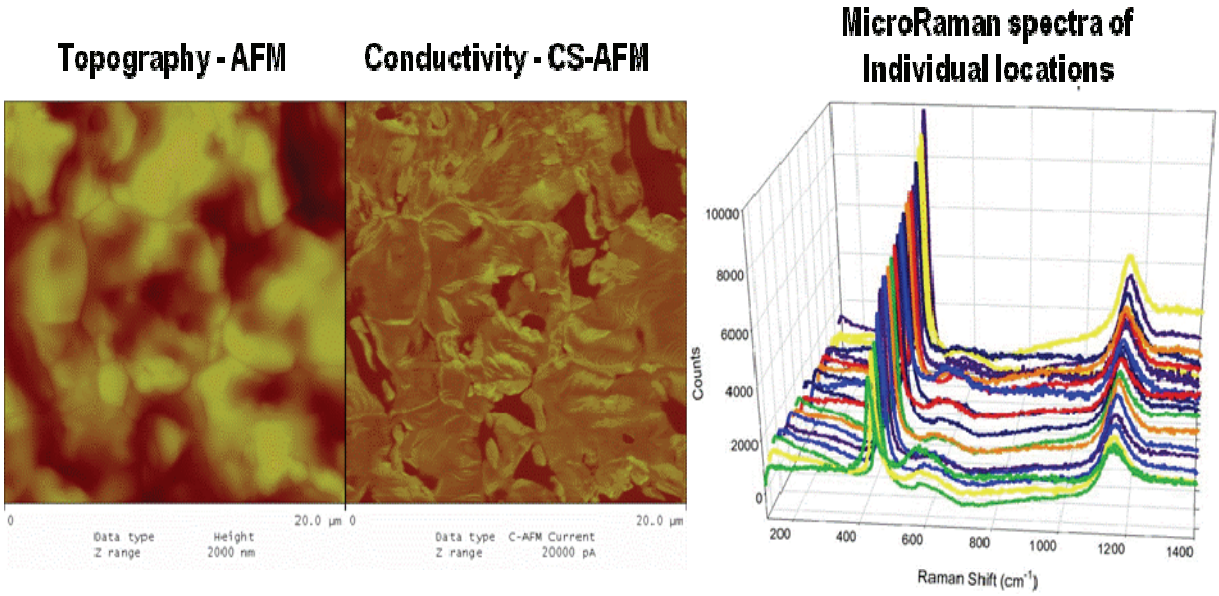


Figure 22: AFM, CS-AFM and spot analyses recorded on the $UO_{2.002}$ specimen (Figure 21). The Raman spectra were recorded at a series of locations and arranged according to the intensity of band 1 (445 cm^{-1}). The CS-AFM image is color-coded according to standard AFM practice with conducting regions shown as bright, and regions of lower activity as dark areas.

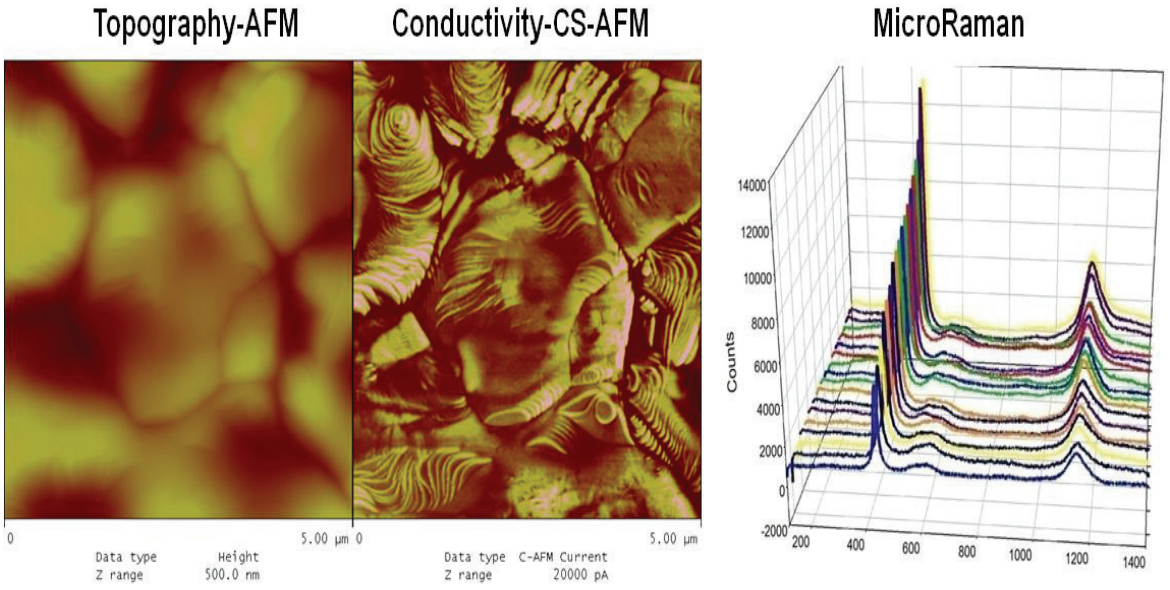


Figure 23: AFM, CS-AFM and Raman spot analyses recorded on the $UO_{2.011}$ specimen (Figure 21). Additional details are given in the legend to Figure 22.

When the nominal non-stoichiometry is increased to $UO_{2.05}$, Figure 24, there is a significant separation into conducting and non-conducting locations. Locations with vertical and horizontally ridged structures develop distinct anisotropic conductivity, consistent with an increased clustering into ordered defects as non-stoichiometry increases. The Raman spectra now show very distinct differences in response from location to location with intense bands at 445 cm^{-1} and 1150 cm^{-1} on smooth locations close to stoichiometric and very weak or absent bands on non-stoichiometric ridged locations with anisotropic conductivity. At this nominal stoichiometry there is an obvious coexistence of stoichiometric cubic locations and areas comprising non-stoichiometric defect clusters.

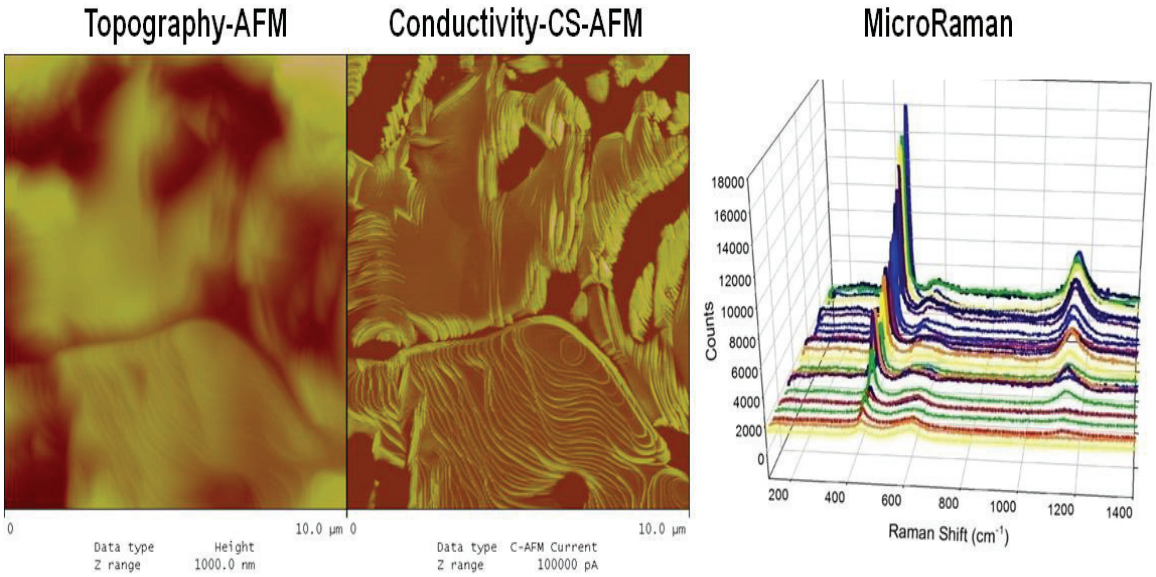


Figure 24: AFM, CS-AFM and Raman spot analyses recorded on the $UO_{2.05}$ specimen (Figure 21). Additional details are given in the legend to Figure 22.

On the $UO_{2.1}$ specimen, Figure 25, there is a very marked separation into conducting and non-conducting locations. The ridged locations exhibit very sharply defined anisotropic conductivity and there is a clear enhancement of conductivity in the grain boundaries. The Raman spectra show that cubic symmetry is maintained only on the few remaining stoichiometric areas. For the ridged non-stoichiometric areas the complete absence of the 1150 cm^{-1} band demonstrates profound distortions of the fluorite lattice to a tetragonal structure.

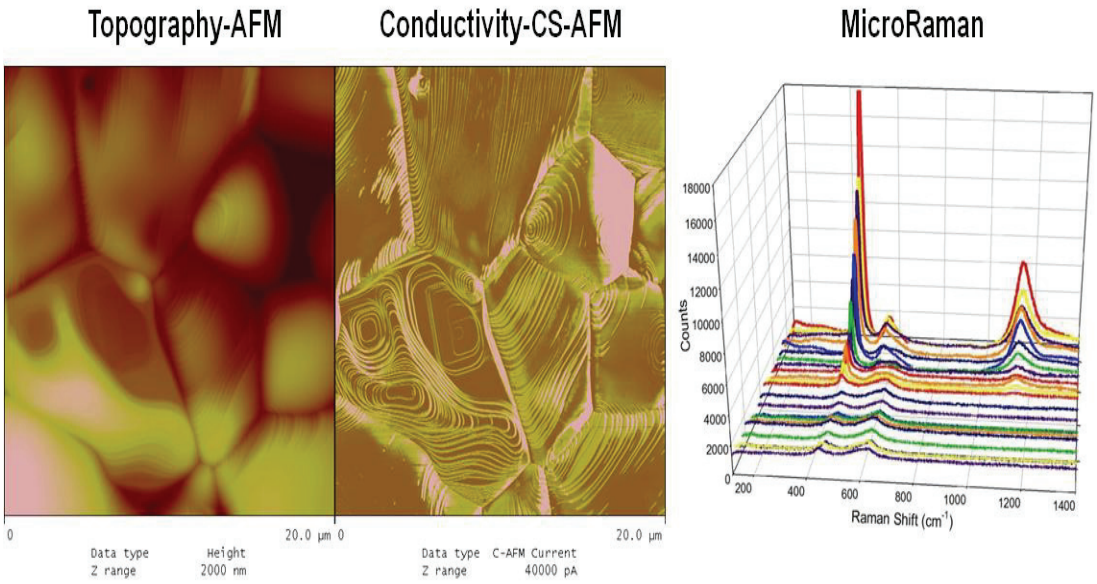


Figure 25: AFM, CS-AFM and and Raman spot analyses recorded on the $UO_{2.1}$ specimen (Figure 21). Additional details are given in the legend to Figure 22.

As discussed above for this particular surface (Figure 18), the appearance of additional Raman bands (470 cm^{-1}, 630 cm^{-1} and 155 cm^{-1}) confirms the conversion to a tetragonal structure at these locations. To emphasize the distribution of structures in the $UO_{2.1}$ specimen, Figure 26 shows three distinct areas within a single grain. The transition from a non-conductive stoichiometric region in the centre of the grain (A), to region B with the uniform moderate conductivity associated with randomly distributed O interstitials, to region C with clustered defects exhibiting anisotropic conductivity is clearly distinguishable.

5.4 RELATIONSHIP BETWEEN SURFACE STRUCTURE/COMPOSITION AND CORROSIVITY

The AFM images shown in Figure 27 confirm that the corrosion damage sustained on the $UO_{2.1}$ specimen is highly localized. This corrosion experiment was conducted in naturally aerated 0.1 mol/L NaCl containing small concentrations of the oxidant ferrocene methanol on a specimen also subjected to short periods of anodic oxidation. The images recorded on the unexposed surface clearly show the ridged structures associated with tetragonally distorted domains, while those recorded after exposure show that the corrosion damage mainly occurred at two locations: on the ridged grain faces and within the grain boundaries; i.e., at the most conductive locations associated with non-stoichiometric defect structures. Figure 28 illustrates the preferential corrosion sites on a hyper stoichiometric surface exhibiting the various features shown in the SEM micrograph in Figure 16.

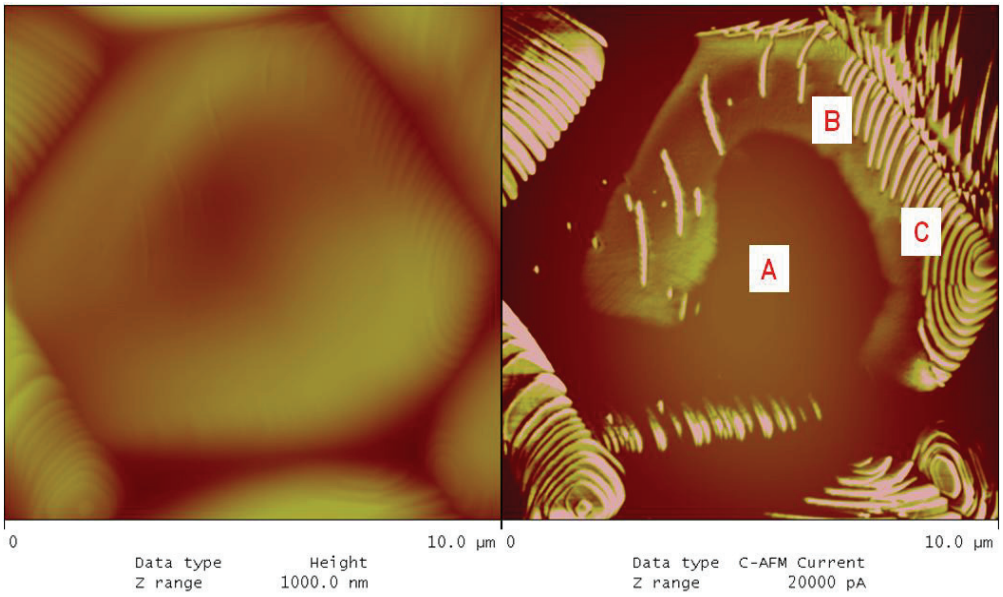


Figure 26: AFM, CS-AFM images recorded on a single grain on the $UO_{2.1}$ specimen (Figure 21): A - a non-conductive stoichiometric region; B - a uniform, moderately conductive region with randomly distributed O interstitials; C - a highly non-stoichiometric region comprising clustered defects exhibiting anisotropic conductivity.

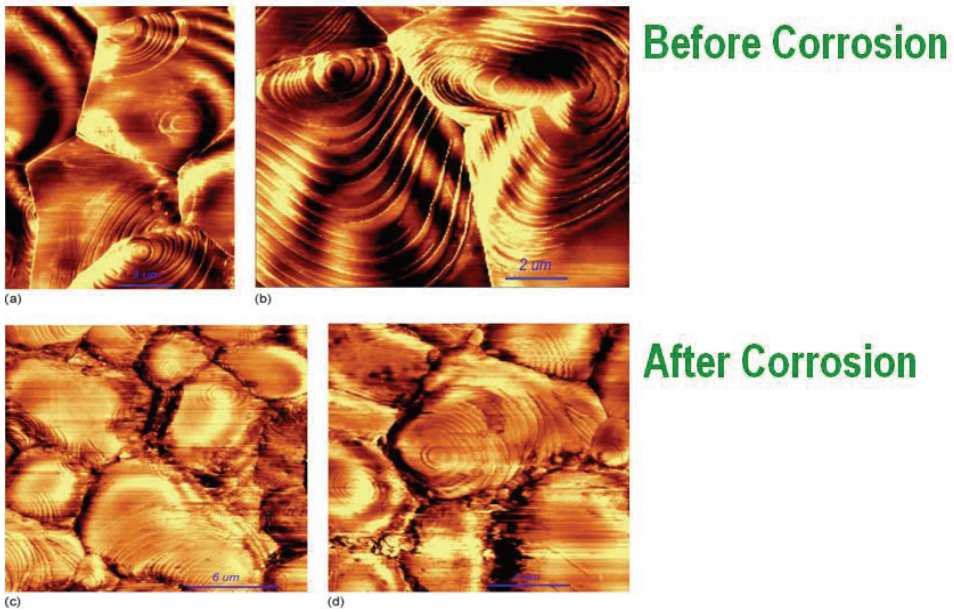


Figure 27: AFM images of the surface of a $UO_{2.1}$ specimen before exposure to solution and after corrosion in a naturally aerated 0.1 mol/L NaCl solution containing a small concentration of the oxidant ferrocene methanol.

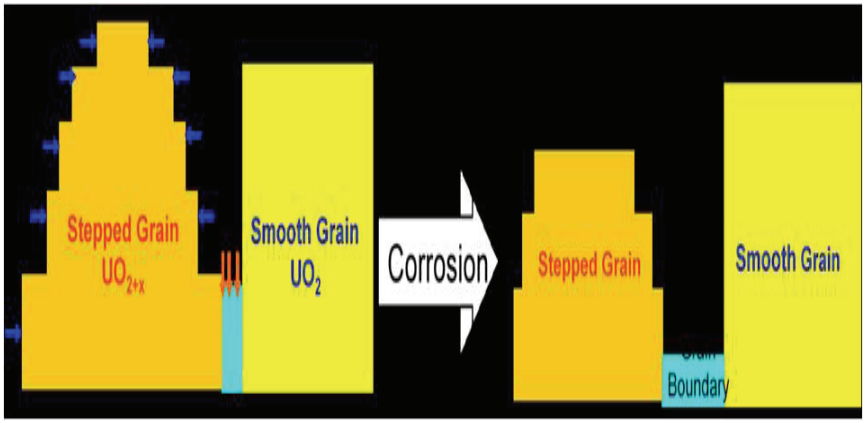


Figure 28: Schematic illustrating the preferential corrosion sites on a hyper stoichiometric surface exhibiting the various features observed in the SEM micrograph in Figure 16.

In an attempt to quantify the reactivities of the various locations on the UO_{2+x} surface, a series of electrochemical experiments were performed. As a basis for comparison, Figure 29 shows a voltammogram recorded on a 1.5 at% SIMFUEL in slightly alkaline sodium chloride solution. This electrode is close to stoichiometric and only rare-earth-doped to a level not expected to significantly influence its reactivity (Section 4).

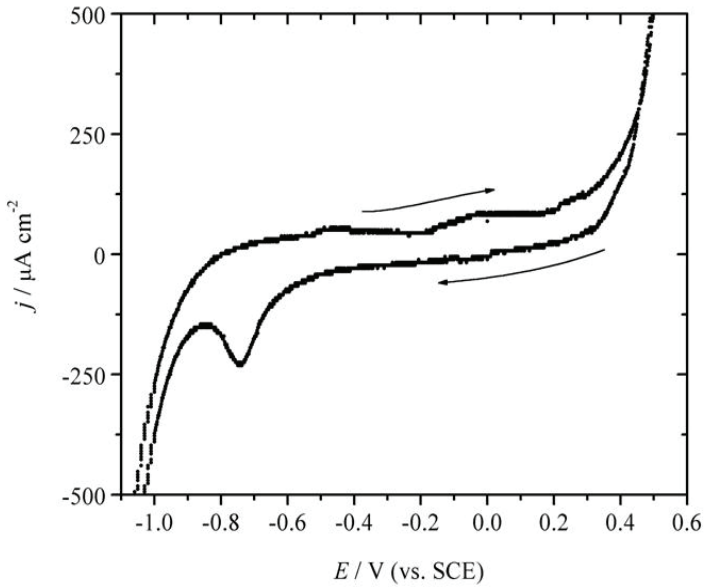


Figure 29: Voltamogram recorded on a 1.5 at% SIMFUEL in 0.1 mol/L NaCl (pH 9.5) at a scan rate of 5 mV/s.

The features observed on the forward and reverse potential scans were described in Section 4 when discussing Figure 12. The sequence of reactions as a function of applied potential was confirmed by X-ray photoelectron spectroscopy (XPS) conducted on this electrode oxidized for 1 hour at individual potentials within the range –500 mV to +500 mV, Figure 30. Oxidation from $U^{IV}O_2$ to $U^{IV}_{1-2x}U^{V}_{2x}O_{2+x}$ commences at potentials ≥ -400 mV to -350 mV (consistent with thermodynamic expectations (Shoesmith 2007)), and the conversion to U^{VI} occurs over the potential range 0 to +300 mV. At very positive potentials, hydrolysis of dissolved UO_2^{2+} leads to local acidification in asperities in the electrode surface and the partial re-dissolution of the U^{VI} surface layer (Santos et al. 2006).

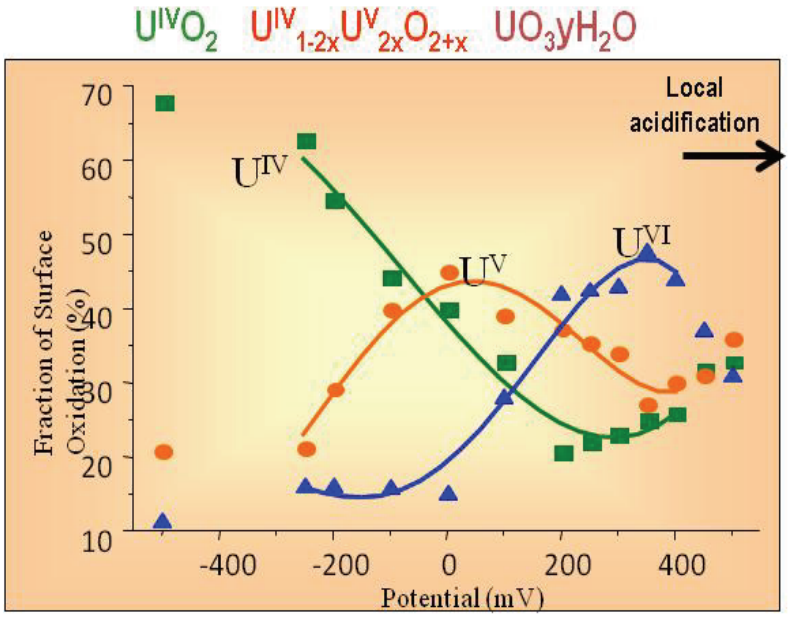


Figure 30: The relative amounts of U^{IV}, U^{IV} and U^{VI} in the surface of a 1.5 at% SIMFUEL electrode determined by XPS after one hour of potentiostatic oxidation in 0.1 mol/L NaCl (pH 9.5) at each individual potential.

Figure 31 shows voltammograms recorded on the four hyper-stoichiometric electrodes in the same solution used in the SIMFUEL experiment. For the two electrodes closest to stoichiometric ($UO_{2.002}$, $UO_{2.011}$) both anodic oxidation and cathodic reduction processes occur in the same potential ranges observed on the SIMFUEL (Figure 29). By contrast, the voltammograms recorded on the $UO_{2.05}$ and $UO_{2.1}$ electrodes show substantial increases in both anodic and cathodic currents. At negative potentials it is noted that the onset potential for H_2O reduction shifts to more positive values with increasing non-stoichiometry, indicating that the presence of non-stoichiometric features on the electrode surface catalyzes this process. In addition, the anodic oxidation process on these two electrodes commences at potentials < -400 mV; i.e., below the oxidation threshold established by XPS (Figure 30) and expected thermodynamically. Also, the extent of oxidation of the surface is increased as indicated by the large cathodic reduction currents (-0.6V to -1.8V) observed on the reverse scan.

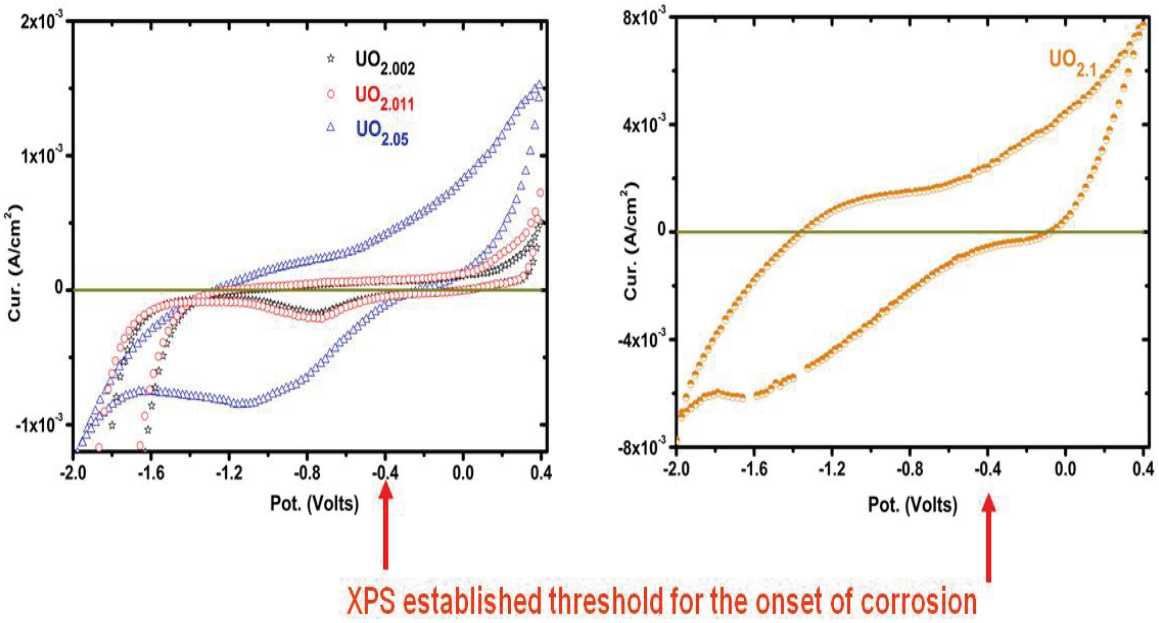


Figure 31: Voltammograms recorded on the four hyper-stoichiometric electrodes (shown in Figure 21) in 0.1 mol/L NaCl (pH 9.5) at a scan rate of 5 mV/s. The threshold is that established for the electrochemical oxidation of 1.5 at% SIMFUEL (Figure 30).

To investigate the oxidation behaviour in more detail the fuel specimens were subjected to more extensive anodic oxidations. This was only possible with the $UO_{2.002}$ and $UO_{2.011}$ electrodes since the voltammetric scans on the $UO_{2.05}$ and $UO_{2.1}$ specimens (Figure 31) suggest longer anodic oxidations would be extensive and potentially destructive. Figure 32 shows the cathodic reduction scans performed after individual 30 minute oxidations at applied potentials in the range -500 mV to +300 mV. The single most positive data point for each of these oxidations shows the anodic (oxidation) currents still sustained on the electrode after 30 minutes. From these points it can be seen that sustainable oxidation is only achieved for potentials ≥ -400mV; i.e., at potentials beyond the oxidation threshold established on the stoichiometric SIMFUEL, Figure 30. However, even for oxidation at a potential below this threshold (-500 mV), a reduction process is observed suggesting some minor areas of the surface are either already oxidized prior to application of a potential (i.e., non-stoichiometric) or sub-thermodynamically oxidized electrochemically when the potential is applied.

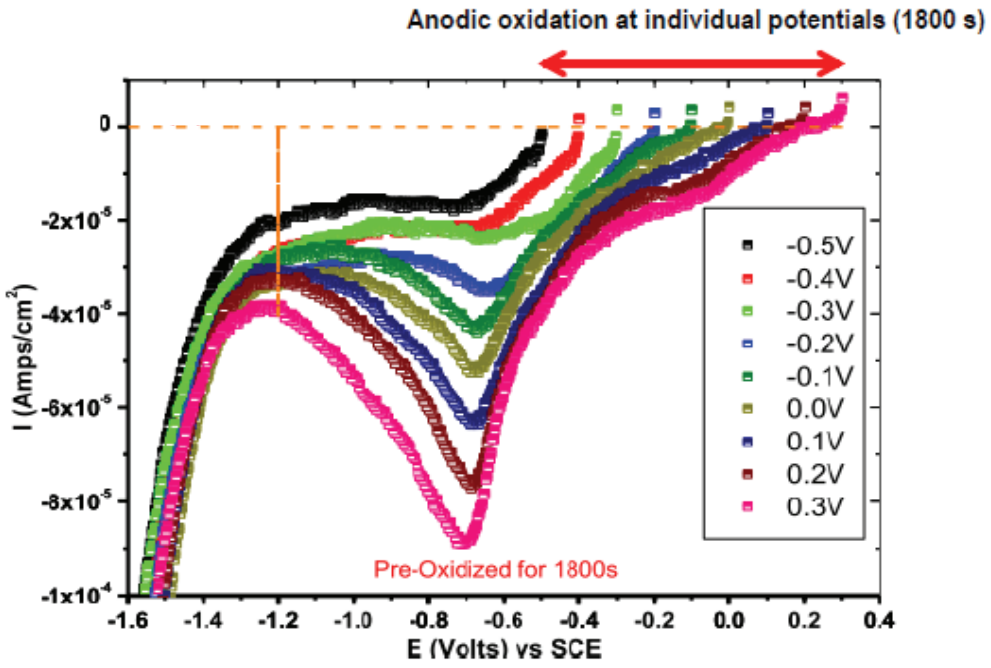


Figure 32: Cathodic reduction scans performed on the $UO_{2.002}$ electrode at a scan rate of 5 mV/s after individual 30 minute anodic oxidations at applied potentials in the range -0.5 V to +0.3 V in 0.1 mol/L NaCl (pH 9.5). The electrode was prepared by polishing and cathodic cleaning between each experiment.

As the potential is made more positive a reduction peak develops at ~ -700 mV with a shoulder at more negative potentials. The position of this peak is the same as observed on SIMFUEL (Figure 29) indicating the cathodic reduction is of the oxide anodically grown on surface areas close to stoichiometric prior to oxidation. The presence of the shallow shoulder on the negative potential side of the reduction peak suggests the presence of a less readily reduced surface consistent with the oxidation of the slightly more non-stoichiometric regions of the surface shown to be present by CSAFM and SEM/EDX, Figures 22 and 21. The very shallow reduction peak formed after oxidation at very positive applied potentials can be attributed to the reduction of dissolved UO_2^{2+} formed in pits and asperities on the UO_2 surface. This process has been discussed in detail elsewhere (Santos et al. 2006), but is not relevant to the present discussion.

Figure 33 shows a similar, but more extensive, series of experiments performed on the $UO_{2.011}$ specimen in which anodic oxidations were performed at potentials from -500 mV to +350 mV for times ranging from 1 minute to 30 minutes at each potential. The reduction profiles of the anodically oxidized surface are considerably more complicated than those recorded on the $UO_{2.002}$ specimen. Up to 5 distinct cathodic reduction peaks are observed, and their prominence depends on the applied potential and the duration of the anodic oxidation. Based on this series of experiments, it is not possible to determine the nature of the individual oxidation processes leading to the cathodic reduction peaks observed. However, accepting the correlation between composition (x in UO_{2+x}) and surface conductivity demonstrated in the conductivity map for this specimen, Figure 23, it is clear that a number of differently oxidized states exist on the electrode surface.

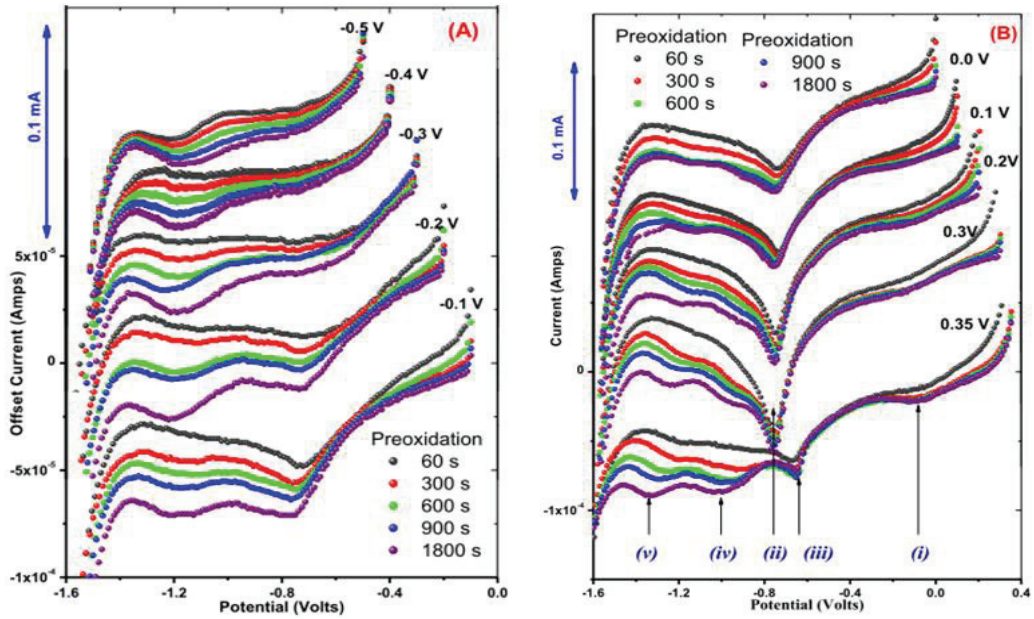


Figure 33: Cathodic reduction scans performed on the $UO_{2.011}$ electrode at a scan rate of 5 mV/s after individual anodic oxidations at potentials from -0.5V to -0.1V (A) and 0.0V to+0.35V (B) in 0.1 mol/L NaCl (pH 9.5) for times ranging from 1 minute to 30 minutes at each potential: (*i*) to (*v*) indicate the locations of individual reduction peaks observed after anodic oxidation at the most positive applied potential.

A number of distinct differences between the oxidation of this specimen and the $UO_{2.002}$ electrode can be noted. Even for an applied potential of -500 mV (i.e., below the thermodynamic and experimental threshold for the oxidation of stoichiometric UO_2) the electrode surface is extensively oxidized, a reduction plateau being observed for E ≤ -600 mV on the cathodic scan, and a broad reduction peak appearing for E ≤ -1000mV. The reduction currents in both these potential regions increase markedly with even a small increase in potential or an increase in time at a specific potential. The cathodic shoulder at ~ -600 mV is present after anodic oxidation of both electrodes, but more prominent on the $UO_{2.011}$ electrode, and attributed to the more facile oxidation of the slightly non-stoichiometric and more conductive surface regions (Figure 23). However, increasing potential and increasing time at a given potential leads to the development of a cathodic reduction process in the range -1000 mV to -1200 mV on $UO_{2.011}$ which did not occur on $UO_{2.002}$. As shown in the conductivity maps for these two electrodes (Figures 22 and 23), only the $UO_{2.011}$ electrode exhibits the ridged surface features associated with domains of defect clusters, suggesting it is these features that are readily and extensively oxidized leading to the cathodic reduction peaks in the -1000 mV to -1200 mV range.

The cathodic peak centred at ~ -750 mV is also common to both electrodes and is the only reduction peak observed after oxidation of a stoichiometric SIMFUEL surface (Figure 29). Consequently, it can be attributed to the reduction of the oxide anodically formed on areas of the surface close to stoichiometric. The apparent shift of this peak to more positive potentials ((ii) → (iii)) and its decrease in relative importance (compared to peaks (iv) and (v)) coincides

with the appearance of peak (i) and can be attributed to the acidification process occurring at the most positive applied potential and noted in Figure 30. This decrease in relative peak heights indicates that the oxide formed at more stoichiometric locations may be more readily dissolved than that on more non-stoichiometric areas.

It is suggested by these experiments that the kinetics of oxidation of the UO_{2+x} surface varies from location to location with the ease and rate of oxidation appearing to increase in the following order: stoichiometric < random interstitial < defect clusters. This sequence would be consistent with AFM results, Figure 27.

5.5 LOCAL CORROSIVITY ON NON-STOICHIOMETRIC UO_{2+x} SURFACES

While the electrochemical studies described above offer evidence that corrosion damage accumulates more readily on non-stoichiometric areas, it cannot unequivocably demonstrate that this is the case. To achieve the lateral resolution required to investigate the corrosion behaviour at specific surface locations, scanning electrochemical microscopy (SECM) experiments were conducted on all four non-stoichiometric electrodes. The principle behind this technique is illustrated in Figure 34. The corrosion kinetics at an individual location can be determined using the probe approach curve (PAC) technique illustrated and described in Figure 34. Based on the probe approach curve measurement, a reaction-diffusion model can be developed from which a rate constant for consumption of the oxidant in the corrosion process can be extracted. Since the rates of oxidant consumption and substrate oxidation are equal in a corrosion reaction, this rate constant is a measure of the UO_{2+x} corrosion rate.

It is also possible to image the reactivity of the surface by scanning the UME probe across the surface at a constant tip height. However, this will lead to a current partially controlled by the topography of the surface which for these UO_{2+x} specimens will vary from location to location, Figure 21, thereby, varying the substrate-UME tip separation and influencing the feedback current.

Although not shown here, PACs recorded on the $UO_{2.002}$ specimen show little variation in reactivity from location to location as expected given the uniform distribution in composition and conductivity. At all locations probed, negative feedback was obtained demonstrating the low reactivity of this close-to-stoichiometric specimen. Figure 35 shows an SECM image and three PACs recorded on the locations numbered on the $UO_{2.011}$ specimen. The image, which provides a mixture of topographical and corrosion information shows well defined regions with different current responses, and the size of these regions is similar to the grain sizes observed by SEM, Figure 21. The current response varies from grain to grain as well as within grains consistent with expectations based on the AFM topography and CS-AFM conductivity maps (Figure 23).

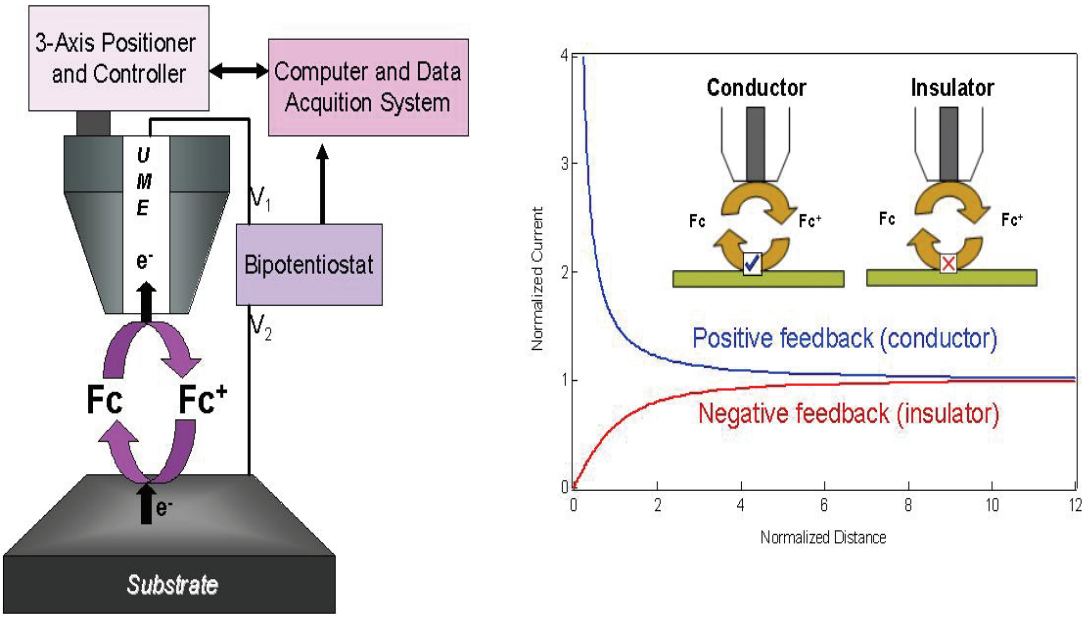


Figure 34: Schematic illustrating the principle behind the technique of scanning electrochemical microscopy (SECM) used to supply in-situ electrochemical information at high spatial resolution (micron scale). A potential is applied to an ultra microelectrode (UME) to create an oxidant which can subsequently corrode the UO_{2+x} substrate.

Ferrocene methanol (Fc) was chosen as the mediator since it can be rapidly converted (at a diffusion controlled rate) to Fc^+ at the UME tip, and its subsequent reduction kinetics to cause corrosion of the UO_{2+x} surface are expected to be similar to those of H_2O_2 (the primary radiolytic oxidant anticipated under waste disposal conditions) because the standard reduction potentials for the two are close (Jonsson et al. 2004).

When the UME is far from the substrate, the current for generation of the oxidant, Fc^+, is determined by hemispherical diffusion of Fc from the bulk of the solution to the electrode surface. When the UME probe approaches a specific location on the substrate, this diffusion controlled current is perturbed in one of two ways. If Fc^+ is not consumed by corrosion of the substrate, then the current decays during the approach since diffusion of the mediator from the bulk of solution to the UME tip is blocked (negative feedback). If Fc^+ is consumed by corrosion of the substrate, then the oxidant is regenerated on the UME tip and the current increases (positive feedback).

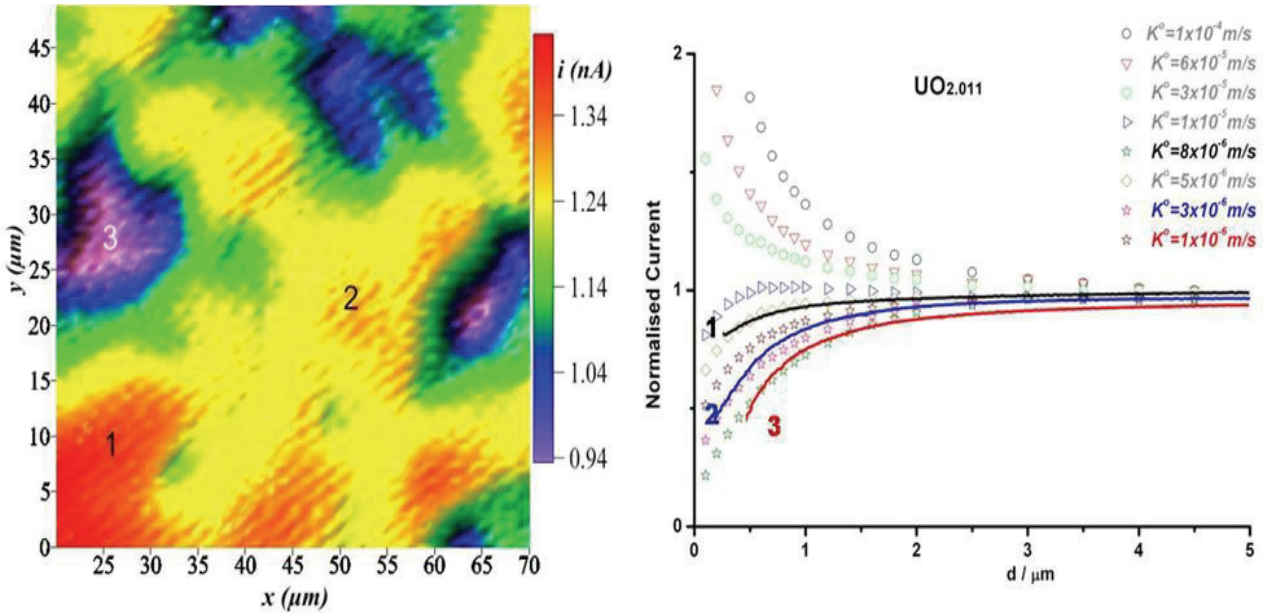


Figure 35: An SECM image (50 μm by 50 μm) and probe approach curves recorded on a $UO_{2.011}$ electrode under corrosion conditions in 0.1 mol/L NaCl (pH 9.5). The current range is indicated in the bar on the right-side of the image. The probe approach curves are superimposed on a series of theoretical curves calculated for various values of the rate constant for the cathodic reaction on the corroding UO_{2+x} substrate surface.

The three probe approach curves are superimposed on a series of theoretical curves calculated for various values of rate constant. The SECM image exhibits only minor differences in current feedback and the PACs performed on high and low current regions of the image both exhibit negative feedback indicating only minor consumption of Fc^+ by the substrate. It can be concluded that Fc^+ causes only slow corrosion of the $UO_{2.011}$ surface but with some areas corroding at up to 5 times the rate of other areas. This variability from location to location is consistent with the differences in electrochemical oxidation of surface locations shown in Figure 33.

For the $UO_{2.05}$ electrode, Figure 36, the SECM image shows a much wider range of currents and the PACs confirm that smooth locations close to stoichiometry exhibit negative feedback (low corrosion rates) while ridged locations with high degrees of non-stoichiometry exhibit positive feedback (high corrosion rates). For the three PACs shown, the range of rate constants for the cathodic reaction is ~200. For the $UO_{2.1}$ specimen the image shows very different currents at distinct locations and the PACs recorded at different locations show the coexistence of locations with low corrosion rates and others with very high rates, Figure 37. For a series of PACs recorded on this specimen the distribution of k values covers a range of $\geq 10^3$.

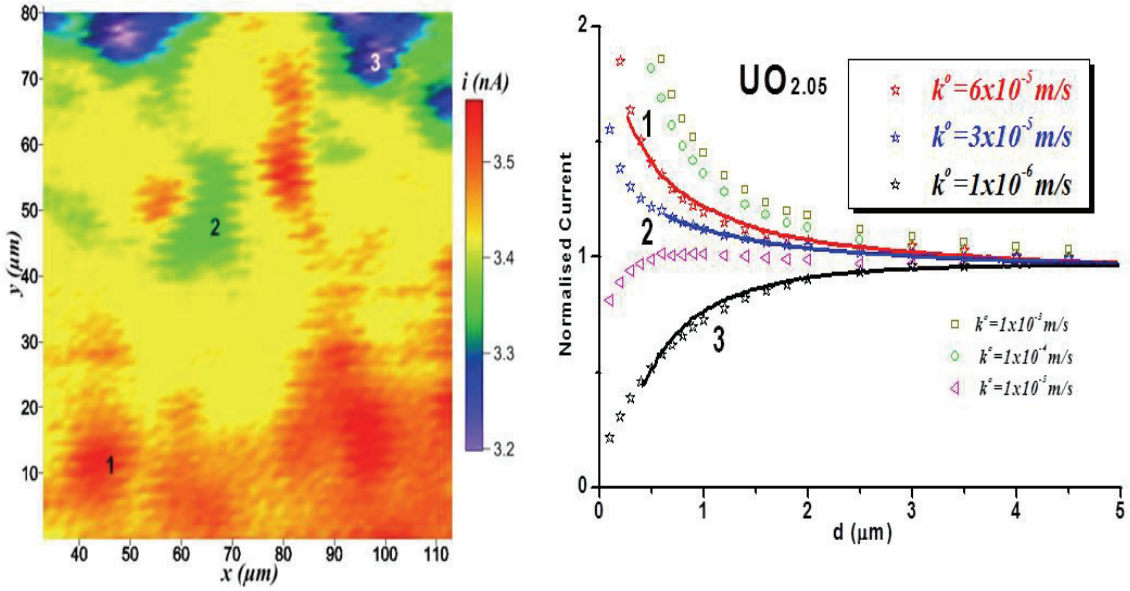


Figure 36: An SECM map (80 μm by 80 μm) and probe approach curves recorded on a $UO_{2.05}$ electrode under corrosion conditions in 0.1 mol/L NaCl (pH 9.5). The current range is indicated on the bar attached to the image. The probe approach curves are superimposed on a series of theoretical curves calculated for various values of the rate constant for the cathodic reaction on the corroding UO_{2+x} substrate surface.

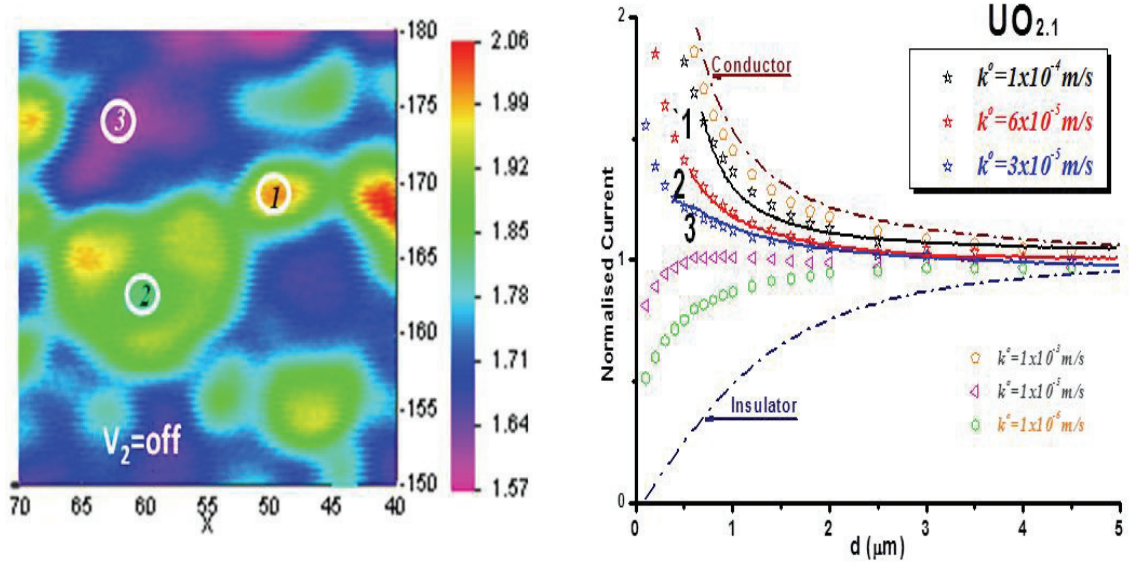


Figure 37: An SECM map (30 μm by 30 μm) and probe approach curves recorded on a $UO_{2.1}$ electrode under corrosion conditions in 0.1 mol/L NaCl (pH 9.5). The current range is indicated in the bar on the image. The probe approach curves are superimposed on a series of theoretical curves calculated for various values of the rate constant for the cathodic reaction on the corroding UO_{2+x} substrate surface.

Figure 38 summarizes the diversity in corrosion kinetics, expressed in terms of the rate constants (determined from PACs) for the cathodic reduction reaction, and the defect structures (determined by Raman mapping), expressed in terms of the intensity of the 445 cm^{-1} band (O-U stretch) observed on the four electrodes. A direct relationship is observed between local corrosion kinetics and the presence of non-stoichiometric defect structures. As the degree of nominal non-stoichiometry increases the diversity of defect structures and corrosion rates on the UO_{2+x} surface increases. This leads to a mixture of stoichiometric locations which sustain an extremely low corrosion rate and a series of structures distorted to various degrees on which the corrosion rate is considerably higher. The highest corrosion rates, which are up to 10^3 times higher than those on stoichiometric locations occur on grains which have undergone a cubic to tetragonal distortion as their composition approaches $UO_{2.33}$. It should be noted that this comparison of corrosion kinetics is only semi-quantitative since chemical conditions under the tip (specifically the local pH) could change as it approaches the surface.

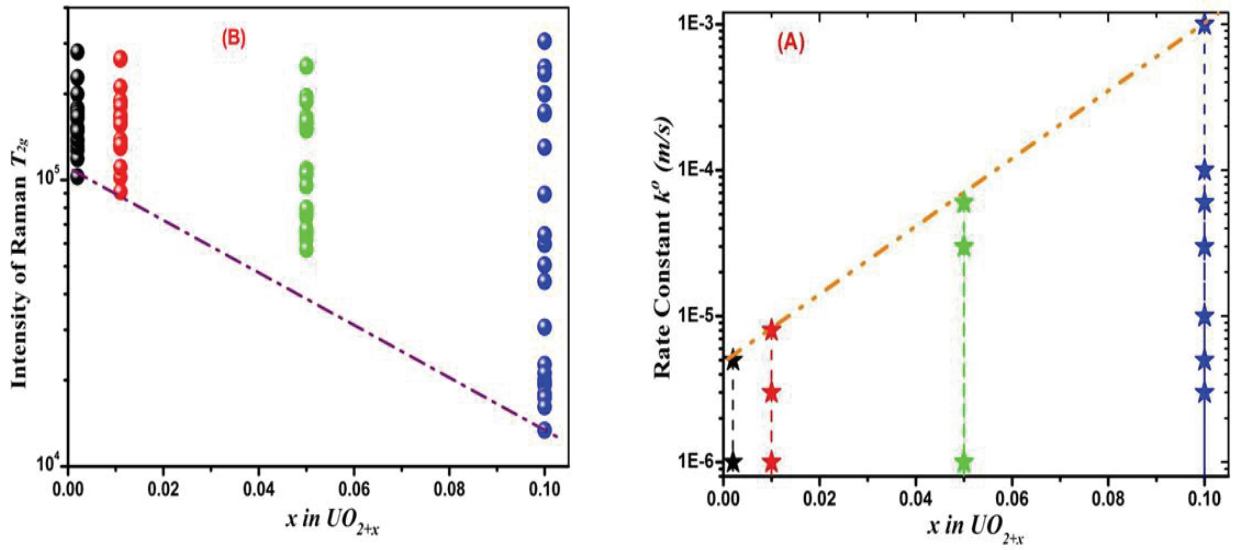


Figure 38: The diversity in corrosion kinetics, expressed in terms of the rate constants (determined from PACs) for the cathodic reduction reaction, and the UO_{2+x} defect structures determined by Raman mapping (expressed in terms of the intensity of band 1 (445 cm^{-1})) for the four electrodes varying in nominal composition from $UO_{2.002}$ to $UO_{2.1}$ (Figure 21).

These studies clearly demonstrate that the anodic reactivity of UO_2 increases substantially with degree of non-stoichiometry. Since non-stoichiometry also catalyzes cathodic reactions, as illustrated in Figure 7A, such locations would be capable of preferentially supporting both the anodic and cathodic reactions which couple during fuel corrosion. In spent nuclear fuel, therefore, the grain boundaries, where non-stoichiometry might be expected due to incomplete sintering during fabrication or generated by in-reactor irradiation, could corrode more rapidly than stoichiometric grains. Consequently, the presently adopted assumption (in waste disposal performance assessment calculations) that radionuclides residing in grain boundaries will be instantly released on contact with groundwater should be retained.

6. DEVELOPMENT OF LOCAL ACIDITY AT THE CORRODING FUEL SURFACE

6.1 THE INFLUENCE OF CORROSION PRODUCT DEPOSITS ON FUEL CORROSION

The possibility of forming acidic conditions within surface flaws or cracks in the fuel and/or pores in corrosion product deposits was originally identified in corrosion experiments with used fuel (Shoesmith et al. 1996) and subsequently observed in experiments at high alpha dose rates (Wren et al. 2005) and in electrochemical experiments (Santos et al. 2004, 2006c). Under general corrosion conditions anodes and cathodes would not be expected to be separated and the alkalinity produced by the reduction of radiolytically-produced peroxide ($H_2O_2 + 2e^- \rightarrow 2OH^-$) should, at least partially neutralize the acidity produced by the anodic reaction as illustrated in Figure 39.

A model was developed to determine whether, even if anodes and cathodes were separated, as illustrated in Figure 39, a significant change in pH could be generated at the fuel dissolution rates sustainable within a failed container (Cheong et al. 2007). It was concluded that only a marginal effect on fuel corrosion would be expected.

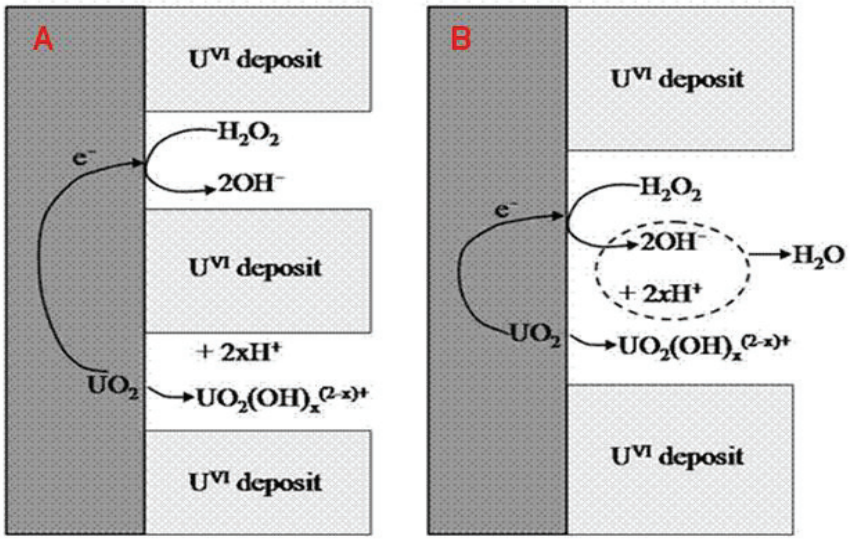


Figure 39: Illustrations showing how acidity can develop within pores in a corrosion product deposit. The first panel shows that acidity can develop at the anodic dissolution site providing it is separated spatially from the cathodic site. The second panel shows that, if the two sites are not separated, then the alkalinity produced by H_2O_2 reduction will, at least partially, neutralize the acidity.

To experimentally verify this prediction a series of experiments were undertaken in which the corrosion rate was controlled by applying low electrochemical currents to simulate, as closely as experimentally feasible, the rates anticipated under repository conditions. Experiments were conducted on 1.5 at% SIMFUEL in a solution (pH = 9.5) containing 0.1 mol.L^{-1} NaCl and 0.1 mol.L^{-1} Na_2SiO_3. A high silicate concentration was used to accelerate the formation of a U^{VI} silicate corrosion product deposit on the fuel surface. This should restrict the diffusion of

dissolved UO_2^{2+} away from the fuel surface allowing the possibility of acidification within the deposit by its hydrolysis, Figure 39A. By applying this current electrochemically the separation of anodes and cathodes is artificially achieved since the cathodic reaction is transferred to a counter electrode in the electrochemical cell.

Figure 40 shows the potential-time profile obtained over many hours in an experiment in which the applied current (simulating the corrosion rate) was increased in stages. Figure 41 shows the final potentials achieved at each current in the sequence immediately before the current was increased to the next higher value. The dashed line at 275 mV (vs. SCE) is the approximate potential at which the development of local acidity was clearly observed at higher applied currents (Ofori et al. 2010). In the experiment considered here, this threshold was only exceeded for applied currents > 8 $nA.cm^{-2}$. The presence of a corrosion product at the end of this experiment was demonstrated by SEM, Figure 42. The deposit was extremely fine grained and widespread and would hence be expected to protect the underlying UO_2 from corrosion except within the network of fractures and pores. The presence of a band in the Raman spectrum around 800 cm^{-1} (6), Figure 43, shows that the deposit is a uranyl-containing phase, while the simultaneous observation of the UO_2 bands (1, 3, 4) indicates the deposit is thin. EDX analyses confirm the presence of silicate in the deposit though the Raman spectrum did not provide unequivocal evidence demonstrating the formation of uranyl silicate.

Removal of the deposit by sonification and rinsing showed that the entire UO_2 surface was generally attacked/etched suggesting that the areas under the deposit have been subjected to some degree of acidification. This is not surprising since the 275 mV threshold beyond which acidification is known to occur was eventually exceeded at the highest applied currents, Figure 40.

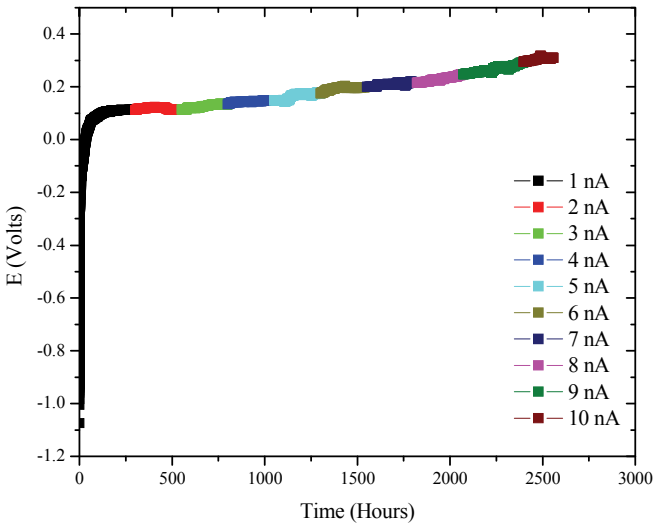


Figure 40: Potential-time profile recorded on a 1.5 at% SIMFUEL electrode in 0.1 mol/L NaCl (pH 9.5) in which the applied current (simulating the corrosion rate) was increased in stages from 1nA to 10nA. The area of the exposed electrode surface was ~1cm^2.

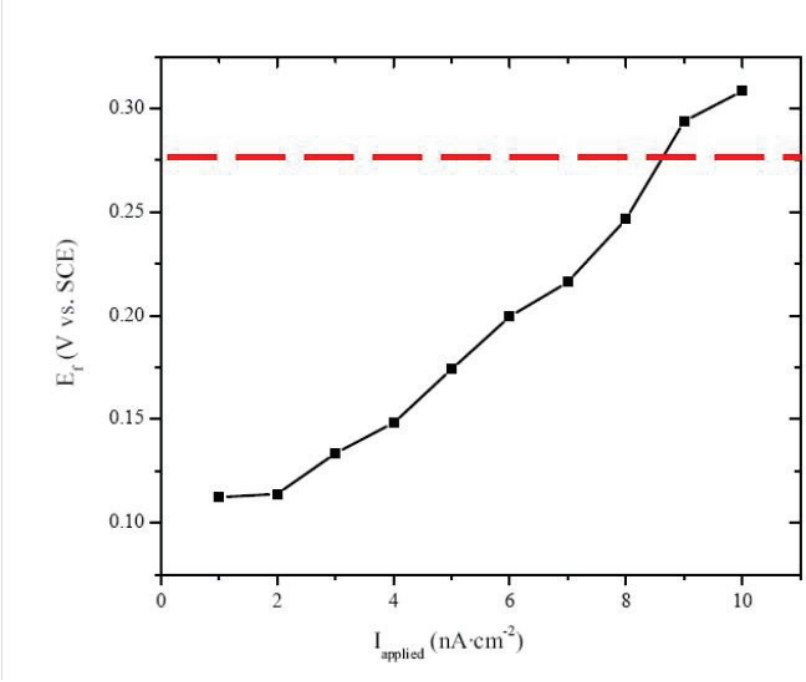


Figure 41: The final potentials achieved on a 1.5 at% SIMFUEL electrode at each current applied in the experiment shown in Figure 40. The dashed line at 275 mV (vs. SCE) is the approximate potential at which the development of local acidity can be clearly observed (Ofori et al. 2010).

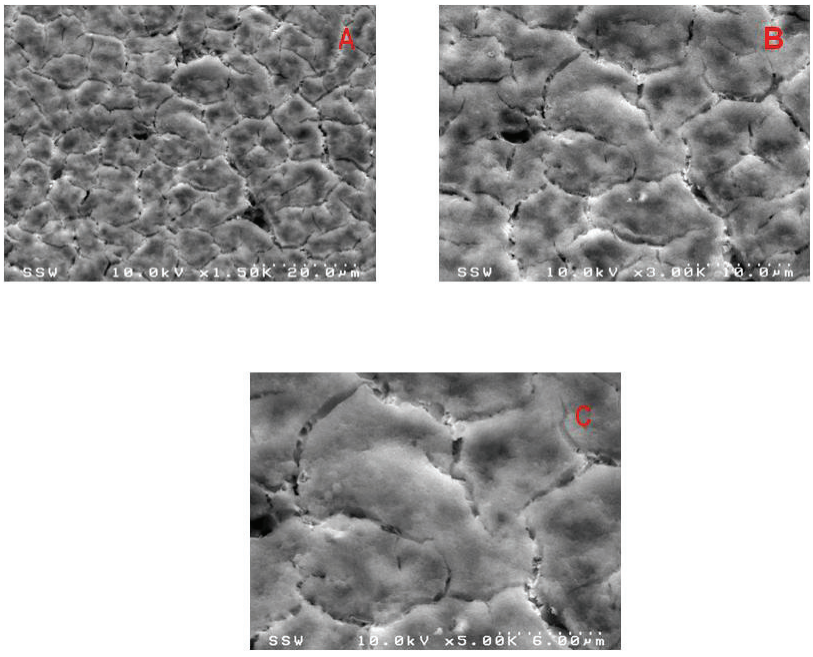


Figure 42: SEM images of a 1.5 at% SIMFUEL surface after application of a sequence of applied currents (Figure 40) in 0.1 mol/L NaCl (pH 9.5) for magnifications of (A) 1500; (B) 3000; (C) 5000 X.

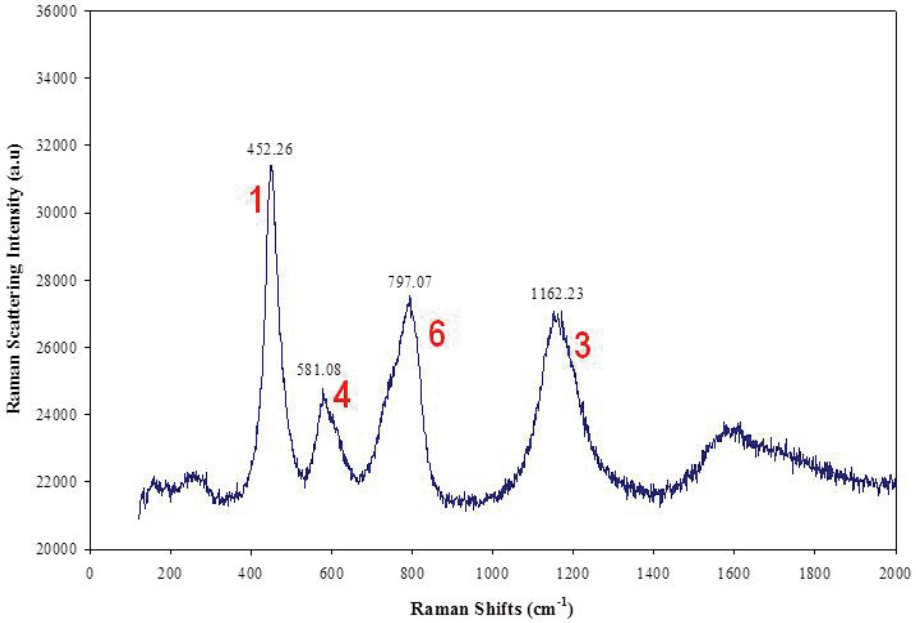


Figure 43: Raman spectrum recorded on a 1.5 at% SIMFUEL electrode after application of a sequence of applied currents from 1nA to 10nA (Figure 40). The bands are numbered as defined in Figure 8.

At very low applied currents (≤ 2nA.cm^{-2}), the potential approached a plateau suggesting it was independent of time and the value of ~ 110 mV (vs. SCE) is in the range measured for the corrosion potential of UO_2 in aerated (Sunder et al. 1991, 2004; Wren et al. 2005; Shoesmith et al. 1994; Goldik et al. 2004), peroxide-containing (10^{-4} to 10^{-2} mol.L^{-1}) and alpha radiolytically-decomposed solutions (Wren et al. 2005). The electrochemically–predicted current values at these potentials (Shoesmith 2000) are in the range 0.1 to 1nA.cm^{-2} showing that this experiment simulated fuel behaviour under oxidizing conditions. A more detailed model for corrosion due to α-radiolysis (Shoesmith et al. 2003) predicts an evolution in E_{CORR} from -50 mV to -180 mV over a 30,000 year period. These values are considerably lower than those measured (E_{CORR}) or achieved by the application of low currents in this study, where acidification did not occur at the lowest current densities applied. These results are consistent with the model calculations (Cheong et al. 2007) and confirm that the development of locally acidic conditions within the fuel due to corrosion is extremely unlikely.

6.2 THE ANODIC DISSOLUTION OF UO_2 IN ACIDIC SOLUTIONS

While the possibility of local acidification at locations on the fuel surface is unlikely (Section 6.1) the chemistry/electrochemistry of UO_2 was studied at pH values down to 1 to clarify how the mechanism of the anodic (dissolution as UO_2^{2+}) and cathodic (H_2O_2 reduction) reactions changed with pH. The anodic reaction was studied in 1.5 at% SIMFUEL in chloride and sulphate solutions since these are the two ions expected to dominate in natural groundwaters, and the cathodic reaction was studied over the pH range 9 to 1 in chloride solutions. The specific anion present, with the exception of carbonate/bicarbonate at the high end of this pH range, is not expected to influence H_2O_2 reduction.

Figures 44A and 44B show the anodic dissolution currents (plotted logarithmically) as a function of applied potential for three pH values in 0.1 mol/L NaCl and 0.1 mol/L Na_2SO_4 solutions, respectively. Such plots are known in the electrochemical literature as Tafel plots and can be used to determine the reaction mechanism and rate-determining step. The identifiable linear regions of the plots are indicated by the numbered lines. Lines 1, 2 and 3 indicate Tafel slopes of 40 mV/decade, 60 mV/decade and 120 mV/decade of current increase, respectively.

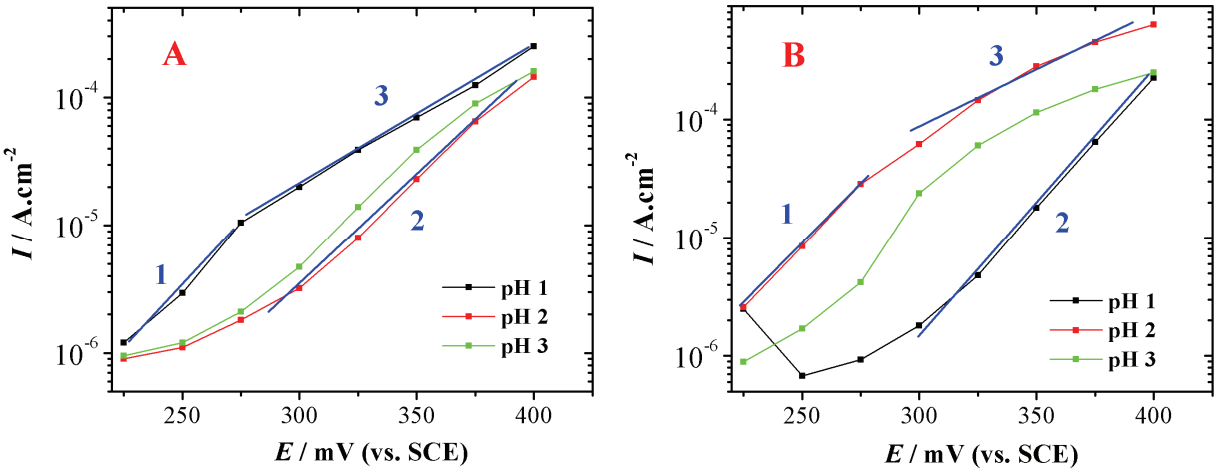


Figure 44: Anodic dissolution currents recorded on a 1.5 at% SIMUFUEL rotating disk electrode (16.7 Hz) in 0.1 mol/L^{-1} NaCl (A) and 0.1 mol.L^{-}1 Na_2SO_4 (B) solutions with various pH values: pH = 1 (black); pH = 2 (red); pH = 3 (green). The numbered lines are theoretical slopes of 40 mV/decade (1), 60 mV/decade (2), and 120 mV/decade (3).

Based on an original suggestion by Nicol and Needes (1975) and subsequently supported by our previous studies (Santos et. al. 2006), it has been claimed that the steady-state dissolution of UO_2 in acidic solutions proceeds via a mechanism involving U^{V} and U^{VI} surface intermediates,

$$UO_2 + H_2O \leftrightarrow (U^{V}O_2OH)_{ads} + H^+ + e^- \quad (2)$$

$$(U^{V}O_2OH)_{ads} + H_2O \rightarrow (U^{VI}O_2(OH)_2)_{ads} + H^+ + e^- \quad (3)$$

$$(U^{VI}O_2(OH)_2)_{ads} + 2H^+ \rightarrow UO_2^{2+} + 2H_2O \quad (4)$$

with the anions present in the solution being deemed not to be involved in the fuel anodic dissolution process.

However, Figures 44A and 44B show that the observed behaviour is different in chloride compared to sulphate solutions. To emphasize these differences, the currents recorded at a potential of 325 mV in the two solutions are compared in Figure 45. In the chloride solution the current increases as pH decreases although the difference is only approximately a factor of 4.

By contrast, in sulphate solutions, the currents were highest at pH 2 and pH 3 and decreased by an order of magnitude when the pH was lowered to 1. A most likely possible explanation for these differences is that SO_4^{2-} actively accelerates the overall dissolution process at pH $\geq$ 2 but the reaction is inhibited by HSO_4^- at pH 1, the pK_a for the protonation reaction

$$HSO_4^- \leftrightarrow SO_4^{2-} + H^+ \qquad (5)$$

being 1.7.

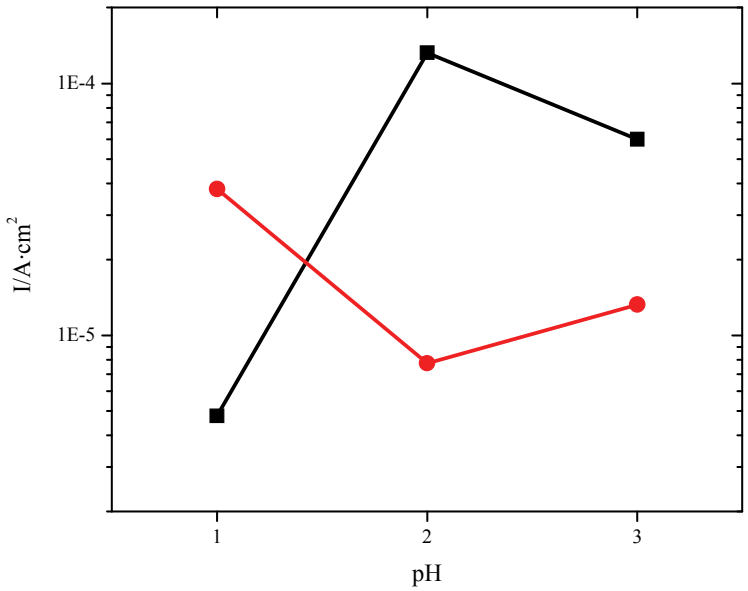


Figure 45: Steady-state anodic dissolution currents recorded on a 1.5 at% SIMFUEL electrode at a potential of 325 mV, as a function of pH in 0.1 mol/L^{-1} NaCl (red) and 0.1 mol/L^{-1} Na_2SO_4 (black)

Based on the standard procedures for analyzing linear log current (I) vs. potential relationships the plots in Figures 44A and 44B can be interpreted as follows:

(i) When the plot exhibits a single slope of 60 mV^{-1} (i.e., the current changes by one order of magnitude for an increase in potential of 60 mV; Line 2 for pH 2 and 3 in Cl^-, and pH 1 in SO_4^{2-}), the second electron transfer reaction (reaction 3) is the rate-determining step.

(ii) When the plot exhibits two distinct slopes of 40 mV^{-1} at low applied potentials (Line 1) and a slope of 120 mV^{-1} (Line 3) at high applied potentials (pH 1 in chloride solution and pH 2 and 3 in sulphate solution) it implies the mechanism changes with applied potential. At low potentials (Line 1) both the forward electrochemical reactions, (2) and

(3), are slow compared to the reverse of reaction (2); and at high potentials both forward reactions are accelerated, the rate of the reverse reaction (2) becomes negligible, and the overall rate is controlled by reaction (2). It is also worth noting in Figure 44B that for sulphate solutions, the current is becoming independent of potential at very high applied potentials as the rate of chemical reaction (4) begins to control the overall rate.

The role of the anions in this overall reaction sequence can be observed by electrochemical impedance spectroscopy and a detailed study has been published (Ofori 2008). Based on these analyses it can be shown that, in potential regions where the slope is 40 mV^{-1} (Line 1, Figures 44A and B) and the reverse of reaction (2) is rapid, the coverage by U^{V}_{ads} and U^{VI}_{ads} intermediates is low; i.e., the anions exhibit little influence in stabilizing the adsorbed species involved in the overall dissolution process. When the log I-E slope increases to 120mV^{-1} at higher applied potentials the adsorbed intermediates accelerate the dissolution process, consistent with overall control of the rate by their formation in reaction 2. At pH $\geq$ 2, this analysis confirms that SO_4^{2-} accelerates the overall dissolution process compared to Cl^-. When the Log I-E slope is 60 mV^{-1}, a condition observed when the overall currents are relatively low and the rate of the overall reaction is controlled by reaction (3), the electrochemical impedance spectroscopy analyses confirm that the intermediate U^V adsorbed species is strongly stabilized on the electrode surface by the coadsorption of HSO_4^-.

6.3 THE INFLUENCE OF pH ON THE MECHANISM OF H_2O_2 REDUCTION

Studies of the cathodic reduction of H_2O_2 on 1.5 at% SIMFUEL show that the mechanism and kinetics of the reaction are unchanged over the pH range ~4 to 9, Figure 46. Extensive studies have shown that this reaction proceeds via a coupled chemical-electrochemical process in which U^{IV} – U^V donor-acceptor sites are first chemically created on the UO_2 surface by H_2O_2 and subsequently destroyed electrochemically (Goldik et al. 2004, 2005, 2006; Shoesmith et al. 2005; Shoesmith 2007),

$$2U^{IV} + H_2O_2 \rightarrow 2U^{V} + 2OH^- \quad (6)$$

$$2U^{V} + 2e^- \rightarrow 2U^{IV} \quad (7)$$

Under natural corrosion conditions, as opposed to the electrochemical conditions used to generate the curves in Figure 46, these reactions would be coupled with the oxidation and dissolution of the fuel ($UO_2 \rightarrow UO_2^{2+} + 2e^-$).

The oxidation reaction involves the insertion of O^{2-} anions at interstitial sites in the UO_2 fluorite lattice to produce a $U^{IV}_{1-2x}U^{V}_{2x}O_{2+2x}$ surface layer. This layer is stable in non-acidic solutions and can sustain H_2O_2 reduction at the diffusion-controlled limit at sufficiently negative applied potentials, as illustrated in Figure 46.

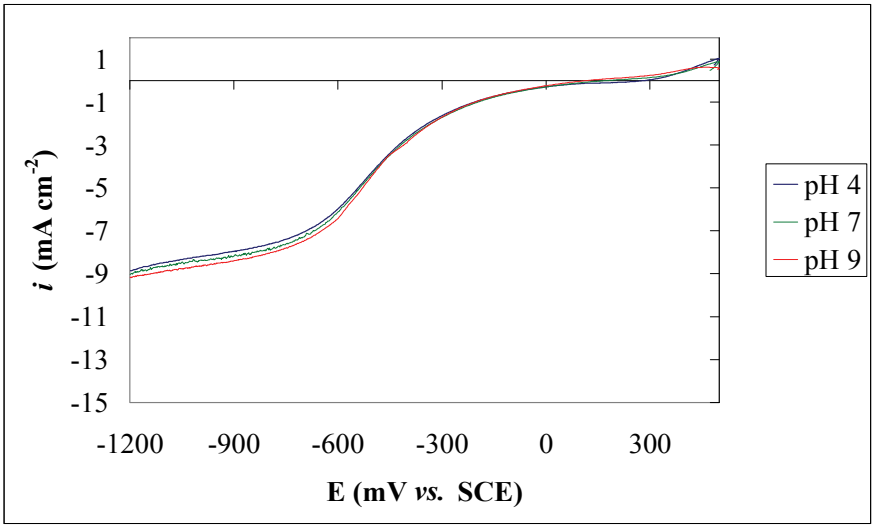


Figure 46: H_2O_2 reduction currents recorded on a 1.5 at% SIMFUEL electrode from negative to positive potentials at a potential scan rate of 10 mV.s^{-1} and an electrode rotation rate of 16.7 Hz in 0.1 mol/L^{-1} NaCl/0.05 mol/L^{-1} borate containing 8 x 10^{-3} mol/L^{-1} H_2O_2 with pH values of 4, 7 and 9.

However, for more acidic pH values, the cathodic reduction process starts to change significantly. Figure 47 shows the H_2O_2 reduction currents recorded at pH 3 and pH 2. At pH 3, two stages of H_2O_2 reduction are observed; a low current in the potential range 300 mV to -300 mV, which is not observed at higher pH; and a current approaching the diffusion controlled limit at more negative potentials as observed at higher pH. At pH 2 the current is larger than at pH 3 in the 300 mV to -300 mV potential range but this current is maintained at more negative potentials and does not increase to the diffusion controlled limit. The currents plotted in Figure 48 show the current in the potential region -100 mV to < -600 mV to be dependent on [H_2O_2] confirming that its cathodic reduction is occurring in a first order reaction. A more extensive study of this process has been published (Keech et al. 2008).

This switch in cathodic reduction behaviour can be attributed to a change in the chemical composition of the surface as previously determined by XPS (Santos et al. 2006). As discussed above, for sufficiently high pH values, H_2O_2 reduction occurs on a $U^{IV}_{1-2x}U^{V}_{2x}O_{2+2x}$ surface layer and the current rises to the diffusion-controlled limit at sufficiently negative potentials. However, for pH <5 this layer is unstable and H_2O_2 reduction occurs on a $(U^{V}O_2OH)_{ads}$ surface adsorbed state. As discussed above, when discussing anodic dissolution this U^{V} adsorbed state is unstable with respect to further oxidation (reaction 2) but also unstable with respect to electrochemical reduction,

$$(U^{V}O_2OH)_{ads} + e^- \rightarrow U^{IV}O_2 + OH^- \qquad (8)$$

The surprising observation that the $U^{IV}_{1-2x}U^{V}_{2x}O_{2+2x}$ layer can be stabilized at pH 3, Figure 47, when it has been shown electrochemically to be unstable below pH ~5 (Santos et al. 2006; Keech et al. 2008) can be attributed to the increase in surface pH due to the production of OH^-

by H_2O_2 reduction, reaction 6. Some XPS evidence exists to support these claims (Keech et al. 2008) but a complete resolution of the reaction mechanism is presently unavailable.

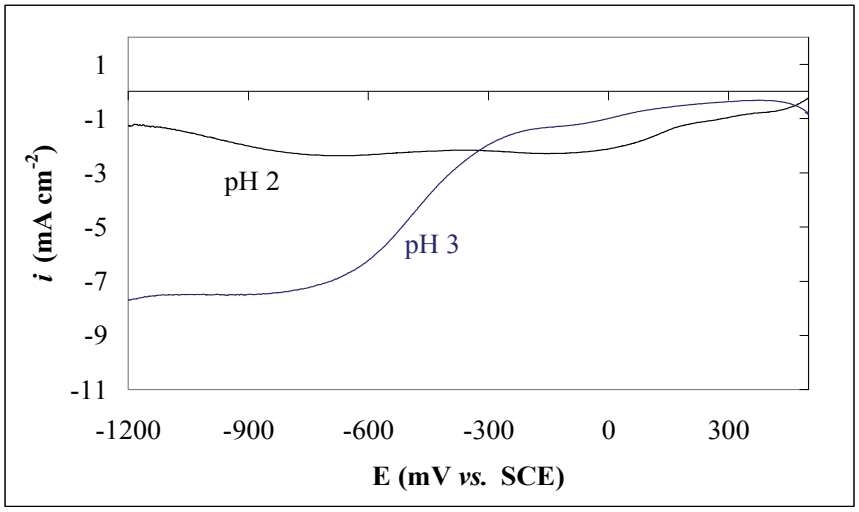


Figure 47: H_2O_2 reduction currents recorded on a 1.5 at% SIMFUEL electrode from negative to positive potential at a scan rate of 10 mV.s^{-1} and an electrode rotation rate of 16.7 Hz in 0.1 mol.L^{-1} NaCl + 0.05 borate containing 9 x 10^{-3} mol.L^{-1} H_2O_2.

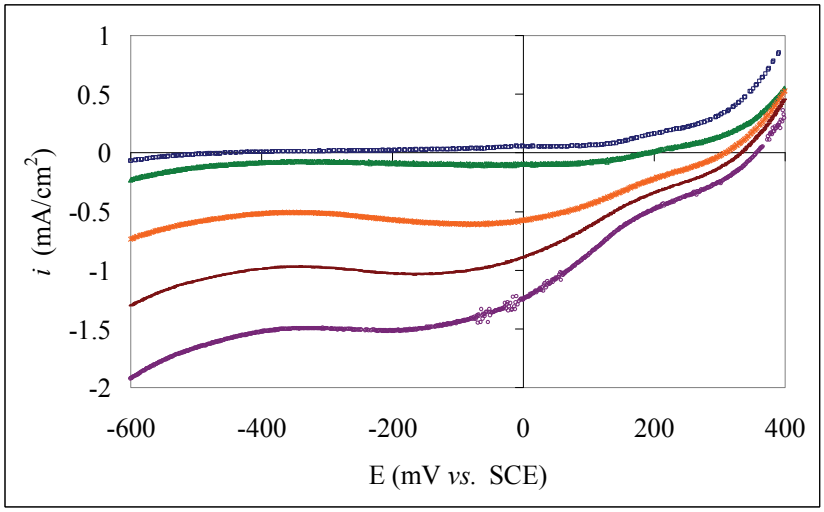


Figure 48: H_2O_2 reduction currents recorded on a 1.5 at% SIMFUEL electrode from negative to positive potentials at a potential scan rate of 10 mV.s^{-1} and an electrode rotation rate of 16.7 Hz. From the top to the bottom scan, (H_2O_2) = 0, 5.2, 21, 36 and 52 x 10^{-3} mol.L^{-1}.

7. THE INFLUENCE OF H_2 ON FUEL CORROSION

The literature on nuclear fuel corrosion/dissolution and radionuclide studies in aqueous solutions containing dissolved hydrogen has been reviewed (Carbol et al. 2005; Shoesmith 2008). In all these studies dissolved H_2 was shown to suppress fuel corrosion and in spent fuel studies to suppress radionuclide release (Carbol et al. 2005, 2009a, b; Cui et al. 2008; Fors et al. 2009; Trummer et al. 2008, 2009; Broczkowski et al. 2010). A number of mechanisms were either demonstrated or proposed to explain these effects, all of which involve the activation of H_2 to produce the strongly reducing H• radical, which scavenges radiolytic oxidants and suppresses fuel oxidation and dissolution (i.e., corrosion). While the exact mechanisms involved may still not be fully understood there is clear evidence that both gamma and alpha radiation produces $H^{\bullet}$ species.

As discussed in Section 2, in-reactor irradiation produces elements which are unstable as oxides (Ru, Pd, Rh, Tc, Mo (partially) and which segregate to form noble metal particles known as ε-particles. Noble metals are well known as catalysts for oxidation/reduction reactions, especially the $H_2|H^{\bullet}|H^+$ reaction, and three of the four predominant components of ε-particles (Rh, Pd, Ru) are exceptionally good catalysts for this reaction as evidenced by their exchange current densities, Table 2 (Broczkowski 2008; Norskov et al. 2008).

Table 2: Exchange current densities for proton reduction for the four predominant epsilon particle constituents

Element	Exchange Current Density ($A.cm^{-2}$)
Pd	$10^{-3.0}$
Rh	$10^{-3.6}$
Ru	$10^{-3.3}$
Mo	$10^{-7.1}$

Thus, it would be expected that these particles would act as galvanically-coupled anodes (for H_2 oxidation) and cathodes (e.g., for H_2O_2 reduction).

7.1 THE INFLUENCE OF NOBLE METAL PARTICLES ON FUEL CORROSION

The E_{CORR} on SIMFUELs is very responsive to variations in redox conditions, Figure 49. In the presence of dissolved O_2 (aerated solutions) oxidation of the fuel surface is catalyzed by O_2 reduction on the ε-particles. A similar catalysis of H_2O_2 reduction occurring on Pd particles dispersed throughout UO_2 was also demonstrated to cause enhanced corrosion (Shoesmith 2008; Nilsson 2008). However, the presence of even small amounts of dissolved H_2 (purging with 5% H_2 / 95% Ar) suppressed E_{CORR} to well below the value measured under purely anoxic conditions (Ar-purging) even for a low density of ε-particles. These results suggest that the presence of distributed ε-particles in a rare-earth doped, conductive UO_2 matrix can both accelerate corrosion in the presence of oxidants as illustrated for H_2O_2 in Figure 50A, or suppress it in the presence of H_2, as illustrated in Figure 50B.

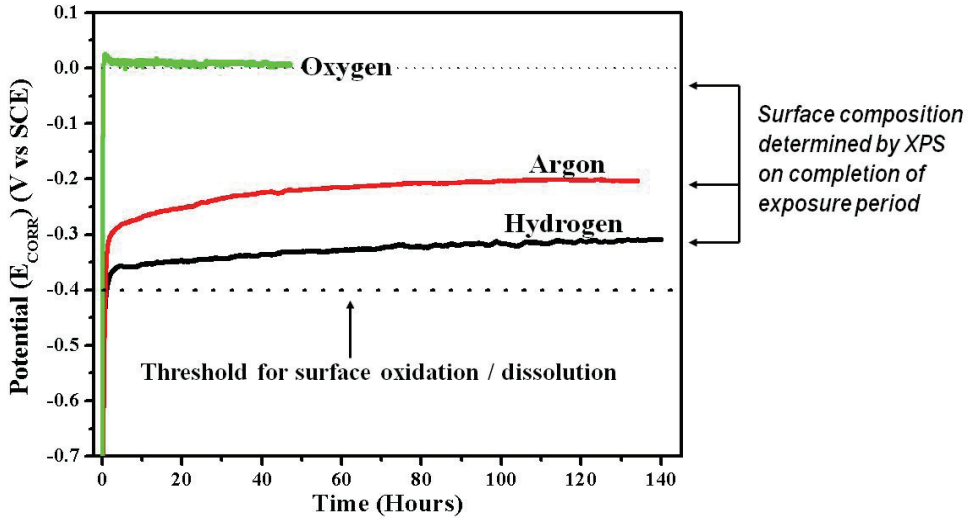


Figure 49: Corrosion potential (E_{CORR}) measured on a 1.5 at% SIMFUEL electrode in 0.1 mol/L KCl (pH 9.5) purged with either O_2, Ar, or 5% H_2/95% Ar at 60ºC. The electrode was freshly polished and cathodically cleaned before each experiment. The potential threshold for surface oxidation and dissolution was established by XPS (Figure 30).

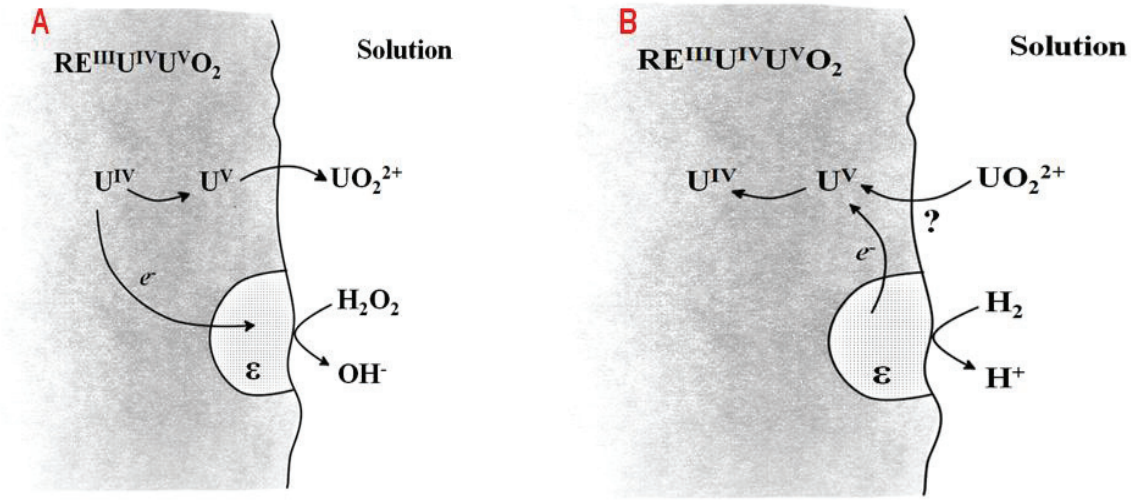


Figure 50: Schematic illustrations showing how noble metal (ε) particles dispersed throughout a conducting, rare each-doped UO_2 matrix could catalyst, (A) oxidant reduction reactions leading to the acceleration of corrosion, and (B) reductant oxidation reactions leading to the suppression of corrosion. The question mark in (B) indicates that there is no substantial evidence that H_2 oxidation can reverse the corrosion reaction by driving the redeposition of dissolved UO_2^{2+}.

Figure 51 shows that the value of E_{CORR} decreased with the number density of ε-particles. As indicated in Figure 49, E_{CORR} measurements were followed by XPS measurements to determine the surface composition of the electrodes, Figure 52(A to C). Also shown for comparison is a set of data recorded on the SSI specimen (Table 1) which is rare earth-doped but contains no ε-particles, Figure 52D. These analyses are superimposed on a plot showing how the surface composition of a 1.5 at% SIMFUEL changes as a function of applied electrochemical potential. This calibration plot was determined in the identical manner to that shown in Figure 30, but at 60°C rather than room temperature (Broczkowski et al. 2007). Here, it serves as a compositional template and its good agreement with the surface compositions of corroded surfaces confirms that the changes observed as the SIMFUEL and purge gas are changed are meaningful and that E_{CORR} and the surface composition are clearly related. As expected from the E_{CORR} measurements, the composition varies little between the different SIMFUELs when exposed to Ar- or O_2-purged solutions. Surfaces exposed to Ar-purged solutions are only slightly oxidized while those exposed to O_2 are predominantly composed of the oxidized U^{V}/U^{VI} states.

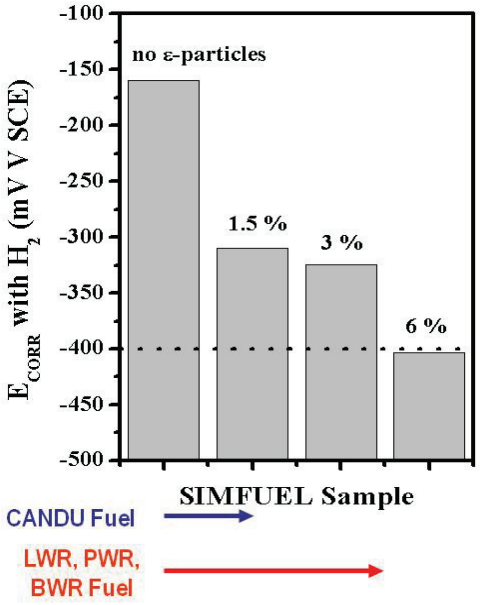


Figure 51:The influence of the increasing number and size of noble metal (ε) particles in SIMFUELs with different degrees of simulated burn-up on the corrosion potential (E_{CORR}) measured in H_2/Ar-purged 0.1 mol/L KCl (pH 9.5) at 60ºC. The dashed line indicates the potential threshold for surface oxidation and dissolution established by XPS (Broczkowski et al. 2007). The arrows indicated the approximate maximum burn-ups expected for different types of fuel.

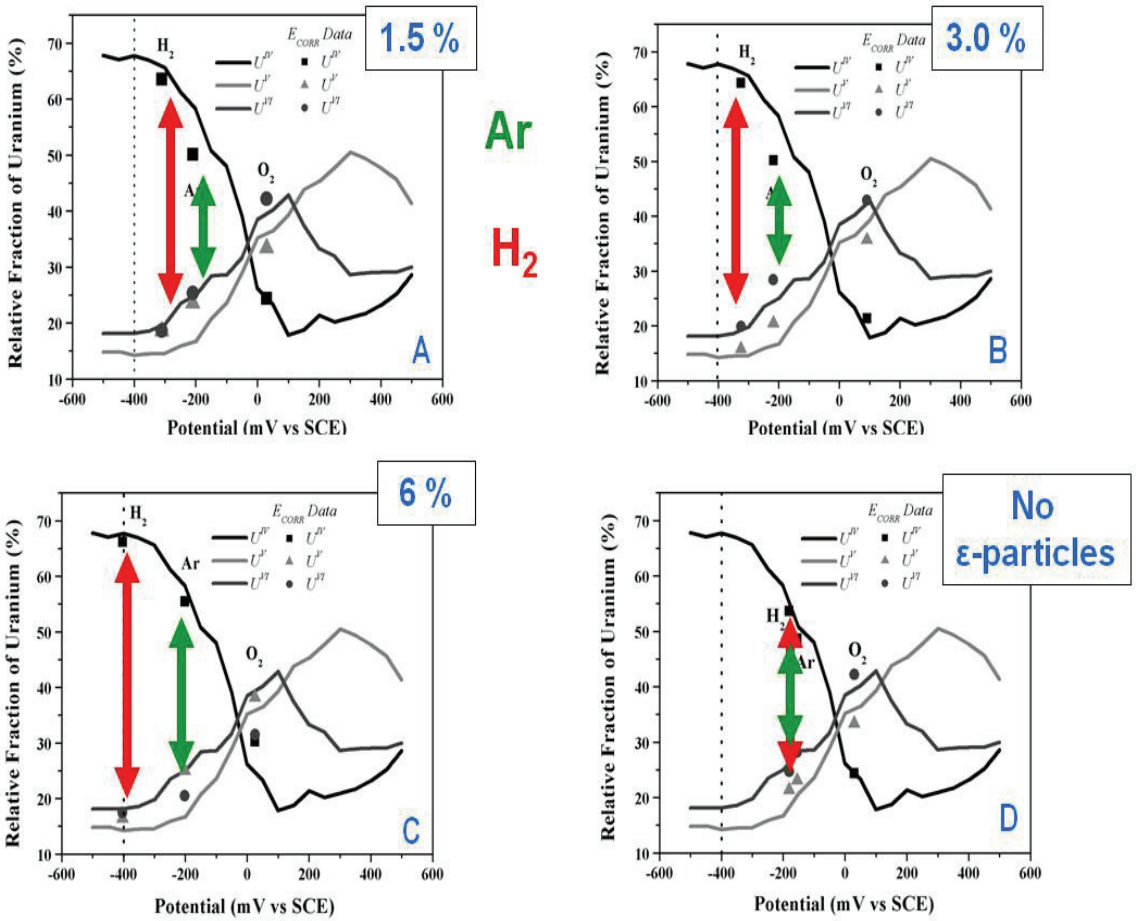


Figure 52: Relative surface fractions of U^{IV}, U^{V} and U^{VI} obtained by XPS as a function of the E_{CORR} achieved in 0.1 mol/L KCl (pH 9.5) purged with either O_2, Ar, or H_2/Ar gas for SIMFUEL specimens with different degrees of simulated burn-up. For comparison, a set of data recorded on a SIMFUEL specimen not containing noble metal (ε) particles is shown. The values are superimposed on a plot showing the surface composition of a 1.5 at% SIMFUEL electrochemically oxidized at individual applied potentials (Broczkowski et al. 2007).

For the SSI specimen containing no ε-particles there is effectively no difference in E_{CORR} and the surface composition in Ar-purged and 5% H_2 / 95% Ar-purged solutions. For the three SIMFUEL electrodes (SF1, SF2, SF3) both E_{CORR} and the extent of surface oxidation decrease as the number density and size of the ε-particles increases. For the 6 at% SIMFUEL (SF3) with the highest number density of ε-particles, E_{CORR} was suppressed to a value of -400mV (vs. SCE), the thermodynamic threshold below which UO_2 corrosion does not occur; i.e., the UO_2 is galvanically protected. That this state is achieved is confirmed by the XPS analyses which show that the surface composition is as reduced as that achieved by electrochemical reduction of the specimen at potentials < -1000mV (vs. SCE).

Figure 51 shows that the E_{CORR} for 1.5 at% SIMFUEL, which simulates the burn-up expected for CANDU fuel, is not suppressed to the threshold value suggesting the fuel would not be fully galvanically protected at this H_2 pressure (concentration). However, even moderate increases in H_2 pressure (or, equivalently, dissolved H_2 concentration) suppress E_{CORR} to values well below the threshold. Eventually, the $H_2|H\bullet|H^+$ reaction becomes reversible on the ε-particles and the UO_2 matrix is rendered completely inert (Broczkowski et al. 2005).

Since noble metals are catalytic for both the reduction of H_2O_2 and the oxidation of H_2, it is not surprising that it can be shown that ε-particles will catalyze the reaction between H_2O_2 and H_2 to produce H_2O; i.e., ε-particles will catalyze the scavenging of radiolytic oxidants by H_2. Nilsson et al. (2007) showed that Pd, present as a powder acted as a catalyst for this reaction, which was shown to be diffusion–controlled on Pd. This would account for the very strong effect of H_2 on spent fuel dissolution at very modest concentrations (10^{-5} to 10^{-4} mol.L^{-1}) (Carbol et al. 2005).

Figure 53 and 54 show the E_{CORR} response of 1.5 at% SIMFUEL to the addition of small concentrations of H_2O_2 under Ar-purged conditions and with a 5% H_2 / 95% Ar purge (~4.5 x 10^{-5} mol.L^{-1} of dissolved H_2). With Ar as the purge gas, Figure 53, E_{CORR} eventually achieves a new steady-state value after H_2O_2 addition, which is more positive than the value prior to its addition. However, in H_2/Ar-purged solutions, Figure 54, E_{CORR} rises to a maximum value, which is not necessarily proportioned to $[H_2O_2]$, before decreasing again. For low $[H_2O_2]$, E_{CORR} returns to the pre-addition value or to an even lower value. At higher $[H_2O_2]$, E_{CORR} does not recover fully to the pre-addition value but stabilizes at a value which is still considerably lower than achieved at the same $[H_2O_2]$ with Ar-purging; e.g., for 10^{-9} mol.L^{-1} (Figures 53 and 54).

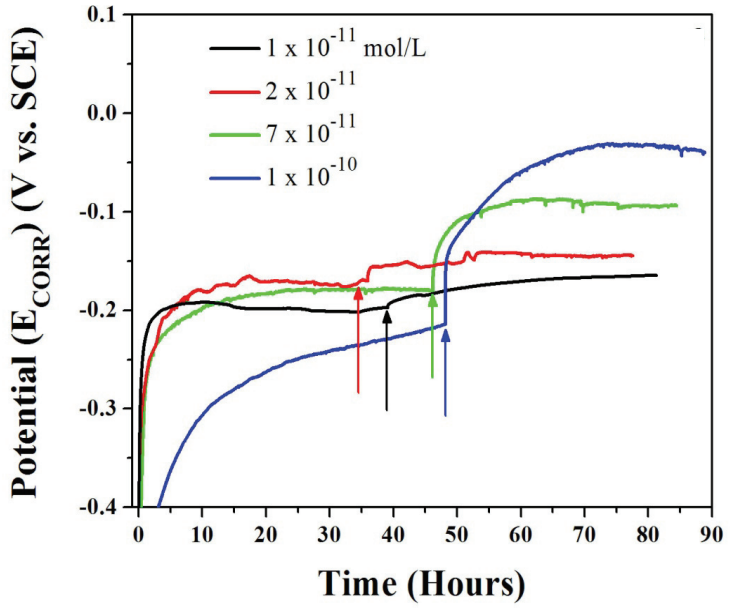


Figure 53: E_{CORR} recorded on a 1.5 at% SIMFUEL electrode in 0.1 mol/L KCl (pH 9.5) at 60ºC purged with Ar. The arrows indicate the times when H_2O_2 was added to achieve the specific concentration indicated.

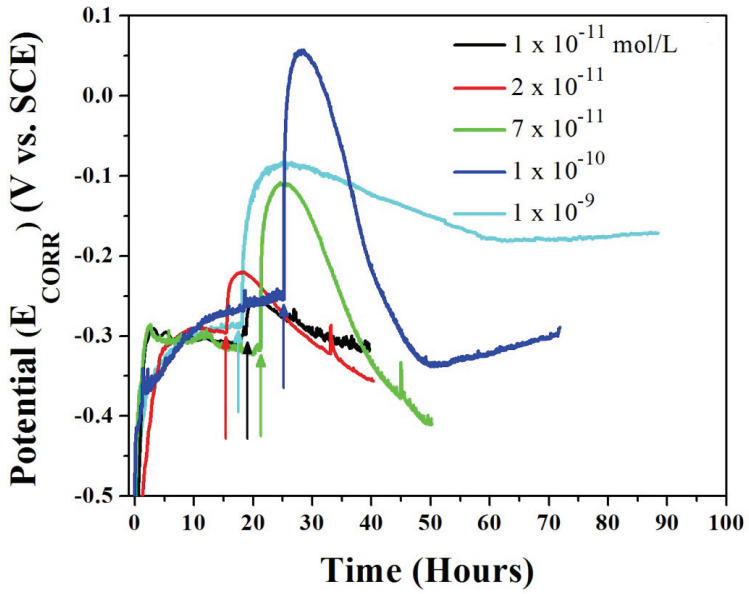


Figure 54: E_{CORR} recorded on a 1.5 at% SIMFUEL electrode in 0.1 mol/L KCl (pH 9.5) at 60ºC purged with 5% H_2/ 95% Ar. The arrows indicate the times when H_2O_2 was added to achieve the specific concentration indicated.

Figures 55 and 56 show the relative fractions of U^{IV}, U^{V}, and U^{VI} as a function of the added [H_2O_2] after a similar series of E_{CORR} measurements. The horizontal dotted lines show the percentages of each oxidation state measured after open circuit exposure to Ar- or H_2/Ar-purged solutions containing no H_2O_2, and provide baseline values by comparison to which the extent of oxidation in the presence of H_2O_2 can be gauged. Comparison of the surface compositions determined after E_{CORR} experiments containing H_2O_2 to these baselines values shows that the surfaces exposed to H_2/Ar-purged solutions are significantly more reduced (higher U^{IV}, lower U^{V} and U^{VI}), Figure 56, than those exposed to Ar-purging only, Figure 55. In fact, for [H_2O_2] ≤ 10^{-10} mol.L^{-1} in the H_2/Ar-purged solutions, the surface is more reduced after exposure to H_2O_2 than if no H_2O_2 had been added, suggesting exposure to low [H_2O_2] in the presence of H_2 actually leads to an overall reduction of the surface. At higher [H_2O_2] the extent of oxidation of the surface increases slightly to coincide with the baseline.

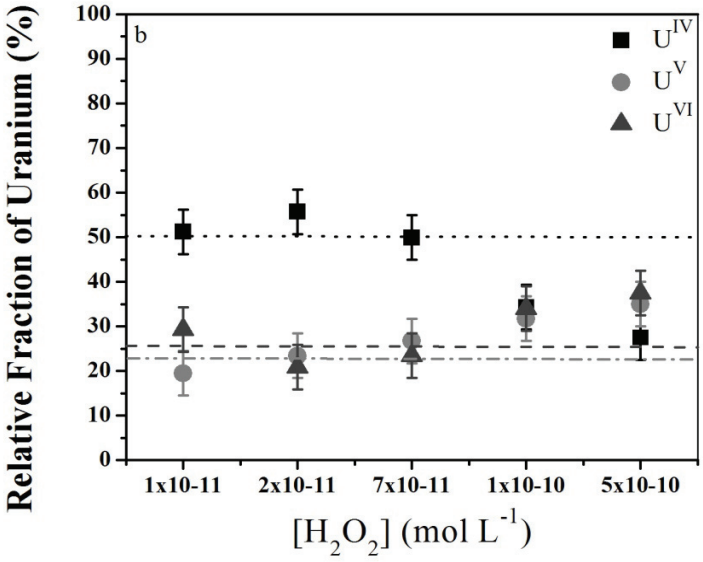


Figure 55: The relative fractions of U^{IV}, UI^{V} and U^{VI} (as determined by XPS) in the surface of a 1.5 at% SIMFUEL electrode after additions of various $[H_2O_2]$ to a 0.1 mol/L KCl solution (pH 9.5) purged with Ar. The lines refer to the fractions of U^{IV} (dotted line), U^{V} (dotted-dashed line) and U^{VI} (dashed line) in the surface after E_{CORR} experiments in solutions to which H_2O_2 was not added (Broczkowski 2008).

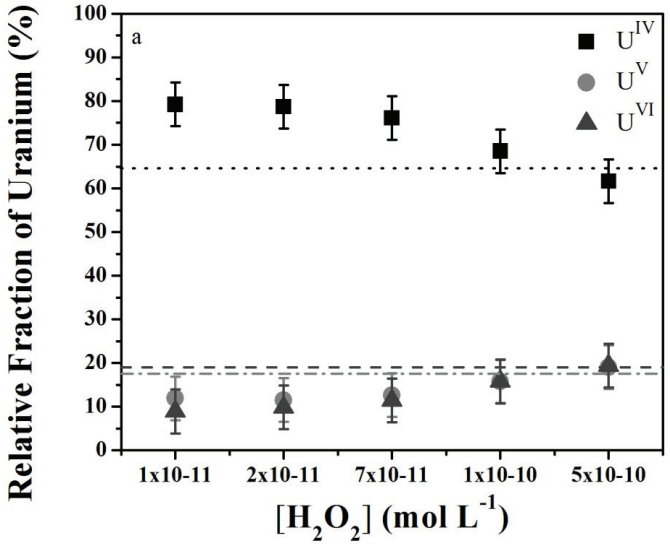


Figure 56: The relative fractions of U^{IV}, U^{V} and U^{VI} (as determined by XPS) in the surface of a 1.5 at% SIMFUEL electrode after additions of various $[H_2O_2]$ to a 0.1 mol/L KCl solution (pH 9.5) purged with H_2/Ar. The lines refer to the fractions of U^{IV} (dotted line), U^{V} (dotted-dashed line) and U^{VI} (dashed line) in the surface after E_{CORR} experiments in solutions to which H_2O_2 was not added (Broczkowski 2008).

When Ar is the purge gas, the overall extent of oxidation of the surface is considerably higher than when H_2/Ar is the purge gas. For $[H_2O_2] \leq 7 \times 10^{-11}$ mol.L^{-1}, no significant influence of H_2O_2 on surface composition is observed. For higher concentrations, a very clear influence of $[H_2O_2]$ is observed: the U^{IV} content is considerably lower and the U^{V} and U^{VI} contents are considerably higher than the calibration values.

Because XPS analyses were restricted to measurements of the final surface composition, there is no evidence that the rapid rise in E_{CORR} on adding H_2O_2 to the H_2/Ar-purged solution leads to surface oxidation which is then reversed when E_{CORR} subsequently decreases. However, the increase in E_{CORR} when H_2O_2 is added occurs irrespective of whether H_2 is present or not, Figures 53 and 54, indicating an immediate surface oxidation in both cases. This is to be expected since much evidence exists showing that noble metal particles enhance UO_2 corrosion by catalyzing the reduction of oxidants (Broczkowski et al. 2005, 2006; Trummer et al. 2008, 2009; Shoesmith et al. 1994) as illustrated in Figure 57A. The $OH^{\bullet}$ radical produced in this reaction could then oxidize a second U^{IV} surface atom or further oxidize the U^{V} surface species to the more soluble U^{VI} (UO_2^{2+}) (not illustrated in Figure 57). The extent of U^{VI} formation would increase as E_{CORR} becomes positive, as demonstrated by XPS, Figure 30.

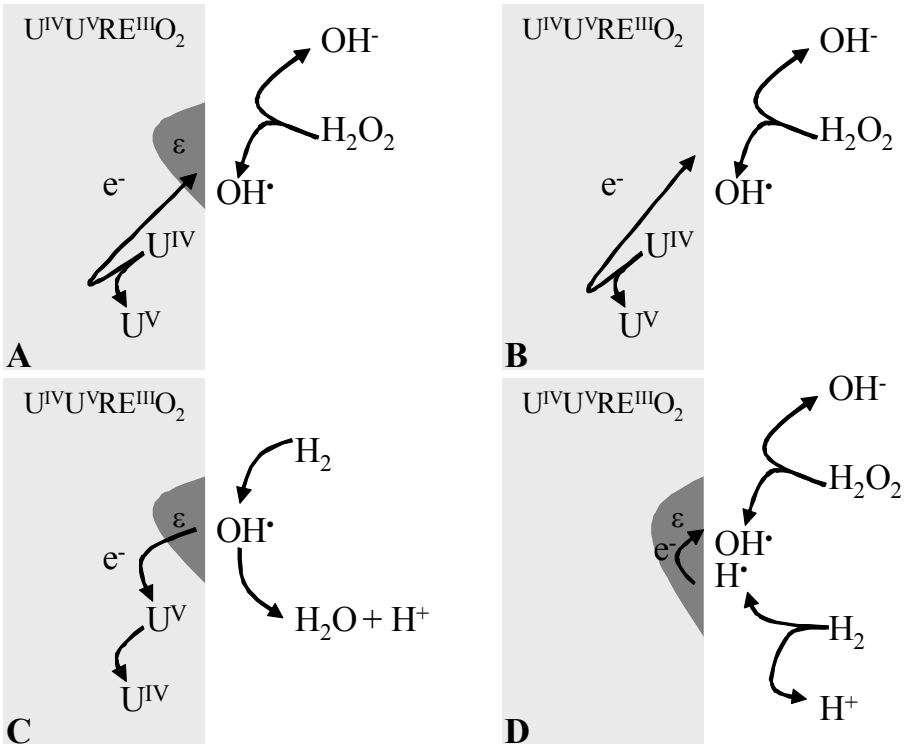


Figure 57: Proposed mechanism for the influence of H_2 on the corrosion 1.5 at% SIMFUEL containing noble metal (ε) particles in the presence of H_2O_2 (see text).

It has also been shown that H_2O_2 reacts directly and rapidly with the UO_2 surface (Sunder et al. 2004; Goldik et al. 2004, 2005, 2006), as illustrated in Figure 57B. While H_2O_2 reaction on UO_2 is likely to be slower than that on noble metal particles, the low number density and small size of these particles, Figure 10, and the large surface area of available UO_2 on SIMFUEL electrodes make the simultaneous reaction of H_2O_2 on both noble metal particles and UO_2 likely. The production of $OH^{\bullet}$ radicals by H_2O_2 reduction on the noble metal particles then offers a possible route by which H_2 could reverse the UO_2 oxidation process by scavenging these radicals to release an electron allowing the reduction of the oxidized U^{V} surface state as indicated in Figure 57C.

An additional redox scavenging route is available since H_2 dissociation to produce $H^{\bullet}$ radicals on noble metal particles can also occur, leading to the scavenging of $OH^{\bullet}$ radicals, and hence the prevention of UO_2 oxidation, by the radical recombination reaction ($H^{\bullet} + OH^{\bullet} \rightarrow H_2O$) illustrated in Figure 57D.

Irrespective of which of these particular mechanisms prevail, and there is a strong possibility all are involved, the XPS data in Figure 56 indicate that on 1.5 at% SIMFUEL (which simulates anticipated CANDU fuel burn-up) complete protection of the UO_2 surface from oxidation is achieved when the $[H_{2]} / [H_2O_2]$ ratio is $> 10^6$.

7.2 THE ROLE OF THE UO_2 SURFACE IN CONTROLLING SURFACE REDOX CONDITIONS

There remains the additional possibility that since H_2O_2 can directly oxidize the UO_2 surface via the formation of $OH^{\bullet}$ radicals, as illustrated in Figure 57B, H_2 could scavenge this radical and reverse the UO_2 oxidation process without involvement of the noble metal particles. This claim was made previously to explain the slow oxidation of UO_2 in the presence of ^{241}Am α-sources (Wren et al. 2005), but the available evidence was weak.

To investigate this possibility a similar series of E_{CORR} and XPS measurements was conducted on a rare-earth doped SIMFUEL containing no noble metal particles. The E_{CORR} values before and after the addition of H_2O_2 are shown for the Ar-purged and H_2/Ar-purged solutions in Figure 58A and B respectively. In Ar-purged solutions, E_{CORR} rapidly rose to a new steady-state value as observed on SIMFUEL containing noble metal particles. As expected the final E_{CORR} value increased with an increase in $[H_2O_2]$. In H_2/Ar-purged solution E_{CORR} also exhibited the same behaviour as observed on SIMFUEL containing noble metal particles, rising rapidly to more positive values than achieved in Ar-purged solutions before decreasing again. However, in this case E_{CORR} decreased more slowly and approached more positive steady-state values, suggesting irreversible oxidation occurred even at the lower $[H_2O_2]$ used in this experiment compared to that on the noble metal-containing SIMFUEL.

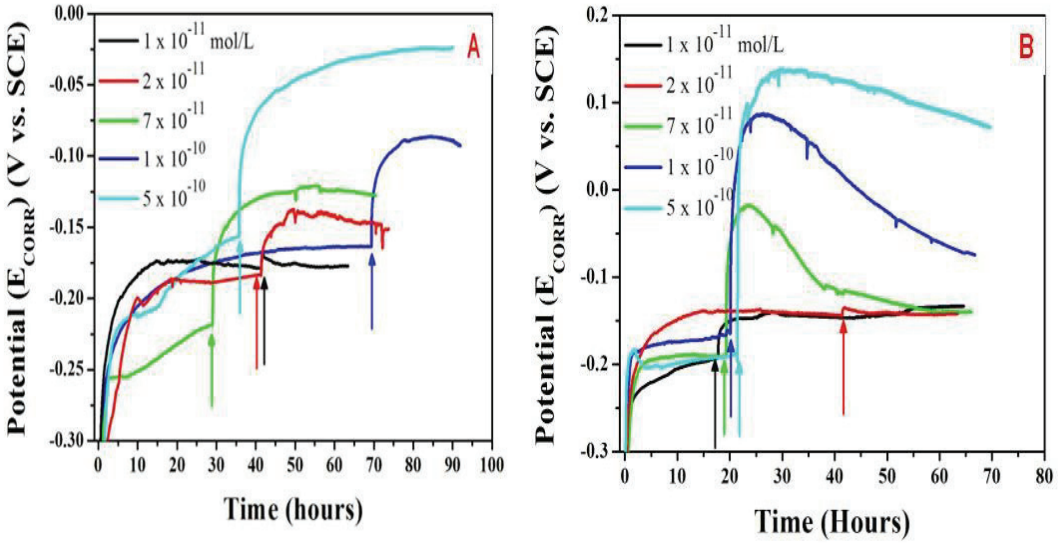


Figure 58: E_{CORR} recorded on a rare-earth doped SIMFUEL not containing noble metal particles in 0.1 mol/L KCl (pH 9.5) purged with (A) Ar at 60ºC; (B) H_2/Ar at 60ºC. The arrows indicate the times when H_2O_2 was added to achieve the specific concentration indicated.

Figure 59 shows the fractions of the U oxidation states as a function of [H_2O_2] in Ar-purged (59A) and H_2/Ar-purged (59B) solutions. Again, the horizontal dotted lines show the amounts of the three oxidation states measured in the electrode surface after exposure to the two purge gases in the absence of H_2O_2. The slight differences in these calibration lines reflect the minor differences in E_{CORR}, and hence extents of oxidation, on exposure to the two purge gases. By comparison to the differences observed when measurements were made on the SIMFUEL electrodes containing noble metal particles (Figures 56 and 57), these differences on the noble metal-free SIMFUEL are negligible. In both Ar-purged and H_2/Ar-purged solutions, the influence of increasing [H_2O_2] on the extent of oxidation of the surface is clear, the U^{IV} surface content decreasing as the [H_2O_2] increases. Comparison of the two plots in Figure 59 shows no significant differences in surface composition between Ar-purged and H_2/Ar-purged solutions.

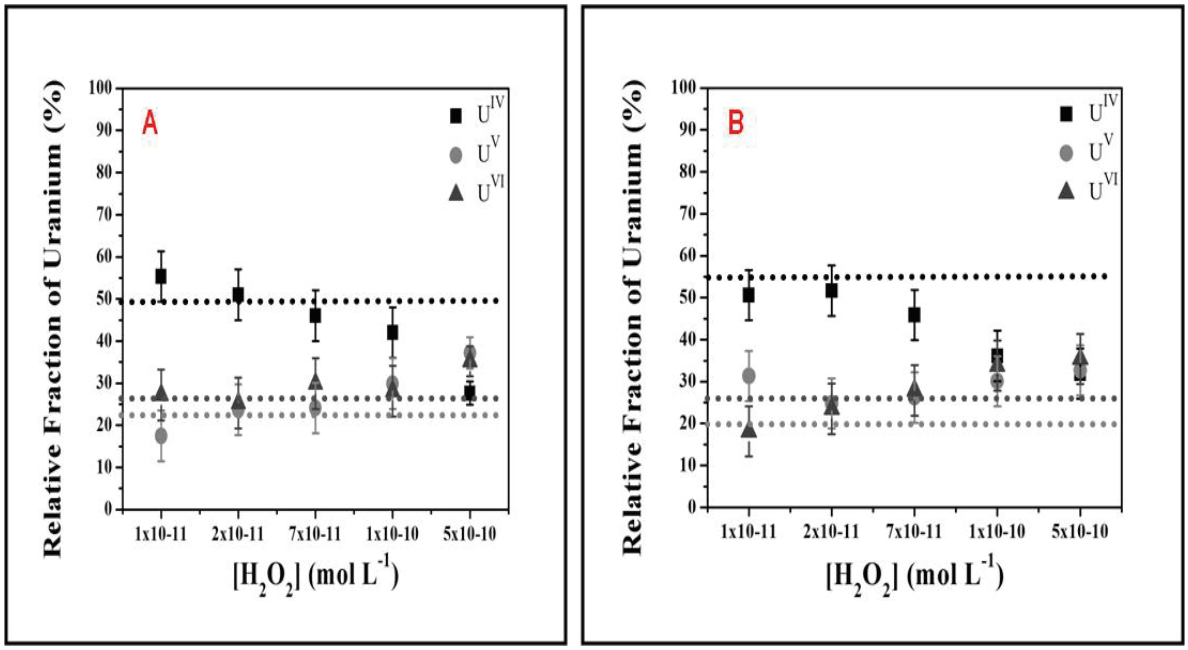


Figure 59: The relative fractions of U^{IV}, U^{V} and U^{VI} (as determined by XPS) in the surface of a SIMFUEL electrode not containing noble metal (ε) particles after additions of various $[H_2O_2]$ to a 0.1 mol/L KCl solution (pH 9.5) purged with (A) Ar; and (B) H_2/Ar. The lines refer to the fractions of U^{IV} (dotted line), U^{V} (dotted-dashed line), and U^{VI} (dashed line) in the surface after E_{CORR} experiments in solutions to which H_2O_2 was not added (Broczkowski 2008).

Based on these results there is no evidence to indicate any enduring influence of H_2 on the oxidation/corrosion of UO_2 in the absence of noble metal particles. However, when H_2 is present considerably more positive potentials are observed prior to relaxation to the final steady-state value with E_{CORR}, in some cases, rising to > 100mV. At these potentials, electrochemical results indicate that substantial oxidation leading to UO_2^{2+} dissolution can occur (Broczkowski et al. 2007). Thus, the E_{CORR} transients observed suggest that, to some extent, a similar, kinetically slower, redox cycle to that observed on noble metal-containing SIMFUEL occurs in their absence, suggesting the UO_2 surface alone does sustain redox reactions between H_2O_2 and H_2. However, the extent of this reaction remains to be confirmed.

8. DISCUSSION AND CONCLUSIONS

This report summarizes the studies performed over the last five years with a special emphasis on three key areas: (i) the influence of fuel properties on its corrosion; (ii) the likelihood of developing local chemistries, in particular acidic conditions within corrosion product deposits and flaws, such as fractures, in the fuel; (iii) the influence of dissolved H_2, from steel corrosion, on the fuel corrosion process.

To assist in these studies a number of novel analytical and experimental procedures were developed. MicroRaman spectroscopy was adapted to determine how changes in fuel composition influence the structural properties of the UO_2 matrix. Atomic force microscopy

(AFM) and current-sensing atomic force microscopy (CS-AFM) were used to relate these structural changes to the properties of the fuel surface, since it is these latter properties which will determine the eventual corrosion kinetics. These two techniques permit the simultaneous mapping of surface topography and local electrical conductivity both key properties of a surface undergoing corrosion. Finally, while standard electrochemical techniques were found useful in demonstrating the general reactivity of fuel surfaces they proved insensitive to the distribution in reactivity on surfaces which varied laterally in composition, in particular in degree of non-stoichiometry. Consequently, scanning electrochemical microscopy (SECM) was applied to investigate the corrosion behaviour at specific surface locations. Using these techniques, along with X-ray photoelectron spectroscopy (XPS) and secondary ion mass spectrometry (SIMS), the development of a detailed understanding of the influence of fuel properties on its surface reactivity was possible.

(a) The influence of rare-earth doping in fuel reactivity

Using a range of SIMFUEL specimens with varying degrees of simulated burn-up a preliminary investigation of the influence of rare-earth lattice dopants on the chemical reactivity of fuel was determined. MicroRaman spectroscopy indicated that as the degree of doping (simulated burn-up) was increased a systematic degradation of the fluorite structure of the UO_2 matrix occurred. Although not proven in this study this degradation is thought to be associated with the defect clusters formed involving the rare-earth dopants and the associated oxygen vacancies.

Electrochemical techniques showed a measurable but marginal influence of rare-earth doping on the surface oxidation of UO_2 (to UO_{2+x}) but a more substantial suppression of the dissolution (as UO_2^{2+}) and corrosion product deposition process (as $UO_3 \bullet yH_2O$) process. This latter influence became more marked as the temperature of the exposure solution was increased up to 90ºC. For the lowest simulated burn-up, which simulates the burn-ups expected for used CANDU fuel, the influence of doping (compared to undoped fuel) was minor to inconsequential. This indicates this influence will be minor. However, the observed suppression of fuel reactivity at higher doping levels suggests that the retention of rare-earths in the surface of corroding fuel will eventually begin to slow its dissolution and suppress radionuclide release. Studies are on-going to determine whether this is the case.

(b) The influence of non-stoichiometry on fuel reactivity

The influence in non-stoichiometry was studied in considerable detail. While in-reactor increases in degree of non-stoichiometry are likely to be limited (to ≤ $UO_{2.007}$) by reaction of the excess O produced with the Zircaloy cladding, other potential sources of non-stoichiometry exist. This includes residual non-stoichiometry from the original fuel sintering process, possibly associated with grain boundaries. The above studies also revealed the somewhat large effect that localized non-stoichiometry within the specimens produced.

MicroRaman spectroscopy showed very distinct changes in fuel structure occur as the degree of non-stoichiometry increases. At low degrees of non-stoichiometry there is an increase in the number of randomly distributed O interstitial defects. As the degree of non-stoichiometry increases these defects begin to associate into clusters, and for a sufficiently high degree large cuboctahedral clusters are formed.

Studies using, AFM, CS-AFM and SECM clearly demonstrated that the anodic reactivity (a major influence on corrosivity) increased substantially with the degree of non-stoichiometry with

the reactivity of highly non-stoichiometric clusters being ≥ 10^3 more reactive than close-to-stoichiometric UO_2. Since non-stoichiometric locations may also catalyze cathodic reactions, such as, the reduction of radiolytic H_2O_2, such locations may be able to preferentially support both anodic and cathodic reactions during fuel corrosion. However, the occurrences of such highly non-stoichiometric locations are unlikely in CANDU fuel unless substantial degradation is allowed to occur in storage prior to disposal. Since the degree of non-stoichiometry is unlikely to increase in-reactor to > $UO_{2.007}$, these studies suggest the potential influence on the corrosion rate should be less than a factor of 5. It is likely the influence will be considerably less than this. However, since non-stoichiometry is most likely to be associated with grain boundaries, it is judicious to retain the presently adopted assumption (in waste disposal performed assessment calculations) that radionuclides residing in grain boundaries will be part of the instant release fraction.

(c) Development of local acidity at a corroding fuel surface

Previous model calculations predicted that any local acidification on locations on the fuel surface, which could accelerate corrosion, would be minor and would lead, at worst, to only a marginal influence on fuel corrosion rates. To verify this prediction a series of experiments was undertaken in which electrochemical techniques were used to control fuel corrosion rates, as closely as experimentally feasible, to those anticipated under disposal conditions. The "minimum" redox condition achieved in these experiments simulated the conditions that would be expected to prevail in aerated environments. Even for these conditions there was no experimental evidence to suggest local acidification was possible. Since these conditions are considerably more oxidizing than those achievable by α-radiolysis at the anticipated dose rates in spent fuel the chances of developing locally acidified sites within the corroding fuel are highly unlikely.

(d) The influence of hydrogen on fuel corrosion

Corrosion of the carbon steel vessel containing the spent fuel (after failure of the outer copper corrosion barrier) is likely to lead to the generation of substantial H_2 pressures within sealed repositories, and a considerable amount of experimental evidence has been generated to demonstrate the ability of H_2 to suppress fuel corrosion. Our previous preliminary studies demonstrated that the noble metal (epsilon) particles present in spent fuel acted as catalysts for H_2 oxidation thereby suppressing the oxidation of the fuel matrix. These studies were extended to a wider range of SIMFUEL specimens. SIMS analyses were used to confirm the noble metal character of the particles and to demonstrate that their number density increased with the degree of simulated burn-up. In the presence of even small concentrations of dissolved H_2 the corrosion potential of the SIMFUELs was found to decrease as the number density of ε-particles increased. For the 6 at% SIMFUEL, the corrosion potential was suppressed to the equilibrium potential for UO_2 oxidation. These experiments confirm that these particles, distributed in a rare-earth doped, conductive UO_2 matrix can completely suppress fuel oxidation and corrosion providing their number density is high. Even for the low particle density associated with 1.5 at% SIMFUEL (with the simulated burn-up expected for CANDU fuel) only a small increase in dissolved H_2 concentration is required for complete suppression. That the extent of oxidation was controlled by H_2 oxidation on the particles was confirmed by XPS.

Since noble metal particles are catalytic not only for the oxidation of H_2 leading to the suppression of fuel corrosion but also for H_2O_2 reduction leading to the catalysis of fuel corrosion a series of experiments were performed to investigate the influence of these particles

when both H_2 and H_2O_2 were present. These studies, based on a combination of corrosion potential and XPS measurements, demonstrated that on 1.5 at% SIMFUEL complete protection of the fuel surface from corrosion could be achieved providing the $[H_2]$ / $[H_2O_2]$ ratio is > 10^6. Since the radiolytic concentrations of H_2O_2 under fuel disposal conditions are likely to be considerably < 10^{-9} mol.L^{-1} and the concentrations of dissolved H_2 > 10^{-3} mol.L^{-1} it possible that the fuel corrosion/radionuclide release processes could be completely suppressed by H_2 oxidation on noble metal particles.

ACKNOWLEDGEMENTS

This research was funded under the Industrial Research Chair agreement between the Canadian Natural Science and Engineering Research Council (NSERC) and the Nuclear Waste Management Organization (NWMO, Toronto). The authors thank Dr. Zhifeng Ding for the use of SECM and Surface Science Western for the use of Raman, XPS, ToF-SIMS and SEM/EDX.

REFERENCES

Bevan, D. J.M., I.E. Grey and B.T.M. Willis. 1986. The crystal structure of β-U_4O_{9-y}. J. Solid State Chem. 61, 1-7.

Broczkowski, M.E. 2008. The effects of hydrogen and temperature on the electrochemistry and corrosion of uranium dioxide. Ph.D. Thesis, the University of Western Ontario. London, Canada.

Broczkowski, M.E., D. Zagidulin and D.W. Shoesmith. 2010. The role of dissolved hydrogen in the corrosion/dissolution of spent nuclear fuel. In: Nuclear Energy and the Environment, American Chemical Society Symposium Proceedings, Vol. 1046, Chapter 26, 349-380.

Broczkowski, M.E., J.J. Noël and D.W. Shoesmith. 2005. The inhibiting effects of hydrogen on the corrosion of uranium dioxide under nuclear waste disposal conditions. J. Nucl. Mater. 346, 16-23.

Broczkowski, M.E., J.J. Noël and D.W. Shoesmith. 2007. The influence of dissolved hydrogen on the surface composition of doped uranium dioxide under aqueous corrosion conditions. J. Electroanal. Chem. 602, 8-16.

Broczkowski, M.E., J.S. Goldik, J.J. Noel and D.W. Shoesmith. 2006. The influence of noble metal particles on redox reactions on uranium dioxide surfaces. Proceedings of the Eleventh International Ceramics Congress (edited by P.Vincenzini), Acireale, Sicily, Italy, June 4-9, 2006. Trans. Tech. Publ. (Switzerland) (www.scientific.net), Advances in Science and Technology 45, 1996-2002.

Broczkowski, M.E., R. Zhu, Z. Ding, J.J. Noël and D.W. Shoesmith. 2006. Electrochemical, SECM, and XPS studies on the influence of H_2 on UO_2 nuclear fuel corrosion. Mat. Res. Soc. Symp. Proc. 932, 449-456.

Carbol, P., J. Cobos-Sabate, J.-P. Glatz, C. Ronchi, V. Rondinella, D.H. Wegen, T. Wiss, A. Loida, V. Metz, B. Kienzler, K. Spahiu, B. Grambow, J. Quinones and A. Martinez Esparza Valiente. 2005. The effect of dissolved hydrogen on the dissolution of ^{233}U-doped UO_2(s), high burn-up spent fuel and MOX fuel. Swedish Nuclear Fuel and Waste Management Company Technical Report TR-05-09. Stockholm, Sweden.

Carbol, P., P. Fors, T. Gouder and K. Spahiu. 2009a. Hydrogen suppresses UO_2 corrosion. Geochim. Cosmochim. Acta 73, 4366-4375.

Carbol, P., P. Fors, S. Van Winckel and K. Spahiu. 2009b. Corrosion of irradiated MOX fuel in the presence of dissolved H_2. J. Nucl. Mater. 392, 45-54.

Cheong, W.-J., P.G. Keech, J.C. Wren, D.W. Shoesmith and Z. Qin. 2007. Modeling the distribution of acidity within nuclear fuel (UO_2) corrosion product deposits and porous sites. Mat. Res. Soc. Symp. Proc. 987, 27-33.

Choi, J.W., R.J. McEachern, P. Taylor and D.D. Wood. 1996. The effect of fission products on the rate of U_3O_8 formation in SIMFUEL oxidized in air at 250ºC. J. Nucl. Mater. 230, 250-258.

Cobos, J., D. Papaioannou, J. Spino and M. Coquerelle. 1998. Phase characterization of simulated high burn-up UO_2 fuel. J. Alloys Compd. 271-273, 610-615.

Conradson, S.D., D. Manara, F. Wastin, D.L. Clark, G.H. Lander, L.A. Morales, J. Rebizant and V.V. Rondinella. 2004. Local structure and charge distribution in the $UO_2 – U_4O_9$ system. Inorg. Chem. 43, 6922-6935.

Corcoran, E.C., M.H. Kaye, F. Akbari, J.D. Higgs, B.J. Lewis and W.T. Thompson. 2007. First principles CANDU fuel model and validation experimentation. Proceedings of the 2007 International LWR Fuel Performance Meeting, San Francisco, California, September 30 – October 3, Paper 107, 99-106.

Crocombette, J.-P., F. Jollet, L.T. Nga and T. Petit. 2001. Plane-wave pseudopotential study of point defects in uranium dioxide. Phys. Rev. B. Condens. Matter Mater. Phys. 64, 104107-104112.

Cui, D., E. Ekeroth, P. Fors and K. Spahiu. 2008. Surface mediated processes in the interaction of spent fuel or alpha-doped UO_2 with H_2. Mat. Res. Soc. Symp. Proc. 1104, 87-99.

Dudney, N. J., R. L. Coble and H. L. Tuller. 1981. Electrical conductivity of pure and yttria-doped uranium dioxide. J. Am. Ceram. Soc. 64, 627-631.

Ekeroth, E., O. Roth and M. Jonsson. 2006. The relative impact of radiolysis products in radiation induced oxidative dissolution of UO_2. J. Nucl. Mater. 355, 38-46.

Floyd, M.R., J. Novak and P.T. Truant. 1992. Fission-gas releases in fuel performing to extended burnups in Ontario Hydro Nuclear Generating Stations. Atomic Energy of Canada Limited Report AECL-10636. Chalk River, Canada.

Fors, P., Carbol, S. Van Winckel and K. Spahiu. 2009. Corrosion of high burn-up structured UO_2 fuel in the presence of dissolved H_2. J. Nucl. Mater. 394, 1-8.

Freyss, M., T. Petit and J.-P. Crocombette, 2005. Point defects in uranium dioxide: Ab initio pseudopotential approach in the generalized gradient approximation. J. Nucl. Mater. 347, 44-51.

Garisto, F., D.H. Barber, E. Chen, A. Inglot and C.A. Morrison. 2009. Alpha, beta and gamma dose rates in water in contact with used CANDU fuel. Nuclear Waste Management Organization Report NWMO TR-2009-27. Toronto, Canada.

Garrido, F., R.M. Ibberson, L. Nowicki and B.T.M. Willis. 2003. Cuboctahedral clusters in U_3O_7. J. Nucl. Mater. 322, 87-89.

Geng, H.Y., Y. Chen, Y. Kaneta, M. Iwasama, T. Ohnuma and M. Kinoshita. 2008. Point defects and clustering in uranium dioxide by LSDA + U calculations. Phys. Rev. B: Condens. Matter Mater. Phys. 77, 104120.1-104120.16.

Goldik, J.S., H.W. Nesbitt, J.J. Noël and D.W. Shoesmith. 2004. Surface electrochemistry of UO_2 in dilute alkaline hydrogen peroxide solutions. Electrochim. Acta 49, 1699-1709.

Goldik, J.S., J.J. Noël and D.W. Shoesmith. 2005. The electrochemical reduction of hydrogen peroxide on uranium dioxide electrodes in alkaline solution. J. Electroanal. Chem. 582, 241-248.

Goldik, J.S., J.J. Noël and D.W. Shoesmith. 2006. The effects of simulated fission products on the reduction of hydrogen peroxide on simulated nuclear fuel electrodes. J. Electchem. Soc. 153, E151-E159.

Grenthe, I., J. Fuger, R.J. Konings, R.J. Lemire, A.B. Muller, C. Nguyen-Trung and H. Wanner. 1992. Chemical Thermodynamics, Vol. 1, Chemical Thermodynamics of Uranium. OECD Nuclear Energy Data Bank. North Holland Elsevier Science. Amsterdam, Netherlands.

Grimes, R.W, and C.R.A. Catlow. 1991. The stability of fission products in uranium dioxide. Philos. Trans. R. Soc. London, Ser. A. 335, 609-618.

Guillamont, R., T. Fanghänel, J. Fuger, I. Grenthe, V. Neck, D.A. Palmer and M.H. Rand. 2003. Chemical Thermodynamics, Vol. 5, Update on the Chemical Thermodynamics of Uranium, Neptunium, Plutonium, Americium, and Technetium. OECD Nuclear Energy Data Bank. North Holland Elsevier Science. Amsterdam, Netherlands.

Gupta, F., G. Brillant and A. Pasturel. 2007. Correlation effects and energetics of point defects in uranium dioxide: A first principle investigation. Philos. Mag. 87, 2561-2569.

Hanson, B. D. 1998. The burnup dependence of light water reactor spent fuel oxidation. Pacific Northwest Laboratory Report, PNNL-11929. Richland, USA.

Hastings, I.J. 1982. Structures in irradiated UO_2 fuel from Canadian reactors. Atomic Energy of Canada Limited Report AECL-MISC-249. Chalk River, Canada.

He, H. and D.W. Shoesmith. 2010. Raman spectroscopic studies of defect structures and phase transitions in hyper-stoichiometric UO_{2+x}. Phys. Chem. Chem. Phys. 12, 8108-8117.

He, H., P. Keech, M.E. Broczkowski, J.J. Noël and D.W. Shoesmith. 2007. Characterization of the influence of fission product doping on the anodic reactivity of uranium dioxide. Can. Chem. 85, 702-713.

Hocking, W.H., J.S. Betteridge and D.W. Shoesmith. 1994. The cathodic reduction of oxygen on uranium oxide in dilute alkaline aqueous solution. J. Electroanal. Chem. 379, 339-351.

Hyland, G.J. and J. Ralph. 1983. Electronic contributions to the high temperature thermophysical properties of UO_{2+x}. A critical analysis. High Temp. – High Pres. 15, 179-190.

Johnson, L.H. and D.W. Shoesmith. 1988. Spent fuel. In: "Radioactive Wasteforms for the Future," edited by W.B. Lutze and R.C. Ewing. Elsevier Science Publishers. Amsterdam, Netherlands.

Jonsson, M., E. Ekeroth and O. Roth. 2004. Dissolution of UO_2 by one- and two-electron oxidants. Mat. Res. Soc.Symp. Proc. 807, 72-82.

Keech, P.G., J.J. Noël and D.W. Shoesmith. 2008. The electrochemical reduction of hydrogen peroxide on uranium dioxide under intermediate pH to acidic conditions. Electrochim. Acta 53, 5675-5683.

King, F. 2007. Status of the understanding of used fuel container corrosion processes – Summary of current knowledge and gap analysis. Nuclear Waste Management Organization Report NWMO TR-2007-09. Toronto, Canada.

King, F. and D.W. Shoesmith. 2010. Long term containment performance – corrosion behaviour of candidate canister materials. In: "Geological Repositories for Safe Disposal of Spent Nuclear Fuel and Radioactive Material", edited by J. Ahn and M. Apted, Woodhead Publishing Limited, Cambridge, U.K., Chapter 14.

King, F. and M. Kolar. 2000. The copper container corrosion model used in AECL's second case study. Ontario Power Generation Report 06819-REP-01200-10041-R00. Toronto, Canada.

King, F. and M. Kolar. 2002. Sensitivity analysis of the factors affecting the effective G-value, G_{EFF}, in the mixed potential model for used fuel dissolution. Ontario Power Generation Report 06819-REP-01300-10044-R00. Toronto, Canada.

Kleykamp, H. 1985. The chemical state of the fission products in oxide fuels. J. Nucl. Mater. 131, 221-246.

Kleykamp, H. 1988. Chemical state of fission products in oxide fuels at different stages of the nuclear fuel cycle. Nucl. Technol. 80, 412-422.

Kleykamp, H. 1990. Post irradiation examinations and composition of the residues from nitric acid dissolution experiments. J. Nucl. Mater. 171, 181-188.

Kleykamp, H. 1993. The solubility of selected fission products in UO_2 and PuO_2. J. Nucl. Mater. 206, 82-86.

Livneh, T. and E. Sterer. 2006. The effect of pressure on the resonant multiphonon Raman scattering in UO_2. Phys. Rev. B: Condens. Matter Mater. Phys. 73, 085118-085119.

Lucuta, P.G., R.A. Verrall, H.-J. Matzke and B.J.F. Palmer. 1991. Microstructural features of SIMFUEL - Simulated high-burnup UO_2-based nuclear fuel. J. Nucl. Mater. 178, 48-60.

Maak, P. 2007. Development of a used fuel container for nuclear fuel waste. Mat. Res. Soc. Symp. Proc. 807, 447.

Maak, P. and G. Simmons. 2001. Summary report: A screening study of used fuel container geometric designs and emplacement methods for a deep geologic repository. Ontario Power Generation Report 06819-REP-01200-10065-R00. Toronto, Canada

MacEachern, R.J. and P. Taylor. 1998. A review of the oxidation of uranium dioxide at temperatures below 400ºC. J. Nucl. Mater. 254, 87-121.

Matzke, Hj. 1982. Radiation damage in crystalline insulators, oxides and ceramic nuclear fuels. Rad. Effects. 64, 3–33.

McMurry, J., D.A. Dixon, J.D. Garroni, B.M. Ikeda, S. Stroes-Gascoyne, P. Baumgartner and T.W. Melnyk. 2003. Evolution of a Canadian deep geologic repository: Base scenario. Ontario Power Generation Report 06819-REP-01200-10092-R00. Toronto, Canada.

Nerikar, P., T. Watanabe, J.S. Tulenko, S.R. Phillpot and S.B. Sinnott. 2009. Energetics of intrinsic point defects in uranium dioxide from electronic-structure calculations. J. Nucl. Mater. 384, 61-69.

Nicol, M.J. and C.R.S. Needes. 1975. Anodic dissolution of uranium dioxide – I. In perchlorate solutions. Electrochim. Acta 20, 585-589.

Nielsen, F. and M.Jonsson. 2006. Geometric α- and β- dose rate distributions and production rates of radiolysis products in water in contact with spent nuclear fuel. J.Nucl. Mater. 359, 1-7.

Nilsson, S. 2008. Influence of metallic fission products and self irradiation on the rate of spent nuclear fuel-matrix dissolution. Licentiate Thesis in Chemistry, Royal Institute of Technology, Paper V. Stockholm, Sweden.

Nilsson, S., and M. Jonsson. 2007. On the catalytic effects of UO_2 (s) and Pd(s) on the reaction between H_2O_2 and H_2 in aqueous solution. J. Nucl. Mater. 372, 160-163.

Norskov, J.K., T. Bligaard, A. Lagodottir, J.R. Kitchin, J.G. Chen, S. Pandelov and U. Stimming. 2005. Trends in exchange currents for hydrogen evolution. J. Electrochem. Soc. 152, J23-J26.

Ofori, D. 2008. The influence of corrosion product deposit in UO_2 corrosion/dissolution. Ph.D. Thesis, the University of Western Ontario. London, Canada.

Ofori, D., P.G. Keech, J.J. Noël and D.W. Shoesmith. 2010. The influence of deposited films on the anodic dissolution of uranium dioxide. J. Nucl. Mater. 400, 84-93.

O'Neil, K.D., B. Shaw and O.A. Semenikhin. 2007. On the origin of mesoscopic inhomogeneity of conducting polymers. J. Phys. Chem. B 111, 9253-9269.

O'Neil, K.D., H. He, P.G. Keech, D.W. Shoesmith and O. Semenikhin. 2008. Anistropy of local electrical conductivity of hyper-stoichiometric uranium dioxide revealed by current-sensing atomic force microscopy (CS-AFM). Electrochem. Comm. 10, 1805-1808.

Park, K. and D.R. Olander. 1992. Defect models for the oxygen potentials of gadolinium- and europium –doped urania. J. Nucl. Mater. 187, 89-96.

Park, K., M.-S. Yang and H.-WS. Park. 1997. The stoichiometry and the oxygen potential change of urania fuels during irradiation. J. Nucl. Mater. 247, 116-120.

Parks, G.A. and D.C. Pohl. 1988. Hydrothermal solubility of uranite. Geochem. Cosmochim. Acta 52, 863-875.

Paschol, J.O.A., H. Kleykamp and F. Thummler. 1987. Phase equilibria in the pseudoquaternary BaO-UO_2-ZrO_2-MoO_2 system. J. Nucl. Mater. 151, 10-21.

Santos, B.G., J.J. Noël and D.W. Shoesmith. 2006. The influence of potential on the anodic dissolution of SIMFUEL (UO_2). Electrochim. Acta 51, 4157-4166.

Santos, B.G., J.J. Noël and D.W. Shoesmith 2006a. The influence of calcium ions on the development of acidity in the corrosion product deposits on SIMUFUEL (UO_2). J. Nucl. Mater. 350, 320-331.

Santos, B.G., J.J. Noël and D.W. Shoesmith. 2006b. The influence of silicate on the development of acidity in corrosion product deposits on SIMFUEL (UO_2). Corros. Sci. 48, 3852-3868.

Santos,B.G., J.J. Noël and D.W. Shoesmith. 2006c. The effect of pH on the anodic dissolution of SIMFUEL (UO_2). J. Electroanal. Chem. 586, 1-11.

Santos, B.G., H.W. Nesbitt, J.J. Noël and D.W. Shoesmith. 2004. X-ray photoelectron spectroscopy study of anodically oxidized SIMFUEL surfaces. Electrochim. Acta 49, 1863-1873.

Shoesmith, D.W. 2000. Fuel Corrosion processes under waste disposal conditions. J. Nucl. Mater. 282, 1-31.

Shoesmith, D.W. 2008. The role of dissolved hydrogen on the corrosion/dissolution of spent nuclear fuel. Nuclear Waste Management Organization Report NWMO TR-2008-19. Toronto, Canada.

Shoesmith, D.W. 2007. Used fuel and uranium dioxide dissolution studies – A review. Nuclear Waste Management Organization Report NWMO TR-2007-03. Toronto, Canada.

Shoesmith, D. W. and D. Zagidulin. 2010. The corrosion of zirconium under deep geological repository conditions. Nuclear Waste Management Organization Report NWMO TR-2010-19. Toronto, Canada.

Shoesmith, D.W., J.J. Noël and F. Garisto. 2004. An experimental basis for a mixed potential model for nuclear fuel corrosion within a failed nuclear wastecontainer. Mat. Res. Soc. Symp. Proc. 824, 81-88.

Shoesmith, D.W., J.J. Noël, Z. Qin, C.T. Lee, J.S. Goldik, B.G. Santos and M.E. Broczkowski. 2005. Corrosion of nuclear fuel (UO_2) inside a failed nuclear waste container. Ontario Power Generation Report 06819-REP-01200-10145-R00. Toronto, Canada.

Shoesmith, D.W., S. Sunder and W.H. Hocking. 1994. Electrochemistry of UO_2 nuclear fuel. In: "Electrochemistry of Novel Materials", edited by J. Lipkowski and P.N. Ross, VCH Publishers, New York, Chapter 6, 297-337.

Shoesmith, D.W., S. Sunder, M.G. Bailey and N.H. Miller. 1996. Oxidation and dissolution (corrosion) of used fuel electrodes in aqueous perchlorate and carbonate solutions. J. Nucl. Mater. 227, 287-299.

Shoesmith, D.W., W.H. Hocking, S. Sunder, J.S. Betteridge and N. H. Miller. 1994. Electrochemical studies of SIMFUEL. J. Alloys and Comps 213/214, 551-553.

Shoesmith, D.W., M.Kolar and F.King. 2003. A mixed potential model to predict fuel (uranium dioxide) corrosion within a failed nuclear waste container. Corrosion. 59, 802-816.

Smith, H.J., J.C. Tait and R.E.V. Massow. 1987. Radioactive decay properties of Bruce "A" CANDU UO_2 fuel and fuel recycle waste. Atomic Energy of Canada Limited Report AECL-9072. Pinawa, Canada.

Sunder, S., D.W. Shoesmith, R.J. Lemire, M.G. Bailey and G.J. Wallace. 1991. The effect of pH on the corrosion of nuclear fuel (UO_2) in oxygenated solutions. Corros. Sci. 32, 373-386.

Sunder, S., N.H. Miller and D.W. Shoesmith. 2004. Corrosion of uranium dioxide in hydrogen peroxide solutions. Corros. Sci. 46, 1095-1111.

Tait, J.C., I.C. Gould and G.B. Wilkin. 1989. Derivation of initial radionuclide inventories for the safety assessment of the disposal of used CANDU fuel. Atomic Energy of Canada Limited Report AECL-9881. Pinawa, Canada.

Thomas, L.E., R.E. Einziger and H.C. Buchanan. 1993. Effect of fission products on air-oxidation of LWR spent fuel. J. Nucl. Mater. 201, 310-319.

Trummer, M., O. Roth and M. Jonsson. 2009. H_2 inhibition of radiation-induced dissolution of spent nuclear fuel. J. Nucl. Mater. 383, 226-230.

Trummer, M., S. Nilsson and M. Jonsson. 2008. On the effects of fission product noble metal inclusions on the kinetics of radiation-induced dissolution of spent nuclear fuel. J. Nucl. Mater. 378, 55-59.

Verrall, R.A., Z. He and J.F. Mouris. 2005. Characterization of fuel oxidation in rods with clad-holes. J. Nucl. Mater. 344, 240-245.

Wasywich, K.M., W.H. Hocking, D.W. Shoesmith and P. Taylor. 1993. Differences in oxidation behaviour of used CANDU fuel during prolonged storage in moisture- saturated air and dry air at 150ºC. Nucl. Tech. 104, 309-329.

Willis, B.T.M. 1987. Crystallographic studies of anion excess uranium oxides. J. Chem. Soc. Faraday Trans. 2, 83, 1073-1081.

Winter, P.W. 1989. The electronic transport properties of UO_2. J. Nucl. Mater. 161, 38-43.

Wren, J.C., D.W. Shoesmith and S. Sunder. 2005. Corrosion Behaviour of uranium dioxide in alpha radiolytically decomposed water. J. Electrochem. Soc. 152, B470-B481.